THE STUDY ON MICROWAVE PROPERTIES OF HIGH-T_C SUPERCONDUCTING FILMS DEPOSITED ON COPPER SUBSTRATES

by

Jian-Fei Liu

DOCTOR OF PHILOSOPHY

Department of Accelerator Science
School of Mathematical and Physical Science
The Graduate University for Advanced Studies

1998

Contents

1. Introduction

1.1 Background

A phenomenon in which a substance loses all electrical resistance was first discovered in metals at liquid helium temperatures by Kamerlingh Onnes in 1911[1]. With the potential of zero resistivity state for electrical applications, superconducting materials have long held the promise of many wonderful technological benefits already in the years following the discovery of superconductivity. Some of the most important applications[2] of superconductors are either in high current wires for powerful supermagnets or in thin films structures like Josephson junctions for superconducting electronics. Another important application[3] is in large-sized cavity structures for energy-saving and high-field rf acceleration of charge particles. These applications utilize so-called "low temperature" superconducting (LTS) materials such as niobium, alloys of niobium, lead and titanium. The inconvenience and expense associated with the cooling of such materials below their critical temperature (T_c), which is ~ 10 K, have restricted their use to applications where performance outweighs the costs of expensive refrigeration.

The discovery of "high temperature" superconductivity (HTS) in 1986[4] resulted in the expansion of the study of the superconductors from a handful of laboratories to hundreds of laboratories worldwide. The discovery of superconductivity above 77 K

(the boiling point of liquid nitrogen) in compounds of Y-Ba-Cu-O[5] gave new hope for the economical and widespread applications of superconductivity.

It is expected that applications of HTS will be made in various fields. Since the discovery of HTS, the research on HTS has been very intensive, and many kinds of applications have been tried. Only a few applications, however, have come onto the market: HTS SQUID[6], microwave devices[7] and Bi-compound wires or tapes[8-10]. The reason is quite clear; as the HTS has complex structures and is quite peculiar, it has been rather difficult to control these materials artificially. Furthermore, superconductivity itself is quite different from that of LTS materials. For instance, the superconductivity is strongly two-dimensional and so it is very sensitive to the structure of crystals. It is, however, sure that the development of synthesis techniques for the high-quality materials will accelerate the progress of applications.

1.2 Motivation of study

In particle accelerators for high energy physics, microwave cavities are used to accelerate charged particles, such as electrons and positrons up to the energy at which physics experiments are made. Accelerating field attained by normal conducting copper cavities is practically limited to about 1 MV/m due to difficulty in removing enormous heat created at cavity wall. In superconducting cavities, the surface resistance and hence the wall loss are lowered dramatically. This enables superconducting cavities to achieve accelerating field much higher than that obtained by copper cavities. A tremendous effort to utilize superconductivity for accelerators has put niobium superconducting cavities into practice, and they are now being operated at several major high energy physics laboratories in the world, such as CERN, DESY, TJLab, Cornell University and KEK.

In the cavity application of superconductivity, two of the most important parameters are the surface resistance and the RF critical magnetic field. The former determines the power dissipation and the latter limits the attainable accelerating field. The followings are the potential advantages of HTS over LTS in cavity application.

i). **Lower surface resistance**. With Nb at 4 K and 500 MHz, the surface resistance R_s is around 25 nΩ at low field levels with typical quality factor $Q_0 = 10^{10}$ and geometrical factor $\Gamma = 250\ \Omega$. The R_s increases to around 250 nΩ and Q_0 decreases to 10^9 at the accelerating field gradient $E_{acc} = 10$ MV/m[3,11]

corresponding to the surface magnetic field $H_s = 4 \times 10^4$ A/m. At low field levels, HTS materials would have lower R_s than that of LTS materials if R_s of HTS exhibits the similar temperature dependence as LTS, and if the residual surface resistance of HTS can be suppressed to a sufficiently low value. It is also important that the surface resistance must remain almost insensitive to rf field increased up to the useful accelerating field.

ii). **Higher critical magnetic field** . With Nb, the maximum possible accelerating field allowable from theoretical considerations is 60 MV/m[12]. This ultimate limit is based on the RF critical magnetic field, equal to the superheating critical field[13], and related to the thermodynamic critical field H_c. From lower and upper critical field measurements in the best HTS materials, it is estimated that the thermodynamic critical field (H_c) is likely to be as high as 1.16×10^6 A/m[14] i.e. more than 5 times higher than that for Nb ($H_c = 2 \times 10^5$ A/m). Correspondingly, postulating the same inter-relationships between critical fields as with LTS, i.e. $H_{RF} \approx 0.75\ H_c$ for $\kappa >> 1$, the RF critical magnetic field H_{RF} for YBCO is expected to be 8.7×10^5 A/m, more than 3 times that of Nb ($H_{sh} = 2.4 \times 10^5$ A/m). These numbers indicate the future possibility of accelerating gradients as high as 200 MV/m. However, the performance of accelerator cavities is usually far below limits imposed by the fundamental RF critical field. Problems such as field emission are dominant. Present day Nb cavities provide 5 – 10 MV/m for today's particle accelerators[11,15]. Much research is in progress on advancing cavity performance towards theoretical capabilities (60 MV/m), particularly in

suppressing field emission. With new surface treatments evolving from these efforts, Nb test cavities approach 30-40 MV/m[11] at KEK. In the case of HTS, this situation may be similar or more severe. Even though a potential accelerating gradient of HTS is higher than that of Nb, the field dependent increase of R_s should be minimised before confronting other difficulties such as field emission.

iii). **Lower cost**. The increased operating temperature offered by HTS could reduce the capital cost of a large accelerator through reduction in cryogenic system costs. In addition, higher temperatures will lower the operating cost and increase the performance reliability of accelerator cavities and their cryogenic systems. Accompanying higher heat capacities will improve thermal stability.

1.3 Study plan

1. **Copper substrates.** For cavity application, HTS films should be deposited onto large-area metallic substrates of complex shape. Since the thermal conductivity of HTS materials is rather low, heat must be released through the substrate to keep the film in a superconducting state even under a high field level. For example, at 10K, the thermal conductivity for polycrystalline $YBa_2Cu_3O_7$ is only about 3 W/mK, more than 2 orders lower than Nb[16]. However, the use of polycrystalline metallic substrates makes the orientation of HTS films difficult, because the orientation of HTS films is governed by the substrate structure. High-quality HTS films grow on single crystalline dielectric substrates more easily than on polycrystalline metallic substrates.
2. **Precise measurement of R_s.** The surface resistance R_s is a key parameter for cavity application and should be measured precisely. The host-cavity method suitable for large area samples is used to measure R_s of YBCO films with 36 mm in diameter. The temperature dependence of R_s is measured with a copper host-cavity. In order to improve the measurement accuracy at low temperature, a niobium host-cavity is used to calibrate the data obtained by a copper host-cavity.
3. **Field dependence of R_s.** Even under high rf fields, the surface resistance of HTS films should be low enough to be competitive with Nb. However, for HTS, the lower critical field for the weak links, H_{c1j}, is quite low, even lower

than 80 A/m, so that beyond H_{c1j} the surface resistance would increase with increasing of rf field. Therefore, it is very important to study the microwave field dependence of the surface resistance for HTS films. The measurement system is prepared in which the cavity input power is controllable from 0.1 mW to 10 W, yielding the cavity surface magnetic fields up to 1000 A/m.

4. **Effect of texturing on R_s.** Due to the anisotropy conduction for HTS, texturing of the c-axis normal to the film surface is inevitable for microwave applications to reduce the surface resistance. For cavity application, the effect of the a-b plane texturing on the surface resistance, especially on its field dependence, should be investigated. We prepare two groups of HTS films, a-b plane well textured and weakly textured, and measure the temperature dependence and microwave field dependence of their surface resistance.

1.4 HTS materials

Before the details of experiment are described, it is useful to review knowledge about HTS materials. Various oxide superconductors with perovskite($CaTiO_3$)-like structure[17] as shown in Fig. 1.1 have been found until now.

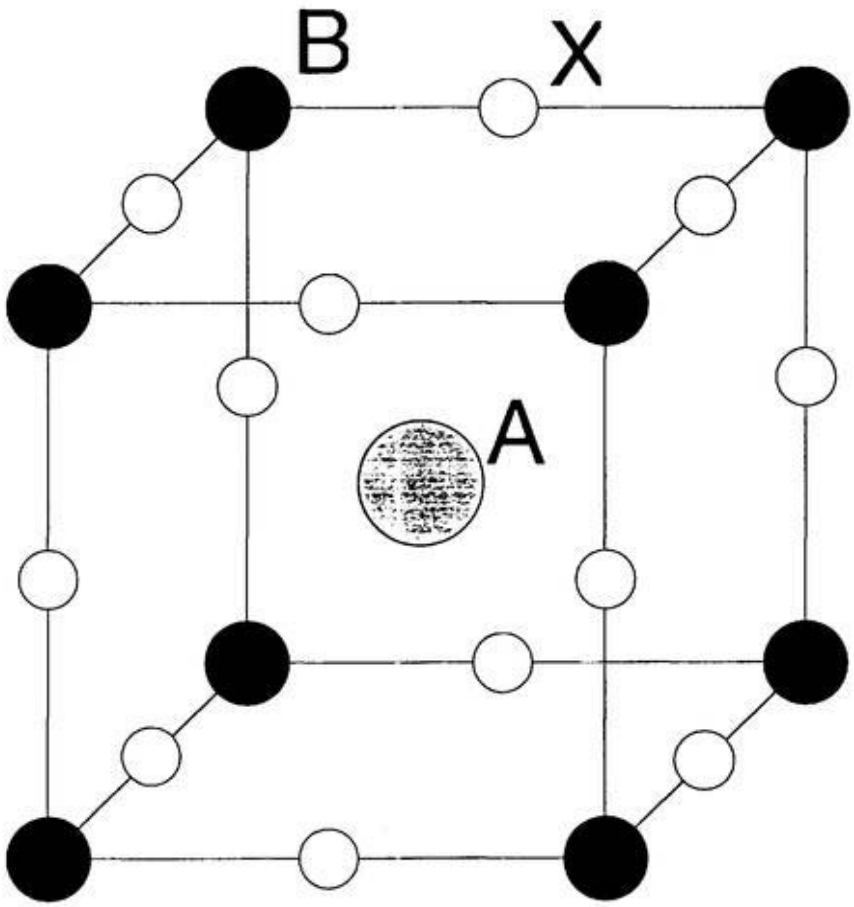

Figure 1.1 Drawing of the perovskite crystal structure, where A and B are metallic cations and X is a non-metallic anion. The YBCO unit cell is composed of three of these perovskite unit cells stacked: the center cell has Y as the A cation, and the top and bottom cells have Ba as the A cation. In both cases, Cu is the B cation and O is the X anion, as shown in Figure 1.2.

The $YBa_2Cu_3O_{7-\delta}$(YBCO) compound was discovered in 1987[4], shortly after the discovery of the first high T_c ceramic superconductor, $(La,Ba)_2CuO_{4-x}$(Tc = 38 K)[5]. Many researchers also refer to $YBa_2Cu_3O_{7-\delta}$, as 123 compound. The 123 phase has a perovskite structure, defined as the basic compound formula ABX3, where A and B are metallic cations and X is a non-metallic anion (Figure 1.1). The superconducting phase is orthorhombic (a=3.819Å, b=3.886Å, c=11.68Å), and the de-oxygenated insulating phase is tetragonal (a=3.889Å, c=11.84Å). The tetragonal to orthorhombic transition occurs during cooling. Any remaining impurity phase will contribute to residual microwave losses. Moreover, the T_c of the oxide superconductors depends sensitively on the oxygen content and on metallic impurities. Contaminations and atomic disorder at the surface should also enhance the surface resistance.

The 123 structure consists of two Cu-O chains in the a-b plane, sandwiching the BaO, Y and kinked CuO2 planes, (Figure 1.2). Current conduction is anisotropic, flowing primarily along the CuO2 planes (a-b planes) rather than along the c axis. Oxygen concentration controls the key 123 phase properties: it determines whether the sample is tetragonal and insulating, or if the sample is orthorhombic and superconducting.

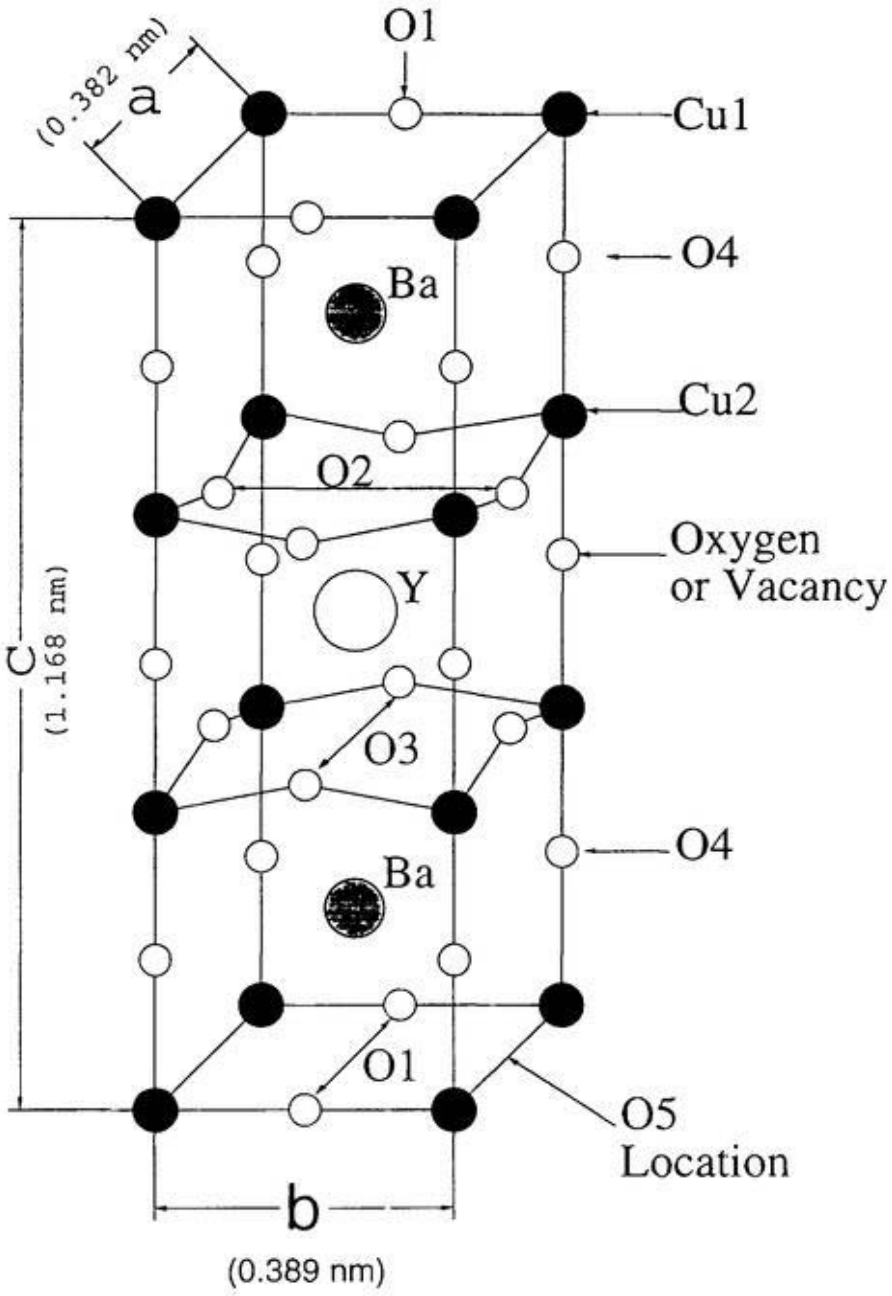

Figure 1.2. Drawing of the YBCO unit cell, orthorhombic and fully oxygenated to O7. The CuO2 planes are kinked. Vacancies for O<7 occur mainly at the O1 and O5 locations, with some on O4 as well. Drawing from [p.105 of Ref. 2].

Table 1-1. HTS materials

Material	abb.	T_c (K)	Unit-Cell Dimensions
$La_{2-x}Ba_xCuO_4$	(La214)		$a \approx b \approx 3.8$ Å, $c \approx 13.2$ Å
$Y_1Ba_2Cu_3O_7$	(YBCO) (Y123)	89-95	$a \approx b \approx 3.8$ Å, $c \approx 11.7$ Å
$Nd_1Ba_2Cu_3O_7$			$a \approx b \approx 3.8$ Å
Bi-Compound: ($Bi_2Sr_2Ca_1Cu_2O_8$)	(BSCCO) (B2212)	105-120	$a \approx b \approx 3.8$ Å, $c \approx 30$ Å
Tl-Compound: ($Tl_2Ba_2Ca_2Cu_3O_{10}$)	(TBCCO) (T2223)	110-125	$a \approx b \approx 3.8$ Å, $c \approx 30$ Å
Hg-Compound: ($Hg_1Ba_2Ca_2Cu_3O_8$)	(HBCCO) (H1223)	136	

LaBaCuO: Lanthanum-Copper Oxide

YBCO: Yttrium-Barium-Copper Oxide

BSCCO: Bismuth-Strontium-Calcium-Copper Oxide

TBCCO:Thallium-Barium-Calcium-Copper Oxide.

HBCCO: Mercury- Barium-Calcium-Copper Oxide

In the past, a lot of different kinds of HTS materials have been discovered. Some parameters for typical HTS materials are listed in the above table. In this study aiming at application of HTS materials to accelerator cavities, we must choose the most suitable HTS material available at present. Even though the transition temperature of

$YBa_2Cu_3O_{7-x}$ (YBCO) is not the highest in HTS family, YBCO was selected because of the following advantages over other materials.

1). **Simplest structure in HTS family**. The crystal structure of YBCO is the simplest among the HTS family such as Bi-, Tl- and Hg-compounds.

2). **Best known characteristics**. YBCO has been investigated mostly and its characteristics are well known.

3). **Lower residual resistance**. Single phase of YBCO materials can be obtained easily in comparison to others. Any remaining impurity phase will contribute to residual microwave losses, and enhance the surface resistance. In general, Bi- and T- compounds have higher residual surface resistance than YBCO.

4). **Sharp rf transition**. YBCO exhibits the sharpest rf transtion due to superior phase purity. This merits more than offsets its lower critical temperature of Bi- and T-compounds.

1.5 R_s Measurement Methods

A key material property, which determines HTS suitability for practical applications especially for cavity application, is the surface resistance R_s. Since the discovery of HTS a large variety of techniques have been developed to measure the surface impedance of HTS samples. Usually, the lower the surface resistance is, the more complicated the technique is. Depending on the size of samples to be measured, these methods may be divided into two groups as listed in Table 1-2. In order to measure physical properties of a single crystal which is usually small in size, the techniques such as a split-ring resonator technique[18], a hot-finger resonator technique[19] or a host-cavity technique[20-22] are adopted. For HTS films with big size, a parallel-plate resonator technique[23], a dielectric resonator technique[24] or a host cavity technique[25-29] are adopted.

Table 1-2. Surface impedance measurement methods

	Methods for measurement of small size samples		Methods for measurement of big size samples	
	Split-ring resonator	Fig. 1.3 (Ref. 18)	Parallel-plate resonator	Fig. 1.6 (Ref. 23)
	Hot-finger resonator	Fig. 1.4 (Ref. 19)	Dielectric resonator	Fig. 1.7 (Ref. 24)
	Host-cavity technique	Fig. 1.5 (Ref. 20)	Demountable cavity or host-cavity technique	Fig. 1.8 (Ref. 29)

The YBCO samples prepared for the study have the diameter of 36 mm. Because of the large sample size, we must select one method from those listed in the right column of Table 1-2. We adopted the demountable cavity method because of the following advantages. First, it can be operated in simple resonant mode. Second, no dielectric material in the cavity is inserted, so that some uncertainty from the temperature-dependent permittivity of the dielectric material was avoided. Third, because the cavity is the closed structure, there is no escaping microwave from the cavity, which will contribute to the accuracy of measurements. The demountable cavity operated in TE_{011} mode was employed, and the cavity dimension was determined by the sample size. The cavity dimension, i.e., 33 mm in diameter and 19 mm in length, and the operation in TE_{011} mode determined the resonance frequency around 13.6 GHz[30]. The principle and the measurement procedure will be described in detail in Chapter 3. The reason why we employed two demountable cavities (copper cavity and niobium cavity) will also be explained in Chapter 3.

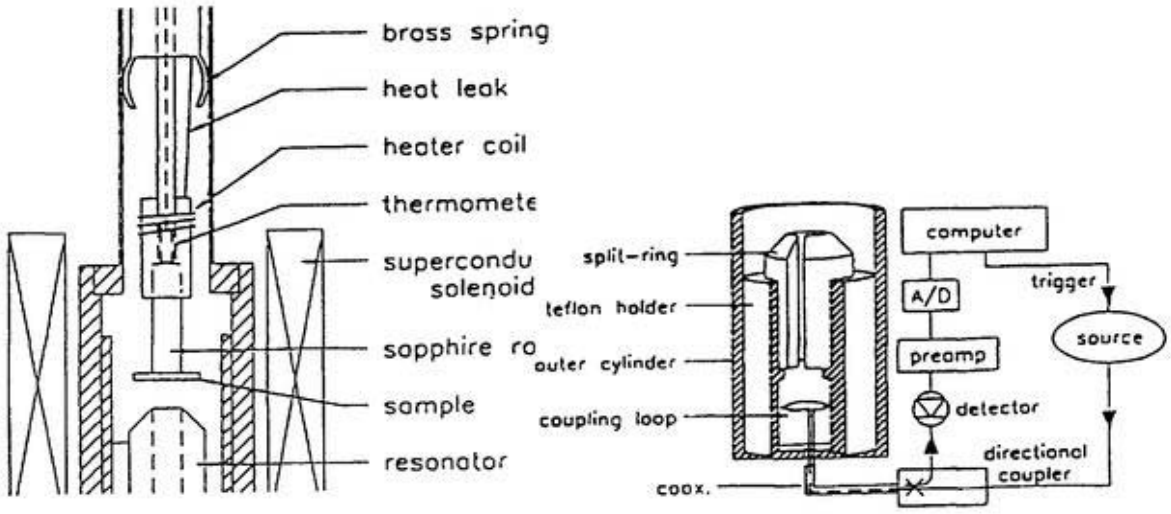

Fig. 1.3. Split-ring resonator from Ref. [18]. Left). Schematic view of the holder used to position samples near the split-ring resonator. The brass springs keep the sample holder centered, allow vertical motion of the sample towards and away from the resonator, and provide cooling via the copper heat leak. The sample and resonator chamber is surrounded by a superconducting solnoid in a bath of liquid helium. Right). Schematic view of the circuit used for measurements with copper split-ring resonators. The outer cylinder and Teflon holder have been cut away to reveal the resonator. Measurements of the resonance are made in a reflectance configuration with the use of a single coupling loop and directional coupler.

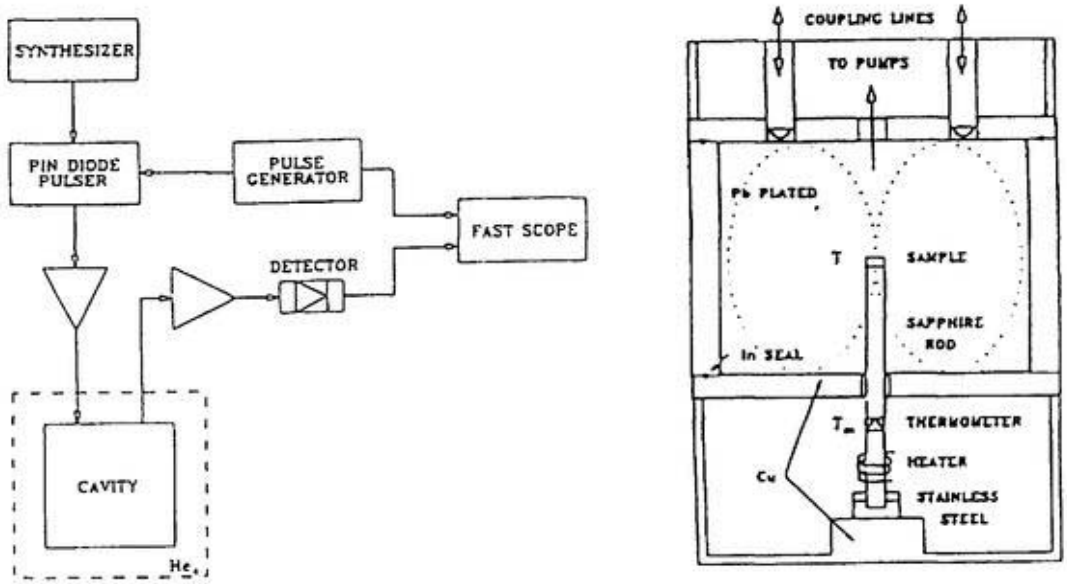

Fig. 1.4. Hot-finger resonator from Ref. [19]. Block diagram of the experimental apparatus. The inset shows the details of the cavity configuration. The bottom plate has one centrally located hole, through which the sample is inserted into the cavity. The sample was mounted on a sapphire rod. Support and adjustment of the rod was provided by a stainless-steel tube which was brazed to the removable Cu bottom plate. Microwaves were coupled into and out of the resonator from the top.

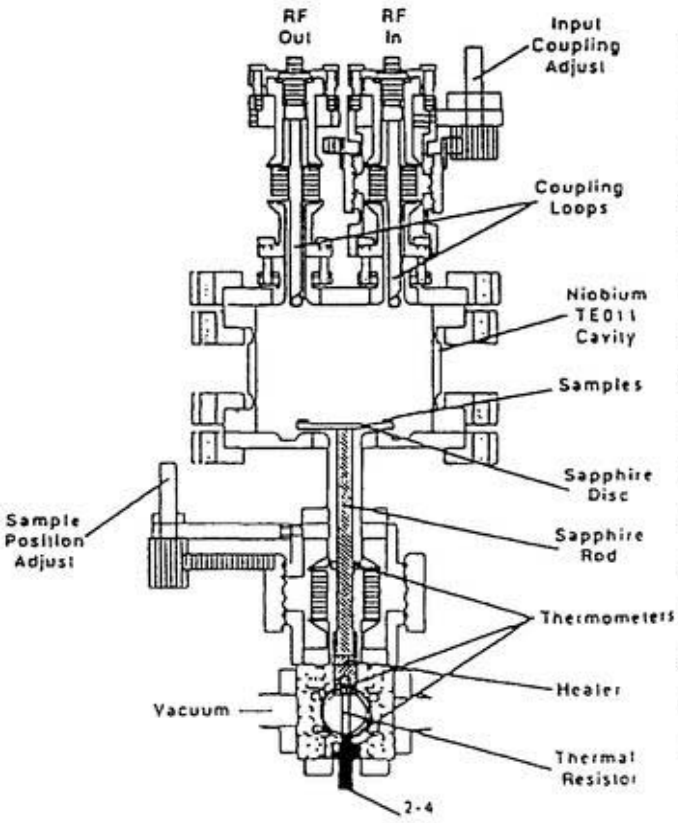

Fig. 1.5. Host cavity from Ref. [20]. A TE_{011} niobium cavity was employed to measure the microwave surface resistance of HTS samples. The samples are introduced into the high Q cavity via a sapphire rod through a niobium cutoff tube aligned along the cavity axis. The rod is coupled by a thermal resistor to the helium bath. A heater at the base of the sapphire rod and thermometers in contact with the rod control and monitor the temperature of the sample. The heater and bath thermometers are placed well beyond RF cutoff.

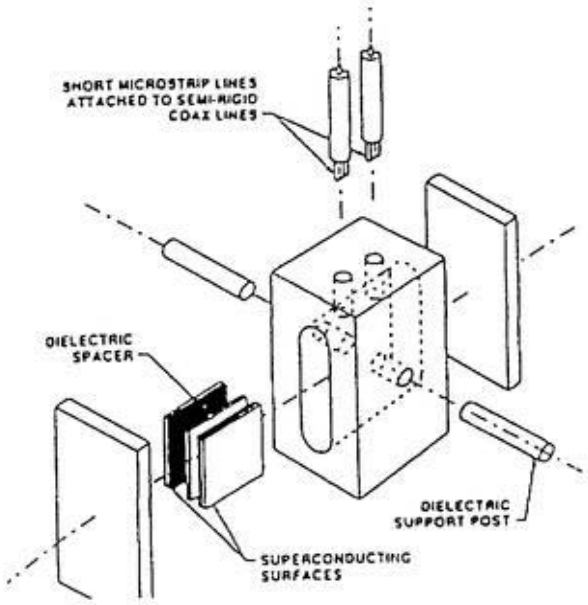

Fig. 1.6. Parallel-plate resonator from Ref. [23]. Expanded view of the measurement configuration. The material under test is clamped within the test chamber by two dielectric posts that are spring loaded by components (not shown) exterior to the test chamber. The test chamber is machined from brass and is gold plated to provide low surface loss.

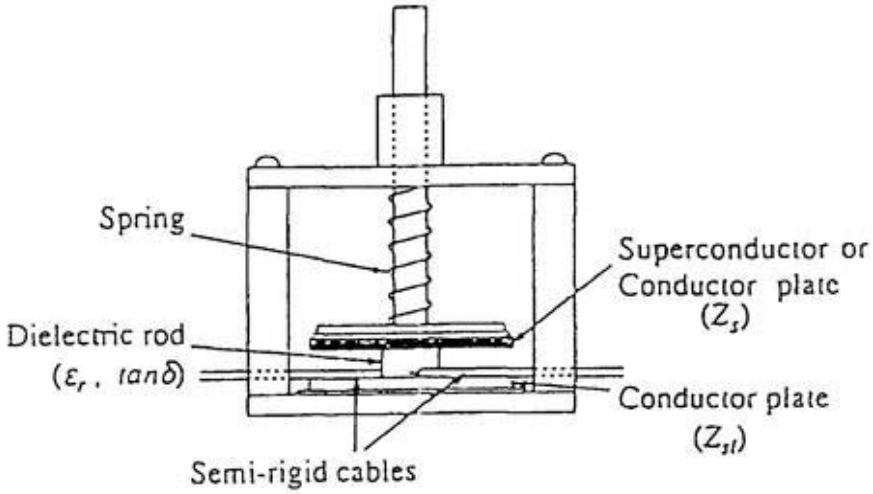

Fig. 1.7. Dielectric resonator from Ref. [24]. Figure shows an dielectric resonator apparatus which is set in the cryostat. The resonator contains a copper cylinder, a copper plate, the HTS plate, and the

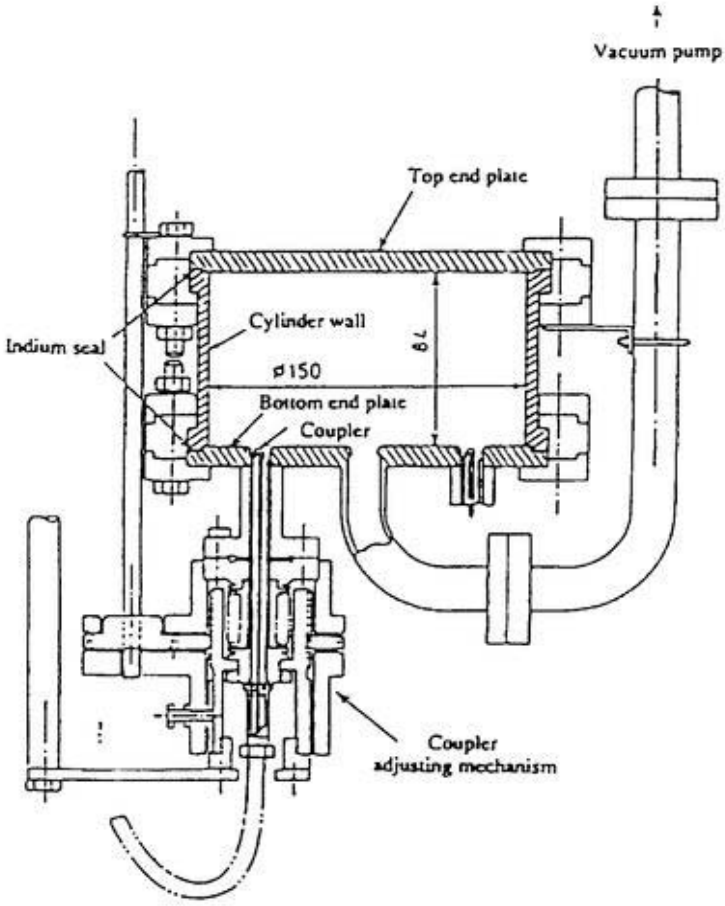

Fig. 1.8. Demountable cavity from Ref. [29]. It consists of a top plate, a cylinder wall and a bottom plate. The bottom plate has two rf and one vacuum port. Microwaves are loop-coupled into and out of the cavity. The coupling to the cavity can be varied by moving the line along the axis of the cavity with a fine driving mechanism. The central pumping hole in the bottom plate contributes to breaking the degeneracy between the TE_{011} and TM_{111} modes. The top endplate can be replaced by the HTS samples.

References

1. Vladimir Z. Kresin and Stuart A. Wolf, *Fundamentals of Superconductivity*, Plenum Press, New York and London, p.3 (1990).
2. James D. Doss, *Engineer's Guide to High-Temperature Superconductivity*, John Wiley & Sons, p.148 (1989).
3. "*Superconductivity in Particle Accelerators*", ed. S. Turner, CERN 96-03 (1996).
4. G. Bednorz and K. A. Müller, Z. Phys. B. **64**, 189 (1986).
5. M. K. Wu, J. R. Asburn, C. J. Torng, P. H. Hor, R. L. Meng, L. Gao, Z. J. Huang, Y. Q. Wang, and C. W. Wu, Phys. Rev. Lett. **58**, 908 (1987).
6. Y. Zhang, W. Zander, J. Schubert, F. Rüders, H. Soltner, M. Banzet, N. Wolters, X. H. Zeng, and A. I. Braginski, Appl. Phys. Lett. **71**, 704 (1997); F. Schmidl, S. Linzen, S. Wunderlich, and P. Seidel, Appl. Phys. Lett. **72**, 602 (1998).
7. J. Chen, H. Myoren, K. Nakajima, T. Yamashita, and P. H. Wu, Appl. Phys. Lett. **71**, 707 (1997).
8. Y. Hakuraku and Z. Mori, J. Appl. Phys. **73**, 309 (1993).
9. H. Yamasaki, K. Endo, S. Kosaka, M. Umeda, S. Yoshida, and K. Ka-jimura, Phys. Rev. Lett. **70**, 3331 (1994); Phys. Rev. B **50**, 12 959 (1994).
10. H. Yamasaki, K. Endo, S. Kosaka, M. Umeda, S. Yoshida, and K. Ka-jimura, Phys. Rev. Lett. **70**, 3331 (1994); Phys. Rev. B **50**, 12 959 (1994).
11. K. Saito, P. Kneisel, E. Kako, T. Shishido, S. Noguchi, M. Ono, and Y. Yamazaki, LINAC98 XIX international Linac Conf., Chicago, USA. August 23-28, (1998).

12. W. Weingarten, p. 324, CERN 92-03 (1992).

13. J. Matricon and D. Saint-James, Phys. Lett. **24A**, 241 (1967).

14. U. Welp, W. K. Kwok, G. W. Crabtree, K. G. Vandervoot, and J. Z. Liu, Phys. Rev. Lett. **62**, 1908 (1989).

15. S. Mitsunobu, K. Asano, T. Furuya, Y. Ishi, Y. Kijima, K. Ohkubo, T. Tajima and T. Takahashi, KEK Preprint 93-208 (1994).

16. G. Müller, p.270, *Proceedings of the 4th Workshop on RF Superconductivity* 1989, KEK Report 89-21, (1990).

17. Charles P. Poole, Jr., Timir Datta, Horacio A. Farach, *Copper Oxide Superconductors*, p.73 (John Wiley & Sons 1988).

18. D. A. Bonn, D. C. Morgan, and W. N. Hardy, Rev. Sci. Instrum. **62**, 1819 (1991).

19. S. Sridhar and W. N. Kennedy, Rev. Sci. Instrum. **59**, 531 (1988).

20. D.L. Rubin, K. Green, J. Gruschus, J. Kirchgessner, D. Moffat, H. Padamsee, J. Sears, Q. S. Shu, L. F. Schmeemeyer, and J. V. Waszczak, Phys. Rev. B **38**, 6538 (1988).

21. M. Hagen, M. Hein, N. Klein, A. Michalke, G. Müller, H. Piel, and R. W. Röth, J. Magn. Mat. **68**, L1 (1987).

22. M. Kobayashi, K. Okabe, S. Tanuma, I. Sankawa, M. Sato, T. Konaka, and K. Ishihara, IEEE Trans. Magn. **25**, 997 (1989).

23. R. C. Taber, Rev. Sci. Instrum. **61**, 2200 (1990).

24. Y. Kobayashi, T. Imai, and H. Kayano, IEEE Trans. Microwave Theory Tech. **27**, 1530 (1991).

25. J. S. Martens, J. B. Beyer, and D. S. Ginly, Appl. Phys. Lett. **52**, 1822 (1988).

26. H. Piel, M. Hein, N. Klein, U. Klein, A. Michalke, G. Müller, and A. Ponto, Physica C **153-155**, 1604 (1988).

27. N. Klein, G. Müller, H. Piel, B. Roas, L. Schultz, U. Klein, and M. Peiniger, Appl. Phys. Lett. **54**, 757 (1989).

28. C. L. Bohn, J. R. Delayen, U. Balachandran, and M. T. Lanagan, Appl. Phys. Lett. **55**, 304 (1989).

29. E. Ezura, K. Asano, H. Hayano, K. Hosoyama, S. Inagaki, S. Isagawa, M. Kabasawa, Y. Kojima, S. Kosuge, S. Mitsunobu, T. Momose, K. Nakada, H. Nakanishi, Y. Shimbo, T. Shishido, K. Tachikawa, T. Takahashi, and K. Yoshihara, Jpn. J. Appl. Phys. **32**, 3435 (1993).

30. Jian-Fei Liu, K. Asano, E. Ezura, M. Fukutomi, S. Inagaki, S. Isagawa, K. Komori, H. Nakanishi, M. Tosa, and K. Yoshihara, Proc. 1995 Particle Accelerator Conf., Dallas, 1995, p. 1652 (1995).

2. Fabrication of films

2.1 Introduction

Application of high-T_c superconductor films for accelerator cavities requires the deposition of films on relatively large-area (~10^2 ~ 10^3 cm^2) metallic substrates[1]. We chose copper as a substrate material[2,3,4] because it has high thermal conductivity and good machinability. As a buffer layer for deposition of YBCO films on copper substrates, we employed YSZ/Cr double layers, where YSZ is an acronym of yttriz-stabilized-zirconia. The Chromium underlayer was found to be essential to protect copper against oxidation, resulting in good adhesion of the YSZ layer on copper[3,4]. The textured YSZ layer helps the YBCO film to be textured. Copper substrates, 36 mm

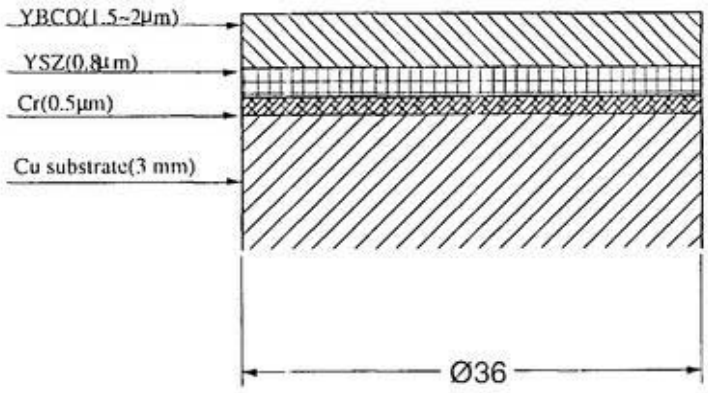

Fig.2.1. The multilayer structure of YBCO films

in diameter disk with a thickness of 3 mm, were polished to a mirror finish. They were then ion-plated with the chromium layer of about 0.5 μm, and subsequently deposited with the in-plane textured YSZ buffer layer of 0.8 μm thick by using a modified bias sputtering technique. As shown in Fig. 2.1, YBCO films were deposited onto the copper substrates pre-coated with YSZ/Cr buffer layer by using laser ablation technique. Due to the anisotropy of YBCO, i.e. the conductivity in a-b plane much better than that along c-axis, c-axis perpendicular to the surface is inevitable to reduce the surface resistance and its field dependence for the accelerator cavity application. In addition, the texturing in a-b plane of YBCO films is possible on well-textured YSZ buffer layer.

2.2 YSZ buffer layer

Before YSZ deposition, a thin chromium underlayer was ion-plated on the copper substrate to ensure good adhesion of YSZ films. The texturing of YSZ is crucial to the ab-plane texturing of YBCO films. The texturing of YSZ layer was obtained by using a modified bias sputtering(MBS) technique[3]. Figure 2.2 and 2.3 show a pair of specially devised electrodes installed in the large-area MBS system. The degree of in-plane texturing varies depending on the sample position. The poorer texturing part over the film is located directly above the center between a pair of adjacent auxiliary

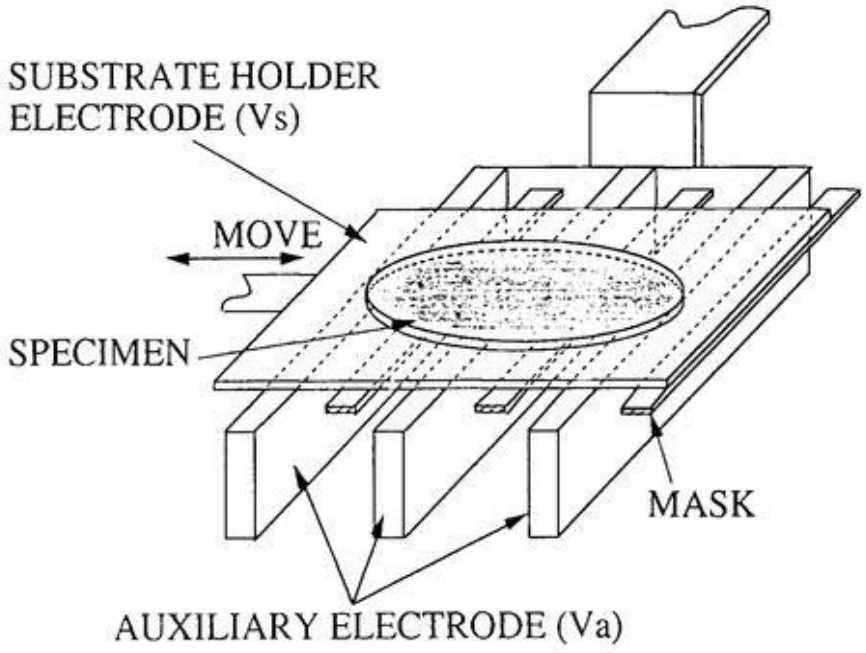

Fig. 2.2. Large-area MBS system showing three auxiliary electrode plates. The number of plates for the auxiliary electrode is changed depending on the substrate area to be coated (From [6].).

electrodes, since the glancing-angle ion bombardment during deposition is one of the requirements for achievement of in-plane texturing. Masks were placed at these positions in order to avoid the growth of poor-oriented films in this area, where Ar^+ ions impinge on a film not obliquely but at almost right angles. Meanwhile, a movable substrate holder electrode was used to slide the substrate horizontally during deposition, so that a textured film can grow on the masked area after a period of deposition. Finally the whole area of the substrate was successfully covered with in-plane textured YSZ thin films. Using this equipment, we made an attempt to obtain YSZ films with in-plane texturing over the whole surface of the sample.

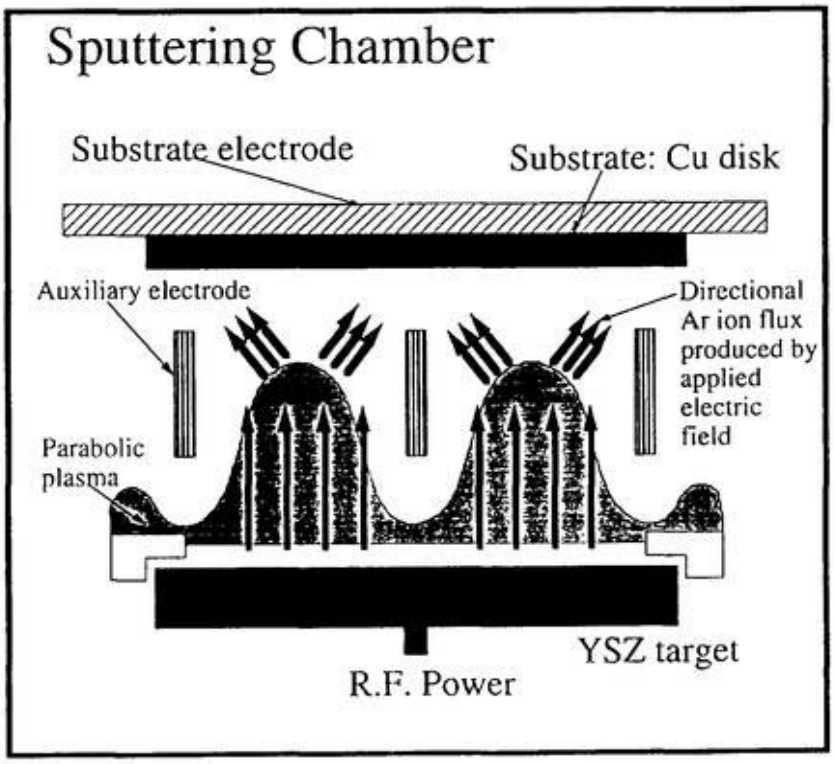

Fig. 2.3 Schematic drawing of large-area MBS system (From [6].).

2.3 Deposition of YBCO films

The copper substrates pre-coated with YSZ/Cr buffer layer were used for deposition of YBCO films using the laser ablation technique[4]. Figure 2.4 shows the schematic view of KrF-excimer pulsed laser deposition(PLD) system. In order to obtain uniform large area YBCO films, the mirror was oscillated so that an excimer laser beam reflected from the mirror could be scanned on the rotating target surface.

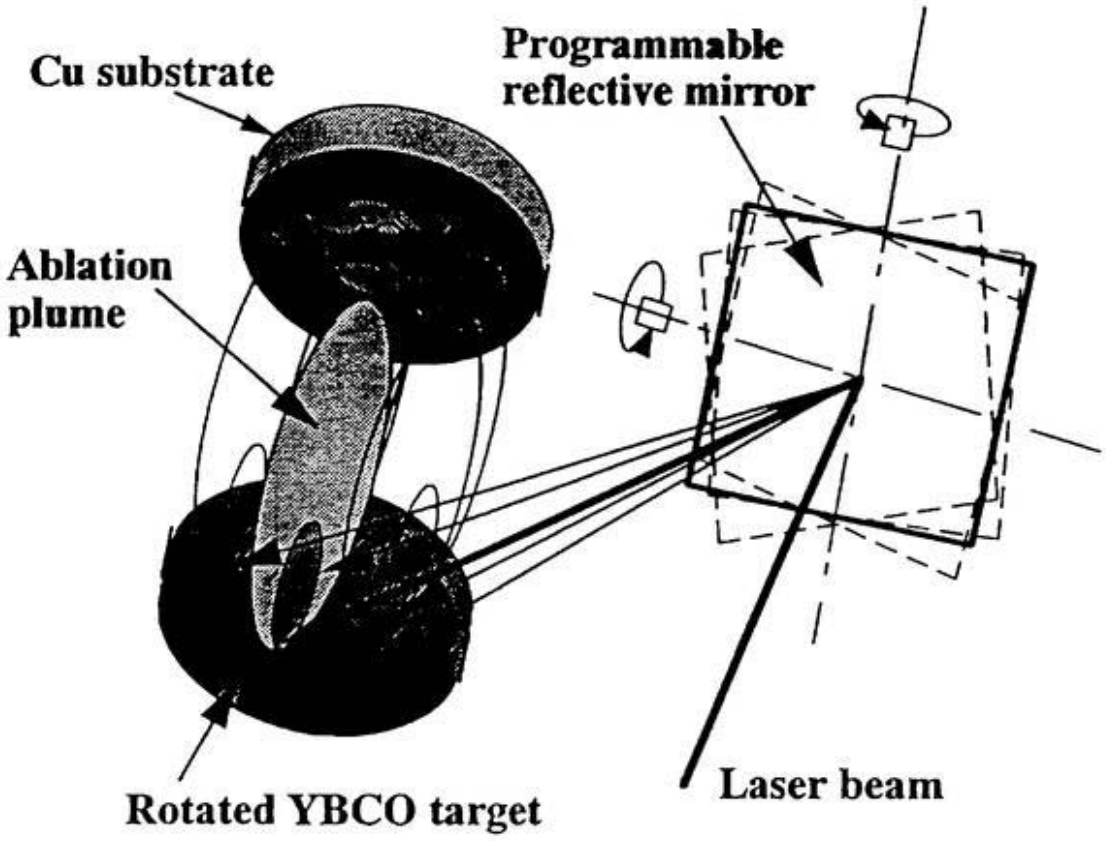

Fig. 2.4. Schematic view of KrF-excimer pulsed laser deposition(PLD) system (From [6].).

2.4 The Texture of YSZ and YBCO

In order to characterize the in-plane texturing of the films, we carried out an X-ray Pole figure measurement using the Schulz reflection method[5]. A pole figure is generally used for determining the texture of polycrystalline material. The details about x-ray pole figure is described in Appendix A. Figure 2.5(a) shows a typical pole figure

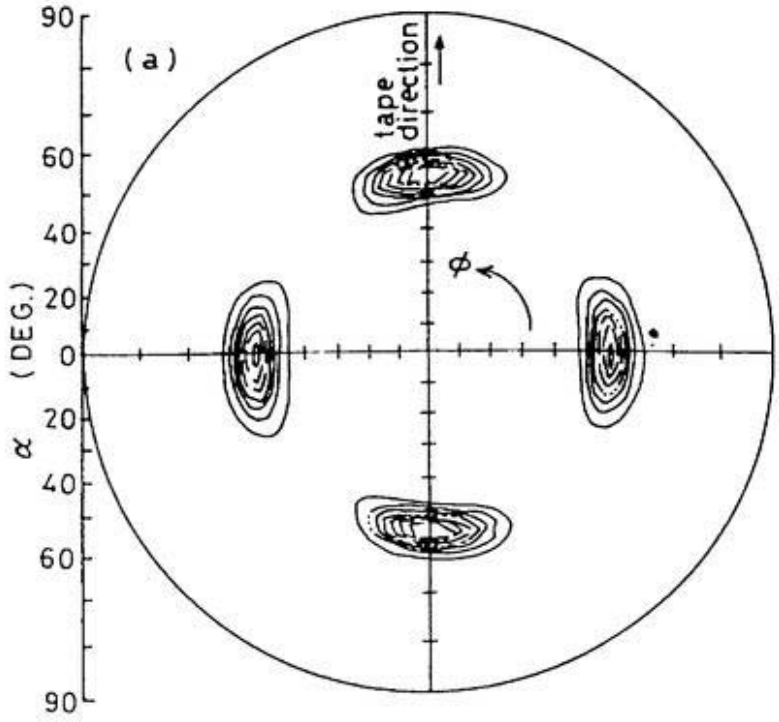

Fig. 2.5(a). An example of a typical pole figure for an YSZ film with an apparent in-plane grain orientation (From [6].).

for an YSZ film with an apparent in-plane grain orientation. For the cubic YSZ structure with the (200) plane parallel to the specimen surface, if the film is tilted relative to the X-ray beam by $\alpha = 54.7^{\circ}$, then the (111) peak can be detected at $2\theta = 30.1^{\circ}$ (CuK_{α}), with (111) becoming the diffraction plane. As is seen in Fig. 2.5(b), the intensities of the diffracted X-ray beam shows a maximum at the angle α mentioned above, with peaks at 90° in the ϕ direction. Figure 2.5(b) gives what is called a ϕ-scan of the same specimen in Fig. 2.5(a), which indicates the (111) intensity plotted as a function of the angular rotation in the plane of the substrate.

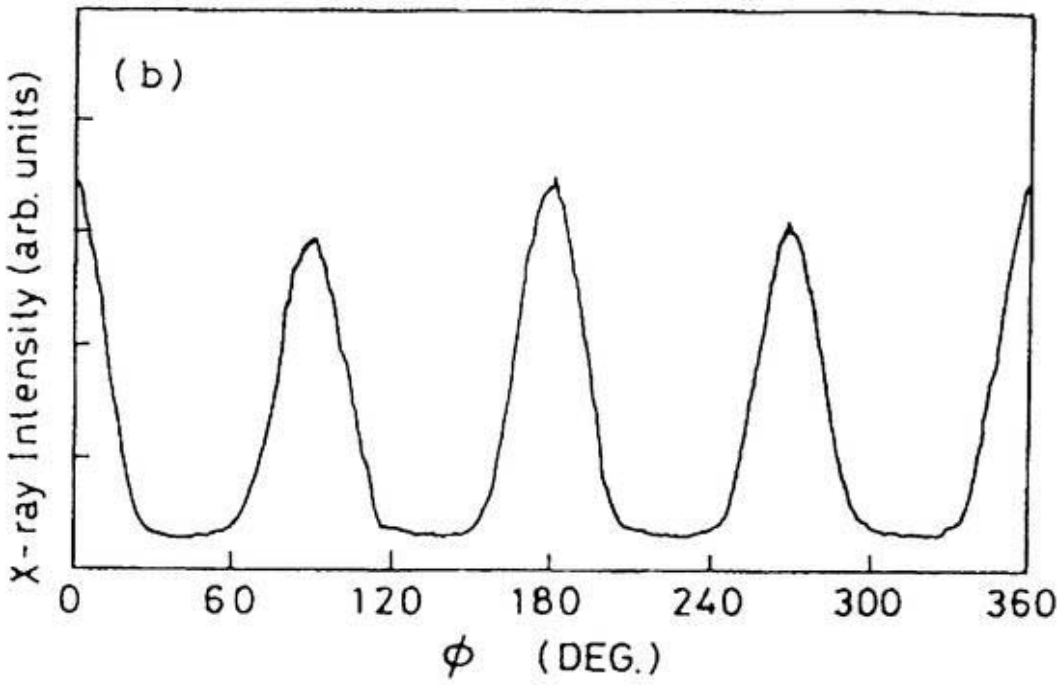

Figure 2.5(b): An example of a typical pole figure for an YSZ film with an apparent in-plane grain orientation. The (111) ϕ-scan is shown. ϕ is varied while $2\theta = 30.1^{\circ}$ (CuK_{α}) and the tilt angle $\alpha = 54.7^{\circ}$ (From [6].).

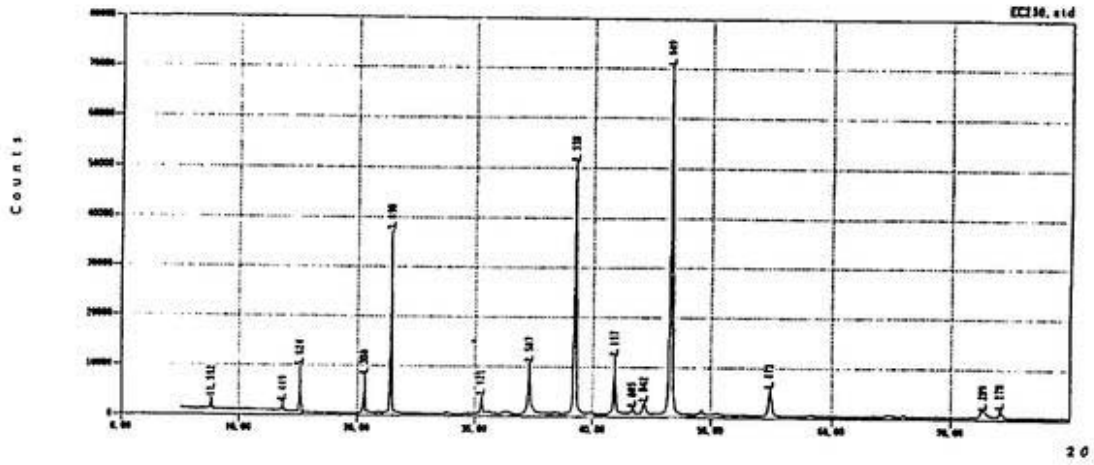

Figure 2.6: The X-ray diffraction patterns exhibit a clear pattern of sharp (00n) lines typical for complete c-axis orientation (From [6].).

Three YBCO films EC230, EC231 and EC232 were prepared for the rf field dependence measurements described in Chapter 7. The c-axis of all the three YBCO films is confirmed to be normal to the substrate plane by the X-ray diffraction. The X-ray diffraction patterns, shown in Fig. 2.6, exhibit a clear pattern of sharp (00n) lines typical for complete c-axis orientation. Degree of a-b plane texturing for EC230, EC232 and EC232 was expected to be untextured, well textured and weakly textured, respectively. However, poor orientations in the a-b direction for all three samples were indicated by X-ray pole figure as shown in Fig.2.7 (a), (b) and (c), respectively. Figure 2.8 shows the sample of pole figure for (a) in-plane textured YBCO and (b) in-plane untextured YBCO films prepared on copper substrates with a YSZ buffer layer.

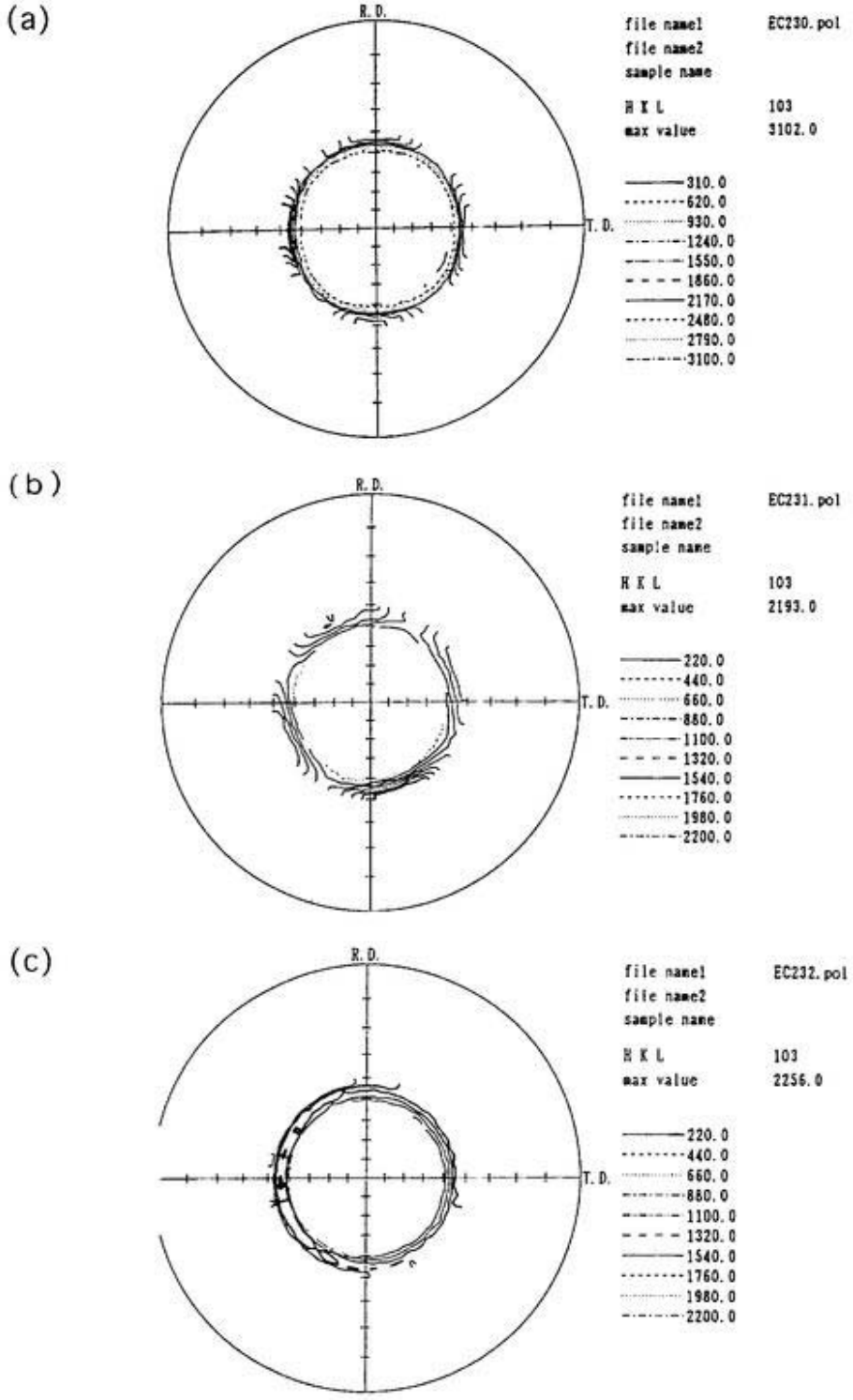

Fig. 2.7(a), (b) and (c). X-ray pole figures for samples EC230, EC231 and EC232, respectively, in which poor or weakly texturing in a-b plane is indicated (From [6].).

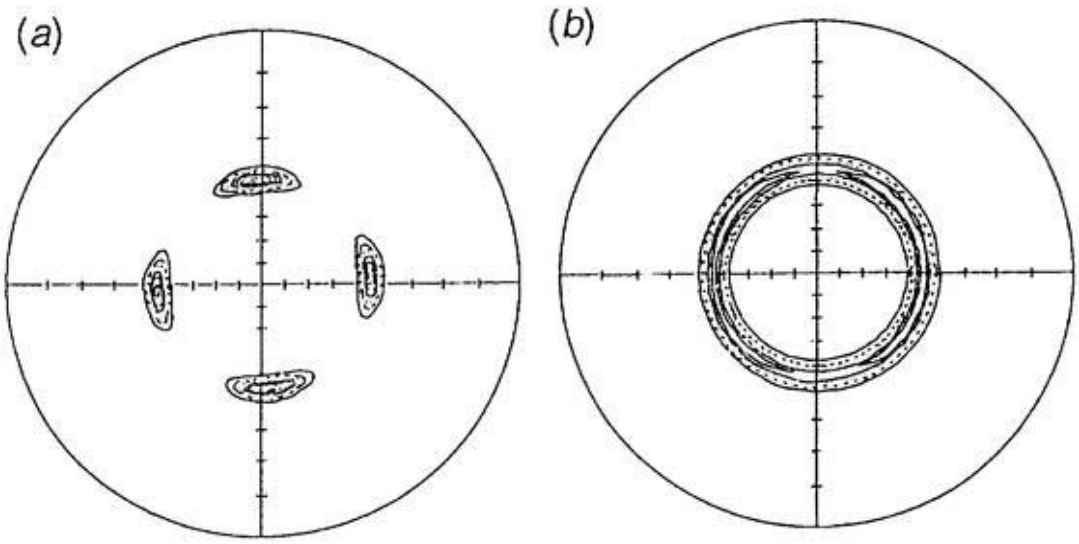

Fig. 2.8. Example of pole figures (a) for in-plane textured YBCO and (b) for random in-plane textured YBCO films prepared on copper substrates with a YSZ buffer layer(From [6].).

2.5 Surface morphology of YBCO films

Scanning electron microscope (SEM) pictures were taken for these three YBCO films. Figure 2.9 (a), (b) and (c) show the surface morphologies of YBCO film samples EC230, EC231 and EC232, respectively. These SEM images revealed that cracks exist clearly for sample EC230, and grain size for EC231 and EC232 is about 0.6~0.8 μm.

Fig. 2.9(a). SEM image of YBCO sample EC230 (From [6].).

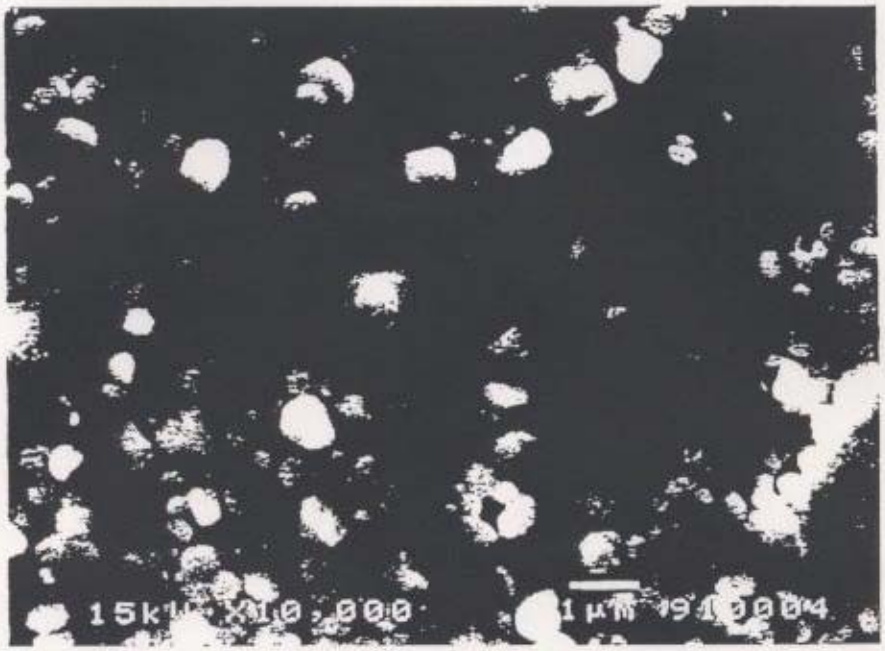

Fig. 2.9 (b). SEM image of YBCO sample EC231 (From [6].).

Fig. 2.9(c). SEM image of YBCO sample EC232 (From [6].).

References

1. E. Ezura, K. Asano, H. Hayano, K. Hosoyama, S. Inagaki, S. Isagawa, M. Kabasawa, Y. Kojima, S. Kosuge, S. Mitsunobu, T. Momose, K. Nakada, H. Nakanishi, Y. Shimbo, T. Shishido, K. Tachikawa, T. Takahashi, and K. Yoshihara, Jpn. J. Appl. Phys. **32**, 3435 (1993).
2. M. Fukutomi, S. Aoki, K. Komori, R. Chatterjee, and H. Maeda, Physica C **219**, 333 (1994).
3. M. Fukutomi, M. Saitoh, K. Komori, and K. Togano, Appl. Supercond. **4**, 447 (1996).
4. M. Fukutomi, S. Kumagai, and H. Maeda, Aust. J. Phys. **50**, 381-9 (1997).
5. Cullity, B. D., *Elements of X-ray Diffraction*, Addison-Wesely Publishing Co. Inc., (1978).
6. Figures provided by Prof. M. Fukutomi group at National Research Institute for Metals, Tsukuba, Japan.

3. Theory of surface impedance measurement

3.1 Relevant details of superconductivity

The superconducting phase field is a volume bounded by three critical parameters, the critical current J_c, the critical temperature T_c, and the critical magnetic field strength H_c or flux density B_c. Within this volume, superconducting materials can carry an electric current with zero resistance (a "supercurrent").

There are two basic classes of superconductors in the case of LTS[1,2], known as Type I and Type II. Type I superconductors do not allow the penetration of magnetic flux into their interior, and carry a supercurrent only within a thin layer λ, the penetration depth, of their surface. Type I superconductors are only found as pure elements (e.g. Pb), although there are some elements (e.g. Nb) that are Type II superconductors. At a field known as the lower critical field B_{c1}, magnetic flux penetrates into the interior of Type II superconductors. The magnetic flux enters a Type II superconductor as fluxoids which consist of an integral number of a quantum known as the fluxon, which has a value of 2.07×10^{-15} Wb[p.158, Ref. 2]. A Type II superconductor which contains some penetrated fluxons, but at a density less than the

upper critical flux density B_{c2}, has regions in both the superconducting and normal states, and is said to be in the "mixed" state. Type II superconductors are more useful from a technological point of view than Type I superconductors, because current is carried throughout the bulk, and because of their typically much great upper critical field.

The discovery of superconductivity in copper oxides in 1986[3] has lead to a great body of effort to explain the physical origins of the phenomenon. The commonly accepted mechanism for superconductivity in most LTS materials is phonon-mediated coupling of electrons with opposite spin. The paired electrons, called Cooper pairs, travel through the superconductor without scattering. The classic work of Bardeen, Cooper, and Schriefer[4], now referred to as the BCS theory, describes the electron pairing process leading to a Bose condensation to the superconducting state. The BCS theory explains the general behavior of LTS metals and alloy superconductors very well. However, several features of superconductivity observed in the high-T_c cuprate superconductor are not well explained by the BCS theory.

Fortunately, for most of the practical applications of superconductors, the phenomenological theory based on the London equations and the two-fluid model (or modified two-fluid model) [p.31, Ref. 2] is adequate to understand and provide a conceptual understanding of the response of superconductors to electrical, magnetic, and electromagnetic fields.

3.2 Modified two-fluid model

In the two-fluid model as described in Appendix B, a superconducting current with a carrier density n_s, and a normal current with a carrier density n_n, yield a total carrier density n, $n = n_s + n_n$. Free energy expressions were postulated for the superconducting and normal electrons. Gorter and Casimir found that $n_n/n \propto T^p$, where $p = 4$ is a good fit for Sn, In and Tl and $p = 6$ is a good fit for Hg and Pb. ($p = 4$ is implicitly meant when one mentions the Gorter-Casimir relation.) At temperatures below T_c,

$$n_s / n = 1 - (T / T_c)^4, \tag{3.1}$$

$$n_n / n = (T / T_c)^4. \tag{3.2}$$

At $T = 0$, all of the carriers are superconducting, and the fraction of superconducting charge carriers approaches zero as temperature approaches T_c. The microwave surface impedance with two-fluid model is described in Appendix C.

In measured microwave surface resistance of high-T_c materials, *not a little residual resistance is generally observed.* In order to explain the residual resistance, a modified two-fluid model has been proposed.

We define that n_{res} is the residual charge carrier density[6-9] (*i.e.* nonpairing normal charge carrier density), and that the total carrier density n_t equals the sum expressed as,

$$n_t = n_n + n_s + n_{res}. \tag{3.3}$$

We denote the fractions of the normal carriers, the superconducting carriers and the residual carriers to the total carriers as,

$$n_n/n_t = X_n(T), \tag{3.4}$$

$$n_s/n_t = X_s(T), \tag{3.5}$$

$$n_{res}/n_t = X_{res}, \tag{3.6}$$

where X_{res} is independent of temperature T. Hence,

$$X_n(T) + X_s(T) + X_{res} = 1. \tag{3.7}$$

Similarly, as in the two-fluid model, we assume,

$$n_n/(n_n + n_s) = (T/T_c)^p \equiv t^p, \tag{3.8}$$

$$n_s/(n_n + n_s) = 1 - (T/T_c)^p \equiv 1 - t^p. \tag{3.9}$$

Therefore, we can obtain

$$n_n/n_t = X_n(T) = t^p(1 - X_{res}), \tag{3.10}$$

$$n_s/n_t = X_s(T) = (1 - t^p)(1 - X_{res}). \tag{3.11}$$

3.3 Microwave surface impedance with modified two-fluid model

As given in Eq. (1) of Appendix C, the surface impedance $Z_s = R_s + jX_s$ can be derived from Maxwell's equations as,

$$Z_s = R_s + jX_s = \sqrt{j\mu\omega/\sigma} = (1+j)\sqrt{\mu\omega/2\sigma} \ , \tag{3.12}$$

where $\omega = 2\pi f$ is the angular frequency, σ the conductivity.

In the modified two-fluid model, the conductivity σ consists of three components σ_s, σ_n and σ_{res} attributable to the superconducting carriers, normal carriers and residual nonpairing normal carriers, respectively, and

$$\sigma = \sigma_s + \sigma_n + \sigma_{res} \ . \tag{3.13}$$

Both σ_s and σ_n are defined in the same way as given in Appendix C,

$$\sigma_s = \frac{1}{j\omega\Lambda} = \frac{1}{j\omega\mu\lambda_L^2} = \frac{n_s q_s^2}{j\omega m_s}, \tag{3.14}$$

where Λ is the London constant, λ_L is the London penetration depth, and q_s and m_s are the charge and mass of superconducting carriers, respectively.

$$\sigma_n = \frac{n_n q_n^2}{m_n}\frac{\tau}{1+j\omega\tau} = \frac{n_n q_n^2 \tau}{m_n}\frac{1-j\omega\tau}{1+(\omega\tau)^2}, \tag{3.15}$$

where τ is the relaxation time for electron scattering, q_n and m_n are the electrical charge and mass for the normal carriers. For nonpairing normal charge carriers, we should expect its conductivity σ_{res} expressed in the same form of the normal charge carriers as

$$\sigma_{res} = \frac{n_{res} q_n^2}{m_n} \frac{\tau}{1 + j\omega\tau} = \frac{n_{res} q_n^2 \tau}{m_n} \frac{1 - j\omega\tau}{1 + (\omega\tau)^2}. \tag{3.16}$$

The total conductivity for a superconductor is

$$\begin{aligned} \sigma &= \sigma_1 - j\sigma_2 \\ &= \sigma_s + \sigma_n + \sigma_{res} \\ &= \frac{(n_n + n_{res}) q_n^2 \tau}{m_n} \frac{1}{1 + (\omega\tau)^2} - j \frac{(n_n + n_{res}) q_n^2 \tau}{m_n} \frac{\omega\tau}{1 + (\omega\tau)^2} - j \frac{n_s q_s^2}{\omega m_s} \end{aligned} \tag{3.17}$$

At microwave frequency, $\omega\tau << 1$, and Eq. (3.17) can be simplified to yield,

$$\sigma = \frac{(n_n + n_{res}) q_n^2 \tau}{m_n} - j \frac{n_s q_s^2}{\omega m_s}. \tag{3.18}$$

Hence, the real part and imaginary part of the microwave complex conductivity σ are

$$\sigma_1 = \frac{(n_n + n_{res}) q_n^2 \tau}{m_n}, \tag{3.19}$$

$$\sigma_2 = \frac{n_s q_s^2}{\omega m_s}. \tag{3.20}$$

The real part of σ represents the loss from the normal carriers and nonpairing residual normal carriers, whereas its imaginary part represents the kinetic energy of the superconductive carriers.

Substituting $\sigma = \sigma_1 - j\sigma_2$ into Eq. (3.12), one can obtain

$$Z_s = R_s + jX_s = \sqrt{\frac{j\omega\mu}{\sigma_1 - j\sigma_2}} = j\sqrt{\frac{\omega\mu}{\sigma_2}} \left(1 + j\frac{\sigma_1}{\sigma_2}\right)^{-1/2} \tag{3.21}$$

Because $\sigma_1 << \sigma_2$ except for the region very close to the critical temperature, a binomial expansion can be used to simplify the above formula, yielding

$$Z_s = R_s + jX_s \approx \sqrt{\frac{\omega\mu}{\sigma_2}}\left(\frac{\sigma_1}{2\sigma_2} + j\right), \tag{3.22}$$

$$R_s = \sqrt{\frac{\omega\mu}{\sigma_2}}\frac{\sigma_1}{2\sigma_2}, \tag{3.23}$$

$$X_s = \sqrt{\frac{\omega\mu}{\sigma_2}} \tag{3.24}$$

Substituting Eq. (3.19), Eq. (3.20) into Eq. (3.23), yields

$$R_s = \frac{\omega^2 \mu^{\frac{1}{2}} q_n^2 \tau}{2m_n} \frac{m_s^{\frac{3}{2}}}{q_s^3}\left(\frac{n_n + n_{res}}{n_s^{3/2}}\right). \tag{3.25}$$

One can expect that $m_s = m_n \equiv m_e$ and $q_n = q_s \equiv e$, which leads to the following expression,

$$\begin{aligned} R_s &= \frac{\omega^2 \mu^{\frac{1}{2}} q_n^2 \tau}{2m_n} \frac{m_s^{\frac{3}{2}}}{q_s^3}\left(\frac{n_n + n_{res}}{n_s^{3/2}}\right) \\ &= A\omega^2\tau \frac{1 - X_s(T)}{X_s^{3/2}(T)} \end{aligned} \tag{3.26}$$

where ,

$$A = \frac{1}{2}\sqrt{\frac{m_e \mu}{e^2 n_t}} \tag{3.27}$$

is defined. By using Eq. (3.4) — (3.11), we can derive,

$$R_s(T) = \frac{A\omega^2\tau}{(1 - X_{res})^{3/2}}\left[\frac{t^p}{(1 - t^p)^{3/2}} + \frac{X_{res}}{(1 - t^p)^{1/2}}\right] . \tag{3.28a}$$

Substitution of Eq. (3.20) into Eq. (3.24) yields

$$X_s = \omega\mu\lambda_L^*(T) \tag{3.28b}$$

where,

$$\lambda_L^*(T) = \sqrt{\frac{m_e}{\mu e^2 n_s}} \tag{3.29}$$

Applying Eq. (3.4) — (3.11), one can obtain

$$\lambda_L^*(T) = \lambda_L^*(0)\frac{1}{\sqrt{1-t^p}}, \tag{3.30}$$

where $\lambda_L^*(0) = \frac{1}{\sqrt{1-X_{res}}}\sqrt{\frac{m_e}{\mu e^2 n_t}}$. Note that the penetration depth at T = 0 K is increased from the London penetration depth $\lambda_L(0) = \sqrt{\frac{m_e}{\mu e^2 n_t}}$ due to the effect of the residual carriers.

The BCS theory[4] provides the quantum description of the superconducting state needed for a microscopic understanding of superconducting properties including the surface impedance. The conduction electron dynamics of bulk charge carriers are described by the following parameters:

1) mean free path l, density n_s, and Fermi velocity v_F;
2) the length $s = {}^{v_F}\!/_{\omega}$, as the distance traveled in one rf period, which is a crucial parameter of electrons in microwave field;
3) the London penetration depth $\lambda_L = \sqrt{m/\mu_0 n_s e^2}$;
4) the BCS or Pippard coherence length $\xi_F = {}^{\hbar v_F}\!/_{2\Delta}$ with the energy gap 2Δ. ξ_F is the extension of a Cooper pair shrinking by elastic and inelastic scattering like $\frac{1}{\xi_F(l)} = \frac{1}{\xi_F(\infty)} + \frac{1}{l}$.

The four lengths l, s, λ_L and ξ_F allow a unique description of the surface impedance Z in the normal and superconducting state at low magnetic fields for homogeneous, smooth, bulk material.

For the local limit $\xi << \lambda_L$, λ_L is a property of the condensation and its thermal excitations. At temperatures below $0.5T_c$, the change of the penetration depth $\Delta\lambda(T) = \lambda(T) - \lambda(0)$, and the microwave surface resistance of an s-wave BCS superconductor for a spherical Fermi surface are approximately expressed as follows.

$$\frac{\lambda(T)-\lambda(0)}{\lambda(0)}=\sqrt{\frac{\pi\Delta}{2k_BT}}e^{-\frac{\Delta}{k_BT}}, \tag{3.31}$$

$$R_s(\omega,T)=\frac{A\omega^2}{T}e^{-\frac{\Delta}{k_BT}}+R_{res}, \tag{3.32}$$

where k_B is the Boltzmann constant, A a constant, ω the angular frequency and $\Delta = \alpha k_B T_c$ the energy gap of the superconductor. In s-wave BCS theory for a spherical Fermi surface, $\alpha = 1.76$. The relations hold for $T < T_c/2$ and for frequencies well below $2\Delta/h$, where h is Planck's constant.

If the excitation gap vanishes on the Fermi surface or the pairing mechanism is of an unconventional type[15], the penetration depth and the surface resistance obey a power-law behavior: $\Delta\lambda(T)/\lambda(0) \approx B(T/T_c)^q$, $R_s(T) - R_{res} \approx C(T/T_c)^r$, where B is a constant of order unity and C is a constant with the dimension of resistance.

3.5 Principles of the surface impedance measurement methods

In our microwave surface impedance measurement, we adopted the demountable cavity method, which is suitable for our purpose as shown in section 5 of Chapter 1.

3.5.1 Q-value of TE_{01p} mode

In order to obtain a high Q-value, TE_{01p} mode should be selected. The surface currents excited by the TE_{01p} mode are exclusively circumferential and vanish at the joints, thus allowing for replacement of the endplate without disturbing the current and electromagnetic field distributions in the cavity. Since E and H in Eq. (7) of Appendix D vary sinusoidally with time, the maximum magnitude of E component, $E_{\varphi,\max}$, becomes:

$$E_{\varphi,\max} = \sqrt{2}\omega_r \mu_0 \left(\frac{a}{q_{01}^{'}}\right) \mathrm{H}_0 J_0^{'}\left(\frac{q_{01}^{'}}{a} r\right) \sin\left(\frac{p\pi}{l} z\right), \tag{3.33}$$

where $\omega_r = \frac{\pi}{\sqrt{\varepsilon_0 \mu_0}} \sqrt{\left(\frac{q_{01}^{'}}{\pi a}\right)^2 + \left(\frac{p}{l}\right)^2}$, the resonant frequency for TE_{01p} mode, a and l are the radius and the length of the cavity, $J_0^{'}(x)$ the derivative of the 0th order Bessel function with respect to x, $q_{01}^{'}$ the first root of $J_0^{'}(x)$, $\mu_0 = 4 \times 10^{-7}$ H/m, $\varepsilon_0 = 8.854 \times 10^{-12}$ F/m, $q_{01}^{'}$=3.832.

The total stored energy, U, is equal to the peak stored electrical energy (or the peak stored magnetic energy), which can be expressed as,

$$U = U_{E,\max} = \frac{1}{2}\varepsilon_0 \int_V E_{\varphi,\max}^2 dV$$
$$= \frac{\varepsilon\omega_r^2\mu_0^2 a^2 \mathrm{H}_0^2}{(\dot{q}_{01})^2} \int_0^a \int_0^l \int_0^{2\pi} \left[\dot{J}_0(\frac{\dot{q}_{01}}{a} r)\sin(\frac{p\pi}{l} z) \right]^2 r d\varphi dz dr \tag{3.34}$$

By using the identities, $\int x J_1^2(x)dx = \frac{x^2}{2}\left[J_1^2(x) - J_0(x)J_2(x)\right]$ and $\dot{J}_0(x) = -J_1(x)$, we obtain

$$U = \frac{\pi}{2}\mu_0 \mathrm{H}_0^2 (\frac{2\pi}{\lambda_r})^2 \frac{a^4 l}{(\dot{q}_{01})^2}\left[J_0(\dot{q}_{01})\right]^2, \tag{3.35}$$

where $\dot{q}_{01}$=3.832, and $J_0(\dot{q}_{01})$= -0.403.

First, the power dissipation, P_d, can be expressed as,

$$P_d = R_s \int_S K^2 dS = R_s \int_S H_t^2 dS, \tag{3.36}$$

where R_s is surface resistance, K is the surface current density, and H_t is the rms value of the tangential component of the magnetic field on the surface.

Then, the power loss for the cylindrical wall, P_{dc}, and the endplate, P_{dc}, can be calculated as

$$P_{dc} = \pi a l \mathrm{H}_0^2 R_s \left[J_0(\dot{q}_{01})\right]^2, \tag{3.37}$$

$$P_{dc} = \pi a^2 (\frac{p\pi a}{l\dot{q}_{01}})^2 \mathrm{H}_0^2 R_s \left[J_0(\dot{q}_{01})\right]^2. \tag{3.38}$$

Thus, the total loss for a cavity is

$$P_d = P_{dc} + 2P_{dc}$$
$$= \pi \mathrm{H}_0^2 R_s \left[J_0(\dot{q}_{01})\right]^2 \left[al + 2a^2 (\frac{p\pi a}{l\dot{q}_{01}})^2 \right]. \tag{3.39}$$

The basic definition of the unloaded quality factor Q_0 is expressed in terms of the stored energy U, angular frequency ω_r, and the power losses P_d:

$$Q_0 = \frac{\omega_r U}{P_d} = \frac{\omega_r U}{P_{dc} + 2P_{de}}. \tag{3.40}$$

Substituting the expressions of U and P_d into the quality factor definition yields,

$$\begin{aligned} Q_0 &= \frac{\omega_r U}{P_d} \\ &= \frac{\sqrt{\frac{\mu_0}{\varepsilon_0}}\left[(q_{01}')^2 + (\frac{p\pi a}{l})^2\right]^{3/2}}{2R_s\left[(q_{01}')^2 + \frac{2a}{l}(\frac{p\pi a}{l})^2\right]} \end{aligned} \tag{3.41}$$

3.5.2 Geometrical factor

The Q_0 given by Eq. (3.41) can also be expressed in terms of the geometrical factor Γ and the surface resistance R_s as,

$$Q_0 = \frac{\Gamma}{R_s}, \tag{3.42}$$

$$\Gamma = \frac{1}{2}\sqrt{\frac{\mu_0}{\varepsilon_0}}\frac{\left[(\dot{q_{01}})^2 + (\frac{p\pi a}{l})^2\right]^{3/2}}{(\dot{q_{01}})^2 + \frac{2a}{l}(\frac{p\pi a}{l})^2}. \tag{3.43}$$

The geometrical factor Γ depends only on the geometry and the mode of the cavity, and does not depend on the material properties.

By using the expression,

$$Q_0 = \frac{\omega_r U}{P_d} = \frac{\omega_r U}{P_{dc} + P_{de1} + P_{de2}} = \frac{1}{\frac{1}{Q_{0c}} + \frac{1}{Q_{0e1}} + \frac{1}{Q_{0e2}}}, \tag{3.44}$$

where P_{de1} and P_{de2} are the loss in the top and bottom endplates ($P_{de1} = P_{de2}$, if the top endplate and bottom endplate are made of the same material), the geometry factor for the cylindrical wall can be derived as,

$$\Gamma_c = \frac{1}{2}\sqrt{\frac{\mu_0}{\varepsilon_0}}\frac{1}{(\dot{q_{01}})^2}\left[(\dot{q_{01}})^2 + (\frac{p\pi a}{l})^2\right]^{3/2}. \tag{3.45a}$$

The geometry factor for the endplate, Γ_e, is

$$\Gamma_e = \frac{1}{2}\sqrt{\frac{\mu_0}{\varepsilon_0}}(\frac{l}{a})^3(\frac{1}{p\pi})^2\left[(\dot{q_{01}})^2 + (\frac{p\pi a}{l})^2\right]^{3/2}. \tag{3.45b}$$

Then, the combined geometry factor for one endplate and the cylindrical wall should be

$$\Gamma_r = \frac{1}{2}\sqrt{\frac{\mu_0}{\varepsilon_0}}\frac{\left[(\dot{q_{01}})^2 + (\frac{p\pi a}{l})^2\right]^{3/2}}{(\dot{q_{01}})^2 + \frac{a}{l}(\frac{p\pi a}{l})^2}. \tag{3.45c}$$

We introduce another geometrical factor k which is defined as

$$k = \int H_t^2 dS_m / \int H_t^2 dS_s \tag{3.46}$$

where S_m and S_s refer to the surface areas of the exposed metal and the HTS sample, respectively, and H_t is the component of the magnetic field parallel to the surface. The factor k is also given by the ratio of the factor Γ,

for the endplate,

$$k = \frac{\Gamma_e}{\Gamma} = 2 + \left(\frac{l}{a}\right)^3 \left(\frac{1}{p\pi}\right)^2 \left(\dot{q_{01}}\right)^2, \tag{3.47a}$$

and for the cylindrical wall,

$$k = \frac{\Gamma_c}{\Gamma} = 1 + \left(\frac{2a}{l}\right)\left(\frac{p\pi a}{l}\right)^2 \frac{1}{\left(\dot{q_{01}}\right)^2}. \tag{3.47b}$$

For our cavity with diameter (2a) of 33 mm and length of 19 mm, and operating in TE_{011} mode, Γ is 711.8 Ω and Γ_e is 3070 Ω. The k factor for the endplate is 4.313.

3.5.3 Maximum surface field

According to the expressions of field components as given in Appendix D, E_φ and H_z vary with $\sin(\frac{p\pi}{l}z)$, and H_r varies with $\cos(\frac{p\pi}{l}z)$ in the z-direction. Meanwhile, E_φ and H_r varies with $\left|J_0'(\frac{q_{01}'}{a}r)\right|$, and H_z varies with $\left|J_0'(\frac{q_{01}'}{a}r)\right|$ in the r-direction.

1). Maximum of H_r. In the z-direction $|H_r|$ takes the maxima at $z=\frac{nl}{p}$, where n is the integers from 0 through p. This means that the maxima occur at both the endplates. On the endplate $|H_r|$ becomes a maximum at r = 0.48a (or $\frac{q_{01}'}{a}r = 1.84$), where $\left|J_0'(\frac{q_{01}'}{a}r)\right|$ takes a maximum. Therefore the maximum surface field $|H_{r,\max}|$ at the endplate is given by

$$|H_{r,\max}|=\frac{\sqrt{2}p\pi a}{lq_{01}'}\mathrm{H}_0\left|J_0'(1.84)\right|, \tag{3.48}$$

from which, one gets the expression of H_0:

$$\mathrm{H}_0=\frac{lq_{01}'|H_{r,\max}|}{\sqrt{2}p\pi a\left|J_0'(1.84)\right|}. \tag{3.49}$$

Substituting Eq. (3.39) into the expression of U (Eq. 3.35) and using $Q_0=\frac{\omega_r U}{P_d}$ yields,

$$|H_{r,\max}|=0.325(\frac{\varepsilon_0}{\mu_0})^{1/4}(\frac{p}{a})(\frac{\lambda_r}{l})^{3/2}\sqrt{P_dQ_0}. \tag{3.50}$$

2). Maximum of H_z. From Eq. (7) in Appendix D, H_z becomes the maxima at r = 0 and $z = \frac{nl}{2p}$ (n is the integers from 1 through p), which is given by

$$\left|H_{z,\max}\right| = \sqrt{2}\mathrm{H}_0 J_0(0) \ . \tag{3.51}$$

In comparison to Eq. (3.48), we can obtain,

$$\frac{\left|H_{z,\max}\right|}{\left|H_{r,\max}\right|} = \frac{l\dot{q_{01}} J_0(0)}{p\pi a\left|\dot{J_0}(1.84)\right|} \ . \tag{3.52}$$

With $\dot{q_{01}}$ = 3.832, $J_0(0)$ = 1.0, and $\left|\dot{J_{01}}(1.84)\right|$ = 0.582, Eq. (3.52) yields

$$\left|H_{z,\max}\right| = 0.681(\frac{\varepsilon_0}{\mu_0})^{1/4}(\frac{l}{a^2})(\frac{\lambda_r}{l})^{3/2}\sqrt{P_d Q_0} \ . \tag{3.53}$$

This maximum field occurs at the center of the cavity along the z direction. At the cavity wall, maximum value H_z decreases by $\left|J_0(\dot{q_{01}})/J_0(0)\right| = 0.403$ as,

$$\left|H_{zw,\max}\right| = 0.403\left|H_{z,\max}\right|, \tag{3.54}$$

or

$$\left|H_{zw,\max}\right| = 0.274(\frac{\varepsilon_0}{\mu_0})^{1/4}(\frac{l}{a^2})(\frac{\lambda_r}{l})^{3/2}\sqrt{P_d Q_0} \quad \text{(A/m)} \ . \tag{3.55}$$

3). Maximum of E_φ. At $z = \frac{nl}{2p}$, and $\dot{J_0}(\frac{\dot{q_{01}}}{a}r)\Big|_{\frac{\dot{q_{01}}}{a}r=1.84}$, E_φ given by Eq. (7) in Appendix D becomes the maximum, yielding the following expression,

$$\left|E_{\varphi,\max}\right| = \sqrt{2}\omega_r\mu\frac{a}{\dot{q_{01}}}\mathrm{H}_0\left|\dot{J_0}(1.84)\right| \ . \tag{3.56}$$

In comparison with Eq. (3.48), we can obtain,

$$\frac{\left|E_{\varphi,\max}\right|}{\left|H_{r,\max}\right|} = \frac{2}{\lambda_r}\sqrt{\frac{\mu}{\varepsilon}}\frac{l}{p} \quad . \tag{3.57}$$

Therefore, the maximum of E_φ can be expressed as

$$\left|E_{\varphi,\max}\right| = 0.650\left(\frac{\mu_0}{\varepsilon_0}\right)^{1/4}\left(\frac{1}{a}\right)\left(\frac{\lambda_r}{l}\right)^{1/2}\sqrt{P_d Q_0} \quad . \tag{3.58}$$

From comparison between Eqs. (3.50) and (3.55), we notice that $\left|H_{r,\max}\right|$ is larger or smaller than $\left|H_{zw,\max}\right|$, depending on the mode number p and the cavity geometry (a and l). For our cavity (P = 1, a = 16.5 mm, l = 19 mm), $\left|H_{r,\max}\right|$ is only 3% larger than $\left|H_{zw,\max}\right|$.

3.5.4 R_s measurement method

The surface resistance of HTS films is obtained through Q-value of a cavity[9,10,11,12]. We find the resonant peak and half-power points from the S_{21} coefficient using a network analyzer, which gives the loaded quality factor Q_L. From the S_{11} and S_{22} coefficients of the two coupling ports, the coupling factors β_1 and β_2 are calculated. Then the unloaded quality factor $Q_{0,\mathrm{Cu}}(T)$ of the copper host cavity is measured as a function of temperature T, $Q_{0,Cu}(T) = Q_{L,Cu}(T)[1+\beta_1(T)+\beta_2(T)]$. The surface resistance of copper $R_{\mathrm{s,Cu}}(T)$ is calculated by Eq. (3.42) with a given geometrical factor, $R_{s,Cu}(T) = \dfrac{\Gamma}{Q_{0,Cu}(T)}$, where Γ is 711.8 Ω for our cavity with 2a = 33 mm, l = 19 mm and p = 1. Then, the top endplate is replaced by the one covered with a superconducting film, and the unloaded quality factor $Q_{0,\mathrm{Cu+hTc}}(T)$ is measured. In terms of these unloaded quality factors and the geometrical factors Γ as defined previously, the surface resistance $R_{\mathrm{s,hTc}}(T)$ of the high-T_c films at temperature T is calculated by, $\dfrac{R_{s,hTc}(T)}{R_{s,Cu}(T)} = \dfrac{\Gamma_e}{\Gamma}\left(\dfrac{Q_{0,Cu}(T)}{Q_{0,Cu+hTc}} - \dfrac{\Gamma}{\Gamma_r}\right)$, where Γ_e, Γ_r and Γ are the geometrical factors of the endplate, one endplate + cylinder and the whole cavity, respectively. Equation (3.59) is also expressed using the k factor of the endplate as,

$$\frac{R_{\mathrm{s,hTc}}(T)}{R_{\mathrm{s,Cu}}(T)} = k\left(\frac{Q_{0,\mathrm{Cu}}(T)}{Q_{0,\mathrm{Cu+hTc}}(T)} - 1\right) + 1 \quad , \tag{3.59}$$

where k = 4.313 for the cavity we used.

3.5.5 Error in R_s measurements

It is necessary to discuss the error[10] in R_s measurements with host cavity method(or, endplate replacement method), in which part of the host cavity is replaced by a superconducting material. As the surface resistance of the superconducting material becomes much smaller than that of the host cavity material, the relative error increases because of the difficulty in separating the sample loss from the dominant loss of copper. Differentiation of $R_{s,hTc}(T)$ in Eq. (3.59) with respect to $Q_{0,Cu+hTc}(T)$ and additional operations lead to

$$\frac{\Delta R_{s,hTc} / R_{s,hTc}}{\Delta Q_{0,Cu+hTc} / Q_{0,Cu+hTc}} = -\frac{(R_{s,hTc} / R_{s,Cu}) + (k-1)}{R_{s,hTc} / R_{s,Cu}} . \tag{3.60}$$

Due to Eq. (3.60), the ratio of relative error, $(\Delta R_{s,hTc} / R_{s,hTc}) / (\Delta Q_{0,Cu+hTc} / Q_{0,Cu+hTc})$, increases with decreasing $R_{s,hTc} / R_{s,Cu}$, as shown in Fig. 3.1 for the case of k = 4.313. A similar expression can be derived for $(\Delta R_{s,hTc} / R_{s,hTc}) / (\Delta Q_{0,Cu} / Q_{0,Cu})$.

Since the two separate Q_0 measurements are made for $Q_{0,Cu}$ and $Q_{0,Cu+hTc}$, $R_{s,hTc}$ data obtained include systematic errors as well as fluctuation errors. Equation (3.60) and Fig. 3.1 show that the systematic errors increase with decreasing temperature. The systematic errors can therefore be compensated if we know an accurate value of $R_{s,hTc}$ at a low temperature. Then, if we use a niobium host cavity, we can measure $R_{s,hTc}$ accurately at temperatures below 9 K, and can use it to calibrate $R_{s,hTc}$ measured by the copper host cavity.

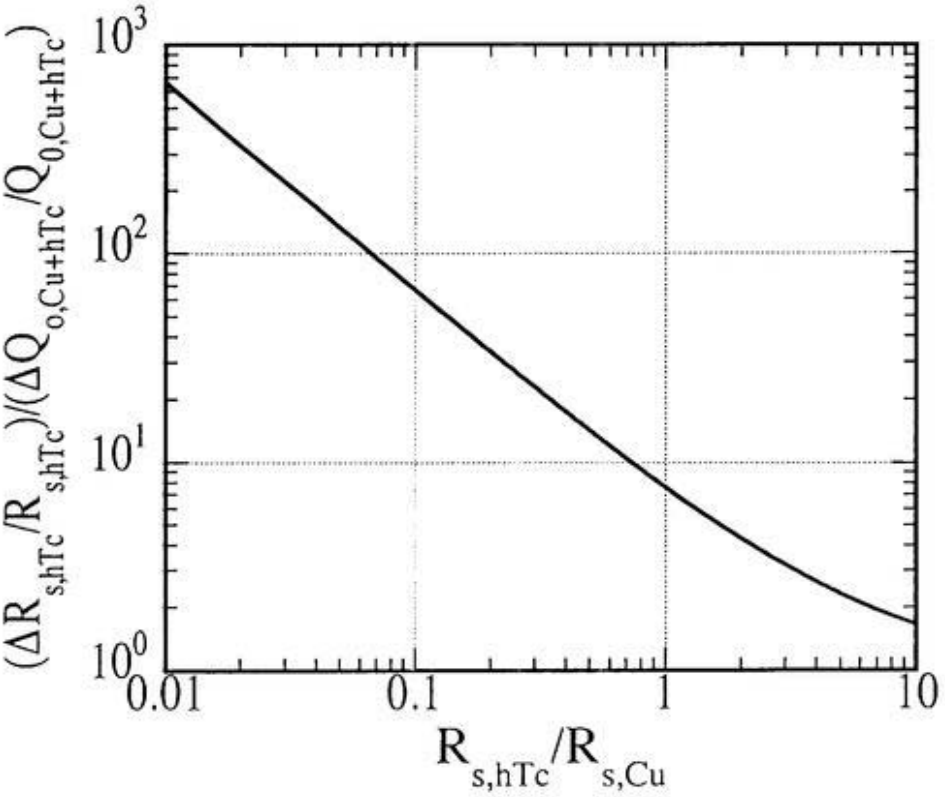

Fig. 3.1. The ratio of relative error, $(\Delta R_{s,hTc} / R_{s,hTc})/(\Delta Q_{0,Cu+hTc} / Q_{0,Cu+hTc})$, as a function of $R_{s,hTc} / R_{s,Cu}$ for the case of k = 4.313.

3.5.6 Relationship between Penetration depth change and frequency shift

During the measurement of the cavity Q-value as a temperature function, the resonant frequency $f(T)$ is determined with high precision. The cause of the total frequency shift of the cavity with temperature change would be attributable to changes of such as the dimension due to the thermal expansion, the microwave surface impedance, the deformation of the cavity assembly due to nonuniform stress, and so on[13]. At the temperatures close to the critical temperature, a significant change in the resonant frequency can be observed due to the change in penetration depth. The relationship between the frequency shift Δf and the penetration depth change $\Delta\lambda$ can be calculated by considering perturbation of the cavity boundaries. With perturbation theory[14], we have

$$\frac{\Delta f}{f} = -\frac{\int_{\Delta V}(\mu|H|^2 - \varepsilon|E|^2)dV}{4U}. \tag{3.62}$$

For the endplate replacement method, the penetration depth change occurred at the high-T_c film endplate. At the endplate, only the magnetic field H_r exists according to the field distribution as described in Appendix D. Substituting the expression of field H_r of Eq. (7) in Appendix D into the numerator of Eq. (3.62) yields:

$$\begin{aligned}\int_{\Delta V}\mu|H|^2 dV &= 2\mu\Delta\lambda\int_s H_r^2 dS \\ &= 2\pi a^2\mu\left(\frac{p\pi a}{lq_{01}'}\right)^2 H_0^2\left\{J_0(q_{01}')\right\}^2\Delta\lambda\end{aligned} \tag{3.63}$$

With the total stored energy U given in Eq. (3.35), the relationship between the penetration depth change $\Delta\lambda$ at one endplate and the resonance frequency shift Δf of the cavity can be obtained as,

$$\begin{aligned}\frac{\Delta f}{f} &= -\frac{\int_{\Delta V}(\mu|H|^2 - \varepsilon|E|^2)dV}{4U} = -\frac{\int_{\Delta V}\mu|H|^2 dV}{4U} \\ &= -\frac{2\mu\Delta\lambda\int_S H_r^2 dS}{4U} \\ &= -\frac{\omega_r\mu\Delta\lambda}{2\Gamma_e}\end{aligned} \tag{3.64}$$

References

(References for Chapter 3, Theory relevant to surface impedance measurements)

1. Vladimir Z. Kresin and Stuart A. Wolf, *Fundamentals of Superconductivity*, Plenum Press, New York and London, p.3 (1990).
2. A. C. Rose-Innes and E. H. Rhoderick, *Introduction to Superconductivity*, Pergamon Press Ltd. (1978).
3. G. Bednorz and K. A. Müller, Z. Phys. B. **64**, 189 (1986).
4. J. Bardeen, L. N. Cooper, J. R. Schrieffer, Phys. Rev. **108**, 1175 (1957).
5. Z.-Y. Shen, *High-Temperature Superconducting Microwave Circuits*, p.25 (Artech House Boston.London 1994).
6. G. Müller, N. Klein, A. Brust, H. Chaloupka, M. Hein, S. Orbach, H. Piel, and D. Reschke, J. of Supercond. **3**, 235 (1990).
7. Y. Kobayashi, and T. Imai, IEICE Transactions, **74**, 1986 (1991).
8. J. R. Waldram, P. Theopistou, A. Porch, and H.-M. Cheah, Phys. Rev. B **55**, 3222 (1997).
9. Jian-Fei Liu, K. Asano, E. Ezura, S. Inagaki, S. Isagawa, H. Nakanishi, M. Fukutomi, K. Komori, and M. Saito: "*Precise Measurements of Microwave Surface Impedance of c-axis oriented $YBa_2Cu_3O_{7-x}$ Films Fabricated on a Copper Substrate*" submitted to J. Appl. Phys.
10. E. Ezura, K. Asano, H. Hayano, K. Hosoyama, S. Inagaki, S. Isagawa, M. Kabasawa, Y. Kojima, S. Kosuge, S. Mitsunobu, T. Momose, K. Nakada, H.

Nakanishi, Y. Shimbo, T. Shishido, K. Tachikawa, T. Takahashi, and K. Yoshihara, Jpn. J. Appl. Phys. **32**, 3435 (1993).

11. Jian-Fei Liu, K. Asano, E. Ezura, M. Fukutomi, S. Inagaki, S. Isagawa, K. Komori, H. Nakanishi, M. Tosa, and K. Yoshihara, Proc. 1995 Particle Accelerator Conf., Dallas, 1995, p. 1652 (1995).
12. S. Inagaki, K. Asano, E. Ezura, S. Haseyama, S. Isagawa, J.-F. Liu, H. Nakanishi, and S. Yoshizawa, Jpn. J. Appl. Phys. **36**, 3478 (1997).
13. S. Inagaki, E. Ezura, Jian-Fei Liu, and H. Nakanishi, J. Appl. Phys. **82**, 5401 (1997).
14. John C. Slater, *Microwave Electronics*, D. Van Nostrand Company, Ltd. (1950).
15. A. J. Berlinsky, C. Kallin, G. Rose, and A-C. Shi, Phys. Rev. B **48**, 4074 (1993).

4. Experimental setups

We adopted the host cavity method or endplate replacement method[1-4] to measure the surface impedance of the YBCO films. Two cavities, i.e. copper host cavity and niobium host cavity were prepared. The systems were established to measure the temperature dependence of the surface impedance, and the rf field dependence of the surface resistance.

4.1 Setup for a temperature dependence measurement

As shown in Fig. 4.1, the cavity was composed of two components. One was machined out of a block of material, the inner surface of which was in cylindrical shape with flat bottom surface. The other is a top endplate. We call the former as a "host cavity" and the latter simply as an "endplate". The endplate was replaceable with that of the high-T_c films fabricated as mentioned above. The diameter and the length of the cavity were 33 mm and 19 mm, respectively. The endplates were circular disks of 36 mm diameter and 3 mm thickness. The resonant frequency of the TE_{011} mode was about 13.6 GHz and k for the endplate was 4.313, where k is a geometrical factor defined by Eq. (3.46).

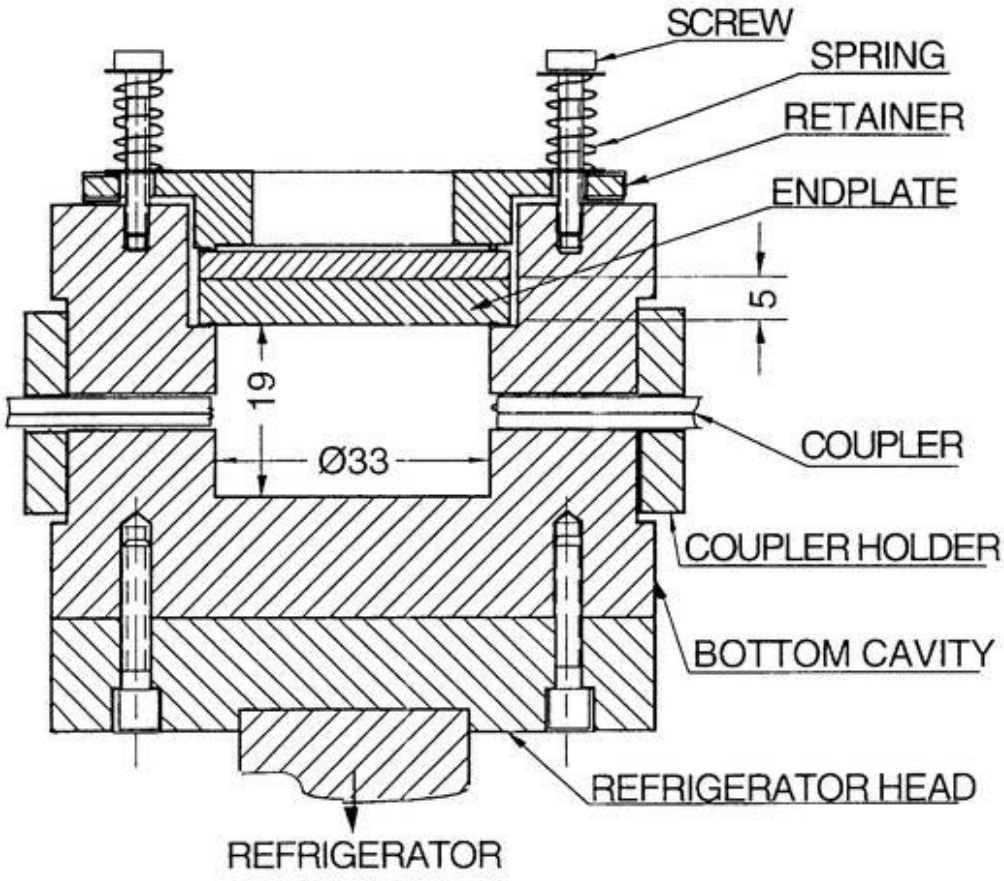

Figure 4.1: Cavity assembly. Every component that contacts the main cavity is made of copper to avoid stress due to a difference in thermal expansion.

The experimental setup for high temperature region is shown in Fig. 4.2. Here the temperature of the cavity was controllable from 11 K to 300 K by a closed-cycle refrigerator and a 50 W heater with an autotuning temperature controller. In the figure, the host cavity is indicated by a right-up hatch and the endplate by a left-up hatch. Both parts were made of copper. The host cavity was loosely fixed to the refrigerator head with copper screws. The endplate was fixed to the host cavity with springs with a force of about 1.58 kgf at room temperature. At the middle of the host cavity wall, two holes

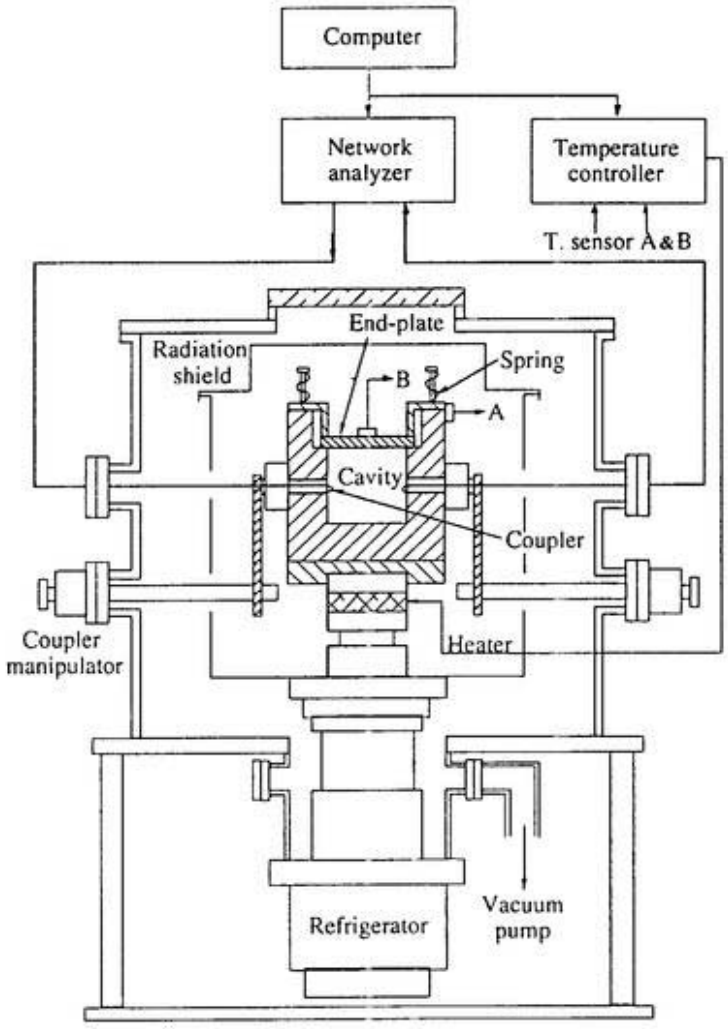

Fig. 4.2 Experimental setup for measuring the temperature dependence of the surface resistance

of 3.6 mm in diameter were drilled. These were for rf coupling loops made of 50 Ω coaxial lines (UT141). Each coupling constant could be adjusted from outside the vacuum vessel by a manipulator. The whole cavity assembly was evacuated with a 300 l/s turbo molecular pump. The cavity was cooled down after it was evacuated below 10^{-3} Pa. A radiation-shield was put between the vacuum vessel and the cavity assembly. Furthermore, superinsulator films were used to reduce heat intrusion.

4.2 Experimental set-up with niobium host cavity

The experimental setup[4] for measurements in a low temperature region is shown in Fig. 4.3. Here the host cavity was made of niobium indicated with a right-up hatch. The endplate was made of either niobium or copper covered with high-T_c film indicated with a left- up hatch. The measured temperature region was from 4.2 K to about 9.2 K. The host cavity in a brass holder assembly was vacuum-sealed with indium lines of 0.5

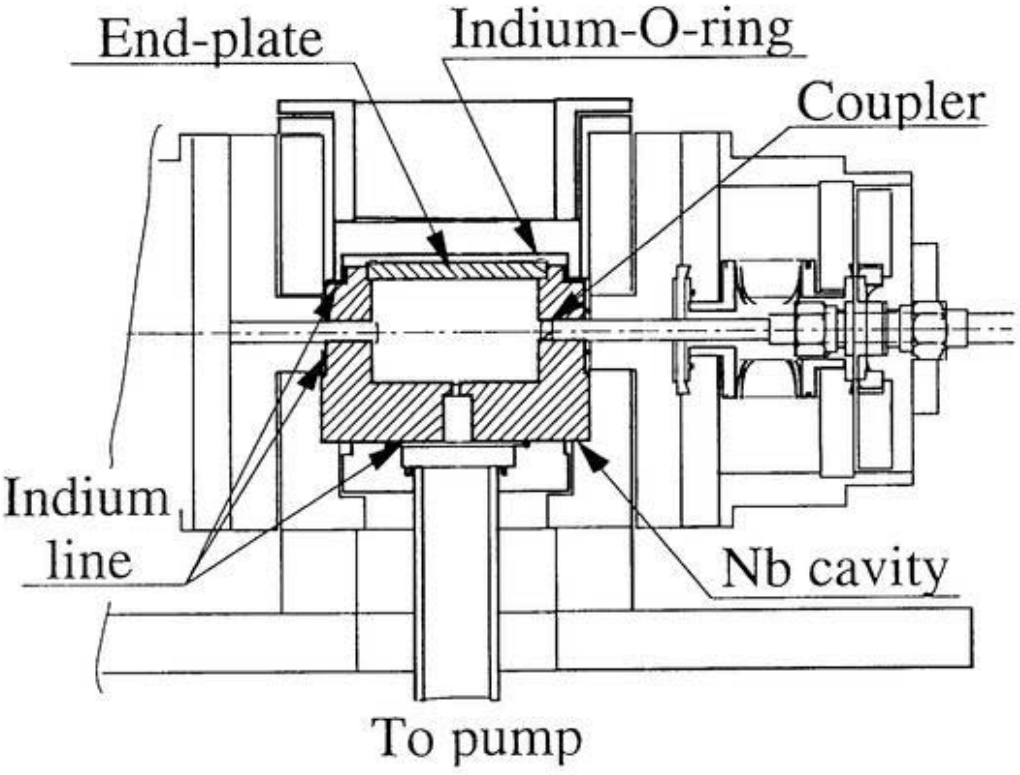

Fig. 4.3. Experimental set-up with niobium host cavity for low temperature region

mm in diameter, and evacuated through a hole at the bottom center. The endplate was pressed to the host cavity through indium lines with a vacuum endcap. Two rf coupling loops at the middle of the cylinder were made from 50 Ω semi-rigid coaxial cable (UT85). The coupling constant could be varied from outside the cryostat through wormgears. Since the cavity was evacuated, a bellow assembly was used for the coupler movement about 10 mm. The assembly was first soaked in liquid helium within a cryostat, as shown in Fig. 4.4, and warmed up through intruding heat. During the measurement, the quality factor changed about three orders from superconducting to normal state.

For both of the above setups, we found the resonant frequency, loaded quality factor and coupling constants[1-4] with a constant temperature step. Replacing the copper or niobium endplate with an endplate covered by a high-T_c film, and from the measured unloaded quality factor, we can find the microwave surface resistance $R_{s,hTc}(T)$ of the high-T_c film by Eq.(3.59).

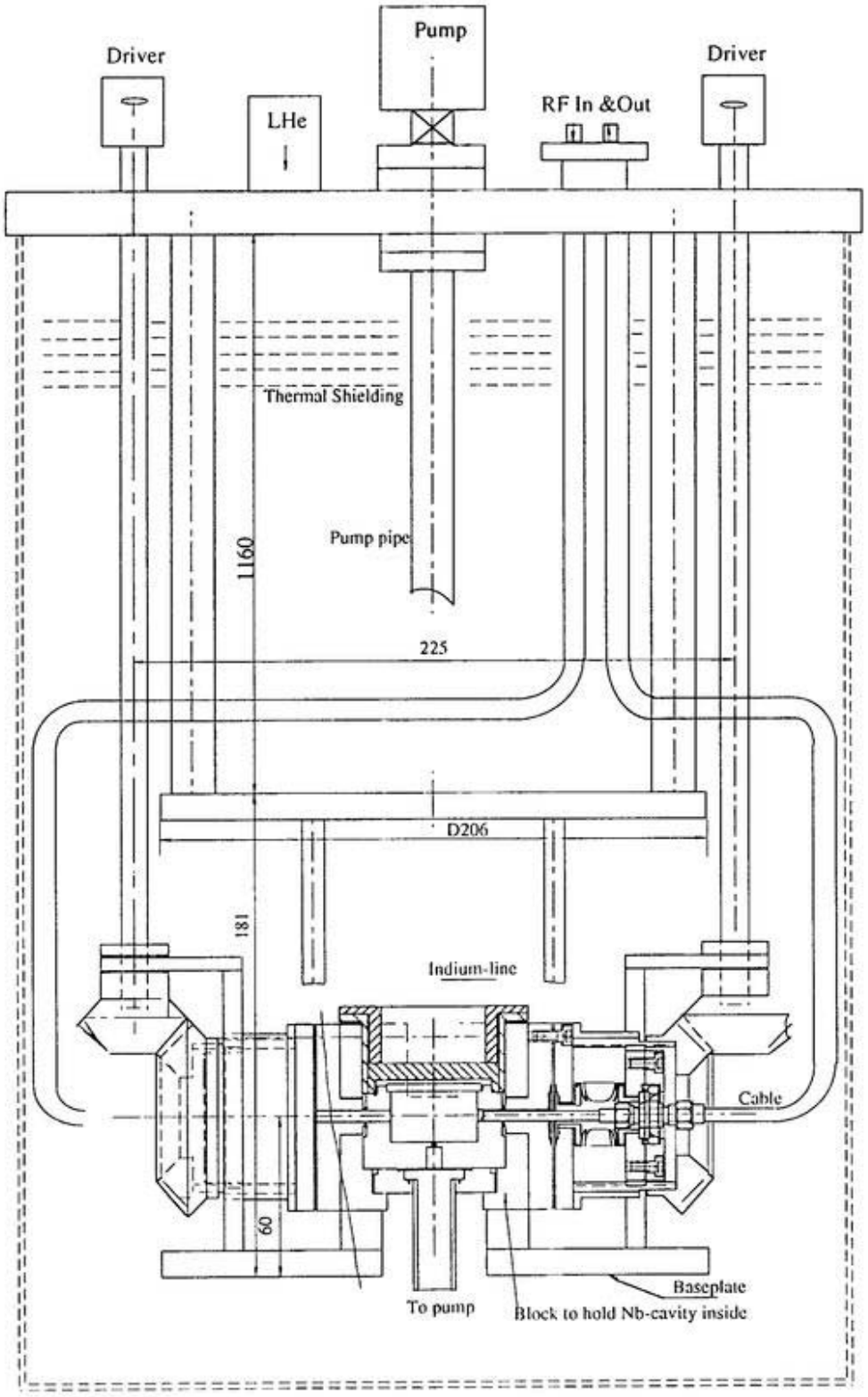

Fig. 4.4 Schematic drawing of experimental setup with niobium host cavity in a cryostat.

References

1. E. Ezura, K. Asano, H. Hayano, K. Hosoyama, S. Inagaki, S. Isagawa, M. Kabasawa, Y. Kojima, S. Kosuge, S. Mitsunobu, T. Momose, K. Nakada, H. Nakanishi, Y. Shimbo, T. Shishido, K. Tachikawa, T. Takahashi, and K. Yoshihara, Jpn. J. Appl. Phys. **32**, 3435 (1993).
2. Jian-Fei Liu, K. Asano, E. Ezura, M. Fukutomi, S. Inagaki, S. Isagawa, K. Komori, H. Nakanishi, M. Tosa, and K. Yoshihara, Proc. 1995 Particle Accelerator Conf., Dallas, 1995, p. 1652 (1995).
3. S. Inagaki, E. Ezura, Jian-Fei Liu, and H. Nakanishi, J. Appl. Phys. **82**, 5401 (1997).
4. Jian-Fei Liu, K. Asano, E. Ezura, S. Inagaki, S. Isagawa, H. Nakanishi, M. Fukutomi, K. Komori, and M. Saito: "*Precise Measurements of Microwave Surface Impedance of c-axis oriented $YBa_2Cu_3O_{7-x}$ Films Fabricated on a Copper Substrate*" submitted to J. Appl. Phys.
5. Jian-Fei Liu, K. Asano, E. Ezura, S. Inagaki, S. Isagawa, H. Nakanishi, M. Fukutomi, K. Komori, and M. Saito, Appl. Phys. Lett. 73, 3450 (1998).
6. Jian-Fei Liu, K. Asano, E. Ezura, M. Fukutomi, S. Inagaki, K. Komori, H. Nakanishi, and M. Saito, Proc. 1998 1st Asian Part. Accel. Conf., Tsukuba, Japan (1998).

5. Precise measurement of surface impedance

This chapter deals with the measurements of R_s and λ of c-axis oriented YBCO films deposited on copper substrates. For R_s measurements, we used both Cu and Nb host cavities, which gave an improved accuracy than that obtained with one host cavity. The data calibration procedure is described and measured results of R_s, λ and σ are discussed.

5.1 Microwave surface resistance

The temperature of the copper cavity was controlled from 11 K to 300 K by a closed-cycle refrigerator and a 50 W heater, as shown in Fig. 4.2. The niobium cavity was immersed in liquid-helium in a cryostat as shown in Fig. 4.4, and warmed up gradually by intruding heat from 4.2 K to about 8 K. This upper temperature was limited by the decreasing coupling factors with increasing temperature, since the quality factor decreased by more than two orders in changing from superconducting to normal state.

By adopting niobium and copper as the host cavity material, two groups of data points were obtained: one below 8 K obtained by the niobium cavity (denoted with

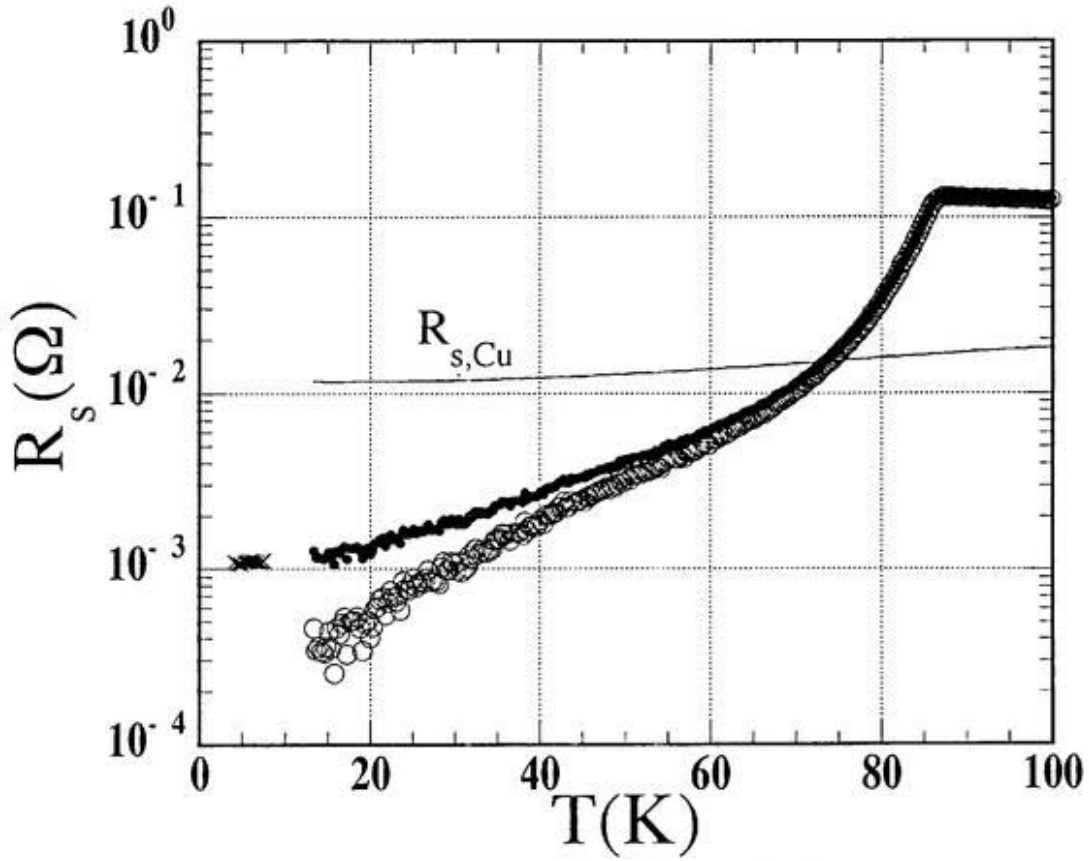

Fig.5.1 The temperature dependence of the surface resistance for YBCO film EC232, open circles obtained by copper-host cavity, crosses below 8 K from niobium cavity, and dots above 10 K obtained by fitting.

crosses in Fig. 5.1) and the other above 11 K obtained by the copper cavity (denoted with open circles). We know that the data obtained by the niobium cavity is reliable since the surface resistance of niobium is much lower than that of the YBCO film. However, the data obtained by the copper cavity include large errors at low temperatures where the surface resistance of the YBCO film becomes about one order lower than that of copper (See Fig. 3.1).

We denote $R_{s,hTc}(T)$ as that measured with the copper host cavity by $R_{s,\ hTc(Cu)}(T)$ and that measured with niobium host cavity by $R_{s,\ hTc(Nb)}(T)$. Here, the raw $R_{s,\ hTc(Cu)}(T)$

values are not, in general, smoothly tied up with $R_{s,\,hTc(Nb)}(T)$ as shown in Fig. 5.1. If it were possible to measure $R_{s,\,hTc(Cu)}(T)$ down to 8 K, the calibration could be carried out easily, in principle, by equating $R_{s,\,hTc(Cu)}(T) = R_{s,hTc(Nb)}(T)$. Since this was not the case in the present experiment, we followed an iteration procedure as decribed in Appendix F. After calibration for the mentioned models given in Chapter 3 and by comparing the correlation coefficients, we can discuss a possible conduction mechanism. Let the correlation coefficient obtained to follow model A be denoted by R_A and that obtained to follow model B by R_B. If $R_A < R_B \leq 1$, we conclude that model B explains the experiment better than model A. In the following, "calibration" is meant for systematic processing of raw data, and "fitting" is meant for finding regression coefficients for the calibrated data.

The dots in Fig. 5.1 show the calibrated $R_{s,\,hTc(Cu)}(T)$, which was to follow the modified two-fluid model with $p = 2$ below $T_c/2$. Here, T_c was defined as the temperature at the maximum $dR_{s,hTc}/dT$ and 87.5 K for the present samples. The calibration constants (in Appendix F) were $c_1 = 1.0192$, $c_2 = 1.0031$ and $R_{mtf} = 0.997$, where R_{mtf} is the correlation coefficient for the modified two-fluid model. This leads to $E = 3.76 \times 10^{-3}\ \Omega$, *i.e.*, $\tau n_s \lambda^3(0) = 2.31 \times 10^{-5}$ s, and $x_{ncs} = 0.202$. Another modified two-fluid model calibration including with $p = 4$ was poorer than that with $p = 2$.

If $R_{s,\,hTc(Cu)}(T)$ was calibrated to follow the BCS model below $T_c/2$, the calibration constants were $c_1 = 1.0192$, $c_2 = 1.0007$ and $R_{BCS} = 0.993$, where R_{BCS} is the correlation coefficient for the BCS model. (The difference between the calibration constants for the modified two-fluid model and those for BCS model is, therefore, only 0.2%.) We

obtained R_{res} = 1.11 × 10^{-3} Ω, A = 9.36 × 10^{-21} ΩKs^2 and Δ = 11.4 meV (α = 1.51). This energy gap is almost the same as that predicted by the BCS model (only 14% smaller).

In the r = 2 calibration below T_c/2, the calibration constants c_1 = 1.0192 and c_2 = 1.0040 and R_{Tsg} = 0.993, where R_{Tsq} is the correlation coefficient for the T^2 fitting. We obtained R_{res} = 1.03 × 10^{-3} Ω and C = 8.18 × 10^{-3} Ω. For the present sample, an r =1

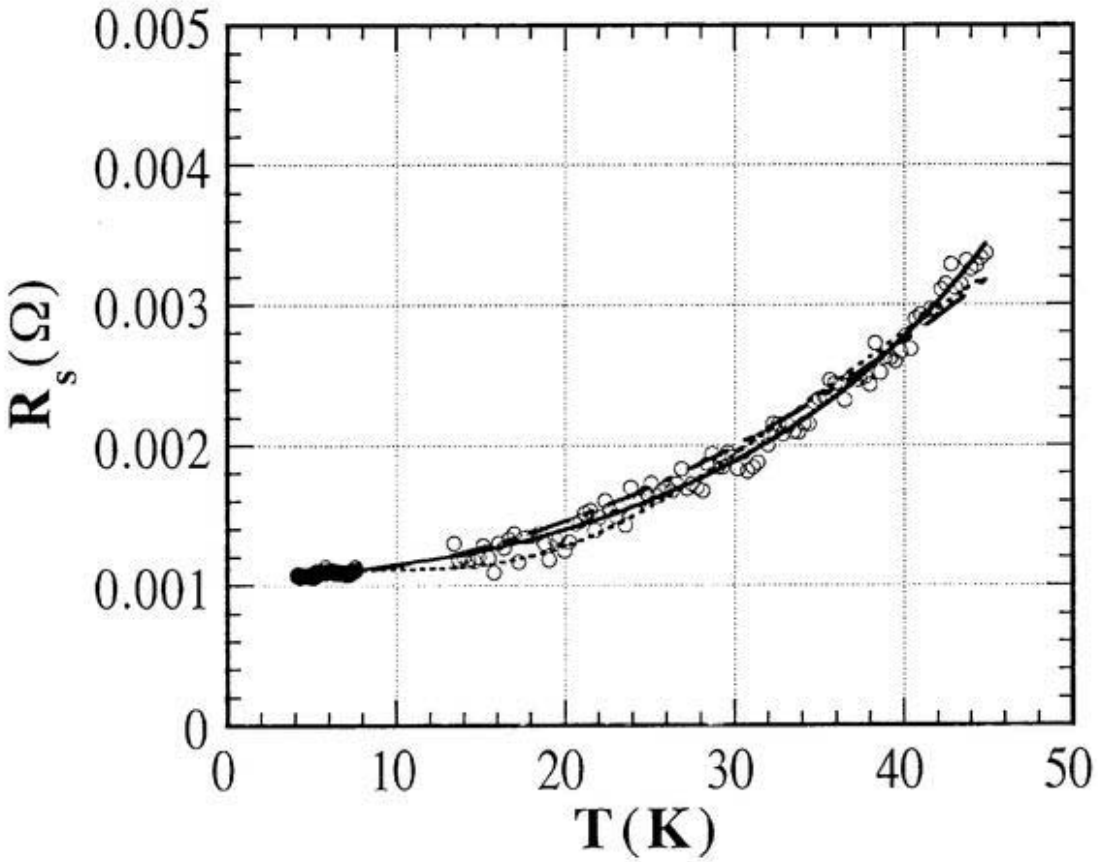

Fig.5.2 Microwave surface resistance ($R_{s,hTc}$) for a temperature region until 45 K. The solid line, dotted line and dot-and-dash line show the fittings by the modified two-fluid model, BCS and T^2, respectively. The data points were calibrated by the modified two-fluid model.

calibration was applied only in a limited temperature region, and no such broad maximum around 38 K, as reported by Bonn et al.[3], was observed.

A closer look at the data deviations from the fitted lines shows that among these calibrations the modified two-fluid model was most competent as is consistent with the fact that R_{mtf} was slightly larger than R_{BCS} and R_{Tsq}. In Fig 5.2, the three fittings, the modified two-fluid model, the BCS model and the T^2 model, are indicated with the solid line, dotted line and dot-and-dash line, respectively. The data points with open circles were calibrated to follow the modified two-fluid model.

5.2 Penetration depth

As described in Chapter 3, due to the change in penetration depth, a significant change in the resonant frequency can be observed at the temperatures close to the critical temperature, as shown in Fig. 5.3. The thin line in the figure is for eye guide, which clearly shows that the frequency (denoted with dots) increased sharply when T decreased below T_c. By comparing the dot line with the frequency change obtained from

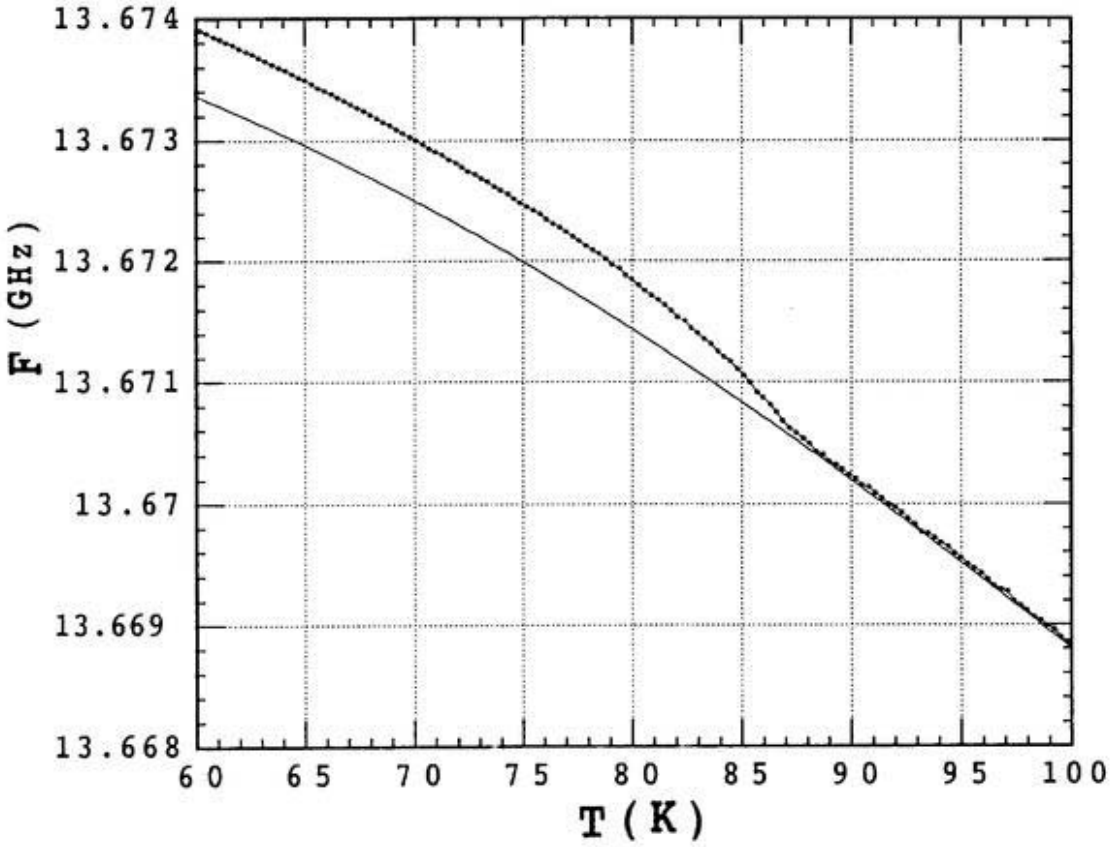

Fig. 5.3 The resonant frequency changes with temperature increasing (the thin line provided as a guide to the eye).

full copper host cavity(not shown in figure), the frequency shift Δf due to the penetration depth change was obtained.

With Eq. (3.64) and the geometrical factor for the endplate (i.e. $\Gamma_e = 3070.3\ \Omega$ as given in Eq. (3.45b)), the penetration depth change $\Delta\lambda$ as a function of temperature T was calculated as shown in Fig. 5.4 with open circles. The solid line is the fitting below $T_c/2$ by the modified two-fluid model in Eq. (3.30) with $p = 2$ and $\lambda^*(0) = 0.693\ \mu m$

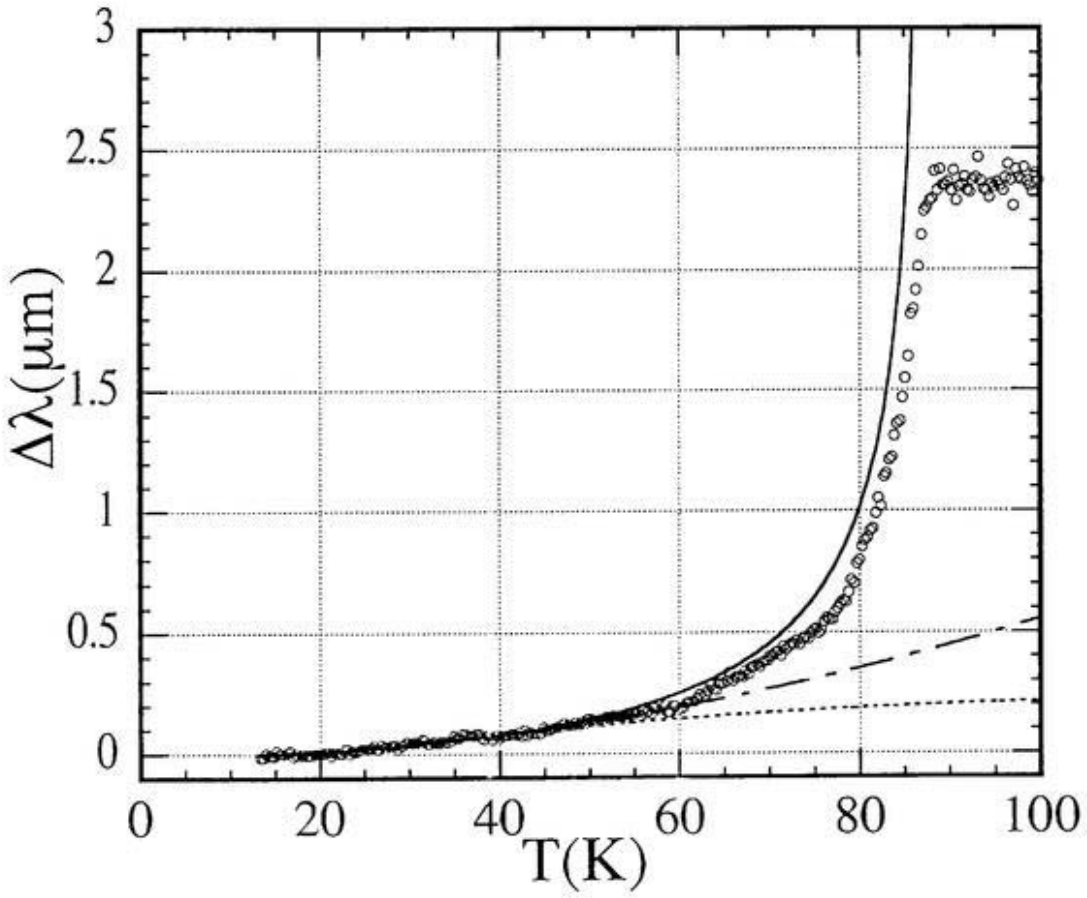

Fig. 5.4. Penetration depth $\Delta\lambda$ as a function of temperature. The solid line is the fitting below $T_c/2$ by the modified two-fluid model with $p = 2$. The dotted line is the BCS fitting below $T_c/2$.

(*i.e.*, $\lambda_{tfm}(0) = 0.619$ μm) with $R = 0.955$. The fitting with $p = 4$ in the same equation was not satisfactory. In the figure, the dotted line is the BCS fitting with $\lambda_{BCS}(0) = 0.387$ μm and $\Delta = 7.25$ meV with $R = 0.972$. This energy gap is about 64% of $\Delta = 11.4$ meV obtained from the microwave surface resistance described above. The dot-and-dash line is the T^2 fitting with $\lambda_{sq}(0)B = 0.437$ μm with $R = 0.963$. The

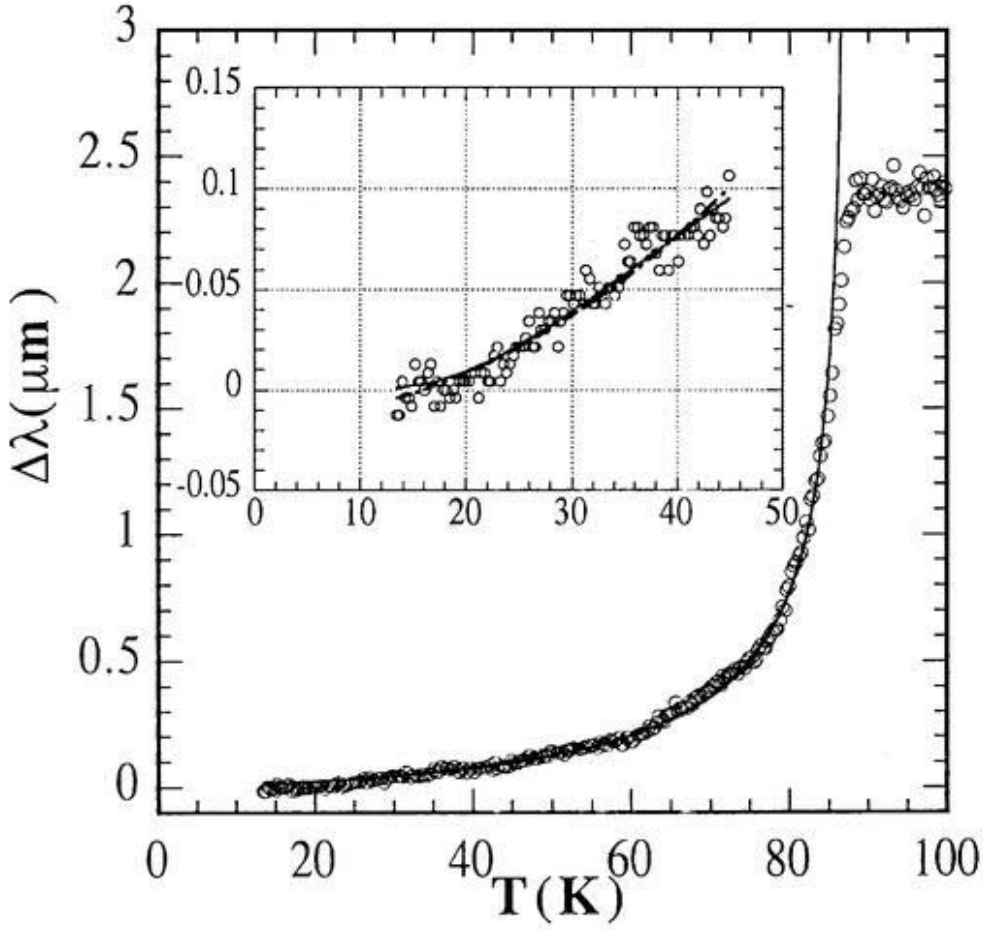

Fig. 5.5. Penetration Depth Δλ as afunction of temperature. The solid line is the fitting below 85 K by the modified two-fluid model with $p = 2$.

obtained penetration depth $\lambda_{tfm}(0) = 0.619$ μm for $p = 2$ was larger than the typical value around 0.15—0.3 μm for single crystals or epitaxial films reported from other institutions[2,4-6].

The solid line in Fig. 5.5 shows another modified two-fluid model fitting with $p = 2$; this time the fitting was made in the temperature region below 85 K and $\lambda^*(0) = 0.521$ μm (i.e., $\lambda_{tfm}(0) = 0.465$ μm) with $R = 0.995$. It is seen from the figure that the modified two-fluid model with $p = 2$ fits very well to the measurement over a wide temperature range. Until about 60 K, the square-temperature law was fit to the measured $\Delta\lambda(T)$ better than the linear-temperature law was. Two kinks were observed around 60 K and 77 K, which gave two peaks in the real part of conductivity as shown below.

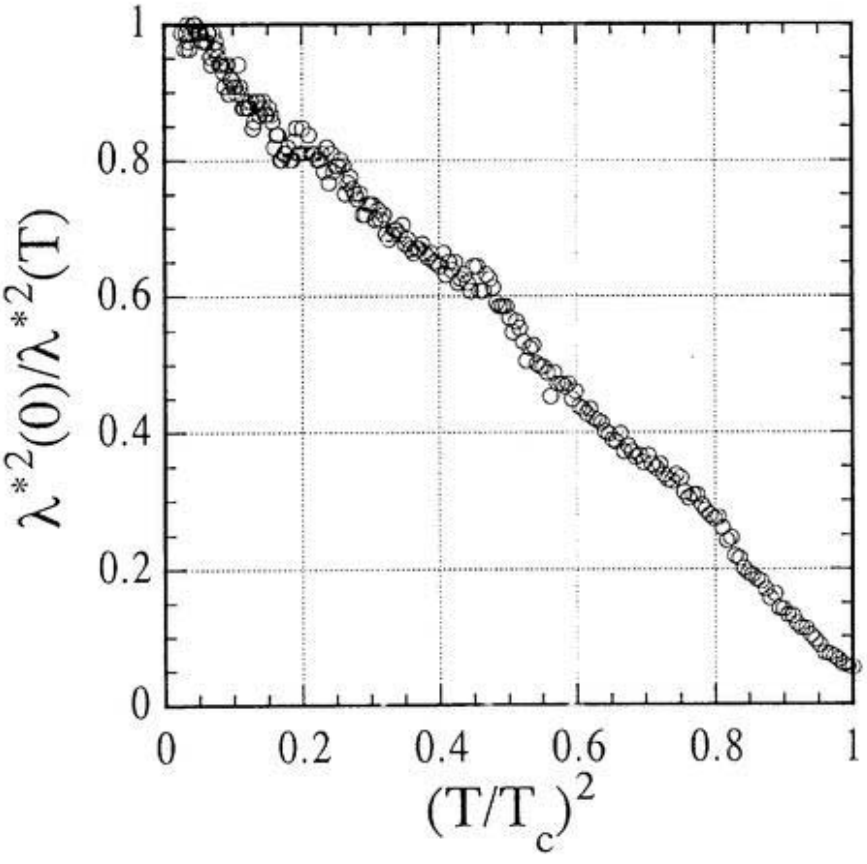

Fig. 5.6. $\lambda^{*2}(0)/\lambda^{*2}(T)$ as a function of $(T/T_c)^2$

Between these temperatures, $\Delta\lambda$ changed linearly with temperature ($\Delta\lambda$ =-1.10 + 1.87(T/T_c) with R = 0.994), but it could also be fit with a T^2-law ($\Delta\lambda$=-0.372+1.20(T/T_c)^2 with R = 0.995). The same kind of feature was observed by Klein *et al.*[7]. They attributed this bump to two conducting subsystems with different gap values and mentioned as ongoing interpretation in the frame of the induced superconductivity model. Figure 5.6 shows the $\lambda^{*2}(0)/\lambda^{*2}(T)$ vs $(T/T_c)^2$, which was fit to $\lambda^{*2}(0)/\lambda^{*2}(T) = 1-(T/T_c)^2$ with R =0.85 for $\lambda^{*}(0) = 0.693$ μm. This shows that the carriers density changes with T^2, since $\sigma_2(T)$ is proportional to $\lambda^{-2}(T)$.

5.3 Complex conductivity

The complex conductivity, $\sigma(T) = \sigma_1(T) - j\sigma_2(T)$, can be related with $R_s(T)$ and $\lambda(T)$ through $\sigma_1(T) = 2R_s(T)(\omega^2\mu^2\lambda^3(T))^{-1}$ and $\sigma_2(T) = (\omega\mu\lambda^2(T))^{-1}$. Figure 5.7 shows the $\sigma_1(T)$ and $\sigma_2(T)$ as a function of temperature. $\sigma_1(T)$ was calculated without subtracting the residual resistance R_{res}. Here, $\lambda_{tfm}(0) = 0.619$ μm corresponds to the n_s of 7.37×10^{25} m^{-3}, and n_s decreases as the rate of 9.63×10^{21} $m^{-3}K^{-2}$ with increasing T^2. It is interesting to compare our result with that measured by Srikanth *et al.*[8] using a hot-

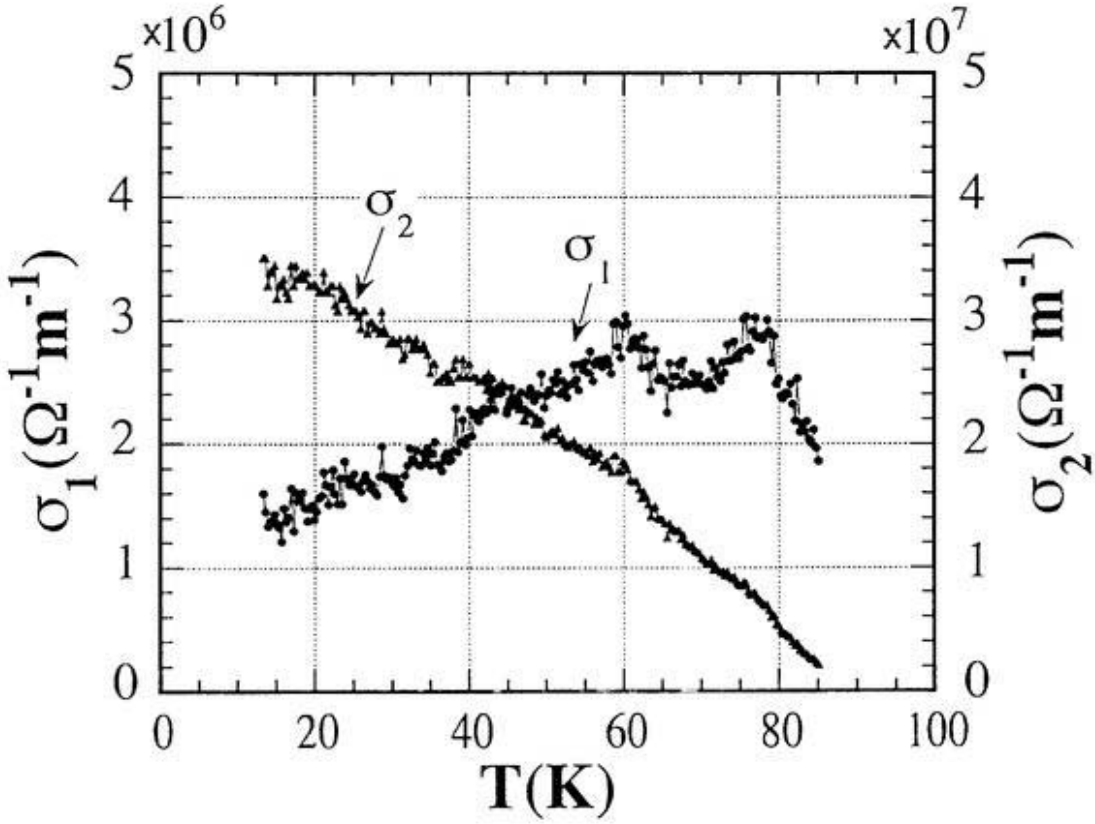

Fig. 5.7. The conductivity σ_1 and σ_2 as a function of temperature.

finger technique. They reported a complicated temperature dependence in $\sigma_2(T)$ for high-quality crystals, meanwhile $\sigma_2(T)$ obeys a simple T^2-law for our polycrystalline film. As to $\sigma_1(T)$, it increases in T^2 for $T < 40$ K. This is attributable to the increasing number of normal charge carriers and the almost constant relaxation time with increasing temperature, as predicted by the d-wave model. The absolute value of σ_1 is about one order lower than that measured by Bonn *et al.*[3], even though the difference in R_s is only a factor of about two if scaled by ν^2-law. Formally it is ascribable to the bigger $\lambda(0)$, which contributes to $\sigma_1(T)$ inverse-cubically, and this may be due to the substantial difference of samples between the high quality crystal and polycrystalline film. In Fig. 5.7, we can recognise two peaks in σ_1 below T_c: one peak at 60 K, and the other around 77 K. However, these peaks spread over a wider temperature region in comparison with the peak observed near 38 K by Bonn *et al.*[3], and these peaks were nearly the same in height, while the second peak observed by Srikanth *et al.* was much smaller in amplitude than the first one. In the simulation using Mattis-Bardeen expressions, Srikanth *et al.* attempted to attribute two peaks in σ_1 to two superconducting components.

5.4 Relaxation time

Assuming the Drude-like relaxation, $\tau(T)$ was calculated from $\sigma_1 = (x_n + x_{res})(\omega\mu\lambda^2(0))^{-1}(\omega\tau)[1+(\omega\tau)^2]^{-1}$. As shown in Fig. 5.8, the scattering time increased from about 5×10^{-13} s at closely below T_c to 1.7×10^{-12} s at 40 K and remained constant below 40 K with decreasing temperature. Meanwhile, we obtained $\tau = 1.05 \times 10^{-12}$ s at T = 0 from $\tau n_t \lambda^3(0) = 2.31 \times 10^{-5}$ s, which was derived by fitting the measured

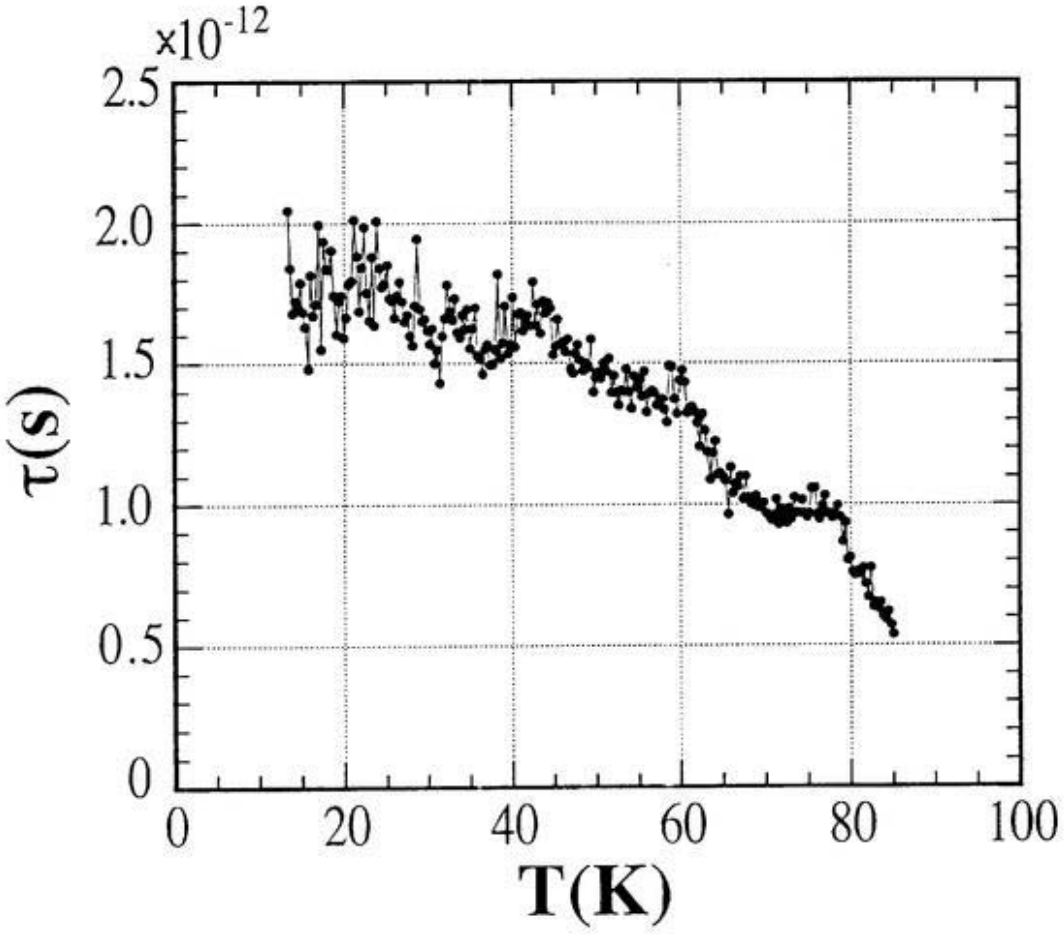

Fig.5.8. The scattering time as a function of temperature.

R_s with Eq. (3.28), $\lambda_{tfm}(0) = 0.619$ μm and x_{res} = 0.202. In other words, both estimations are consistent as far as the order is concerned. Therefore, even though the increase by a factor of 3.4 in the present experiment is small in contrast to the case of Bonn et al.[3], where $\tau = 3.6 \times 10^{-14}$ s at T_c increased to about 1.4×10^{-11} s at the low temperature limit by a factor of 400, our results are reasonable and the difference could be attributable to the sample structure. Since with decreasing T, the velocity of the dominant excitation for a d-wave model remains constant, and that for a s-wave model falls, a constant effective mean-free path corresponds to a constant τ in the former, and to an increasing τ in the latter. Therefore, in as much as a constant effective mean-free path is valid due to the effective limit in the a-b plane, the constant behaviour in τ below 40 K support a d-wave model.

5.5 Conclusion of this chapter

In conclusion, we prepared two demountable cavities, each made of copper or niobium. These are complementary each other with an improved experimental accuracy in R_s. The high-T_c films deposited on YSZ/Cr/Cu substrate exhibited a T^2 dependence in R_s, which suggests an impurity scattering among many possible explanations. The fitting by the BCS model in R_s gave an energy gap of 11.4 meV. Meanwhile, the BCS fitting in $\Delta\lambda$ gave an energy gap of 7.25 meV. The modified two-fluid model with $p = 2$ could fit over a wide temperature range both in R_s and $\Delta\lambda$. The non-zero residual carriers fraction was about 20.5%. Two peaks were observed in σ_1 at around 60 K and 77 K, which were due to the kinks at the temperatures or the straight temperature dependence in $\Delta\lambda$ between these temperatures. The quasipartical scattering time rapidly increased from about 5×10^{-13} s just below T_c to 1.7×10^{-12} s at 40 K and stayed at the value with decreasing temperature.

References

(References for Chapter 5, Precise Measurement of surface impedance)

1. E. Ezura, K. Asano, H. Hayano, K. Hosoyama, S. Inagaki, S. Isagawa, M. Kabasawa, Y. Kojima, S. Kosuge, S. Mitsunobu, T. Momose, K. Nakada, H. Nakanishi, Y. Shimbo, T. Shishido, K. Tachikawa, T. Takahashi, and K. Yoshihara, Jpn. J. Appl. Phys. **32**, 3435 (1993).
2. Jian-Fei Liu, K. Asano, E. Ezura, S. Inagaki, S. Isagawa, H. Nakanishi, M. Fukutomi, K. Komori, and M. Saito, submitted to J. Appl. Phys.
3. D. A. Bonn, R. Liang, T. M. Riseman, D. J. Baar, D. C. Morgan, K. Zhang, P. Dosanjh, T. J. Duty, A. Macfarlane, G. D. Morris, J. H. Brewer, W. N. Hardy, C. Kallin, and A. J. Berlinsky, Phys. Rev. B **47**, 11314 (1993).
4. Z. Ma, R. C. Taber, L. W. Lombardo, A. Kapitulnik, M. R. Beasley, P. Merchant, C. B. Eom, S. Y. Hou, and J. M. Phillips, Phys. Rev. Lett. **71**, 781 (1993).
5. W. N. Hardy, D. A. Bonn, D. C. Morgan, R. Liang, and K. Zhang, Phys. Rev. Lett. **70**, 3999 (1993).
6. T. Jacobs, S. Sridhar, Q. Li, G. D. Gu, and Koshizuka, Phys. Rev. Lett. **75**, 4516 (1995).
7. N. Klein, N. Tellmann, H. Schulz, K. Urban, S. A. Wolf, and V. Z. Kresin, Phys. Rev. Lett. **71**, 3355 (1993).
8. H. Srikanth, B. A. Willemsen, T. Jacobs, S. Sridhar, A. Erb, E. Walker, and R. Flükiger, Phys. Rev. B **55**, R14733 (1997).

6. The effect of the film thickness on the microwave surface impedance

6.1 Introduction

It is necessary to take into account the film thickness, magnetic field penetration depth and the thickness and dielectric and metallic properties of the substrate materials in interpreting the measured results of the microwave surface impedance of a thin film. The effect of the YBCO film thickness on the microwave surface impedance has been calculated by impedance transformation method and discussed mainly for three layers samples.

6.2 Films on dielectric substrates of infinite thickness

First we consider a superconducting film with thickness d deposited on the dielectric substrate of infinite thickness. In this case, the effective surface resistance (R_{eff}) and the effective surface reactance (X_{eff}) can be expressed as (Appendix E)

$$R_{\text{eff}} = R_s f(d/\lambda) + R_{\text{trans}}, \tag{6.1}$$

$$f(d/\lambda) = \coth(d/\lambda) + \frac{d/\lambda}{\sinh^2(d/\lambda)}, \tag{6.2}$$

$$R_{\text{trans}} = \varepsilon_r^{1/2} \frac{(\omega\mu_0\lambda)^2}{Z_0} \frac{1}{\sinh^2(d/\lambda)}, \tag{6.3}$$

$$X_{\text{eff}} = X_s \coth(d/\lambda), \tag{6.4}$$

where R_s and X_s are the intrinsic surface resistance and reactance, respectively, ε_r the relative permitivity and Z_0 the intrinsic impedance for free space. Figure 6.1 shows the $f(d/\lambda)$ as a function d/λ. It is shown that $f(d/\lambda)$ is close to unity when $d/\lambda \geq 3$. The main effect of the finite superconducting film thickness is that both the real and imaginary parts of Z_s are enhanced to some extent, depending on d/λ. This can be understood as a consequence of an altered current density distribution in the film, which furthermore leads to an enhancement of the current density j_s at the film surface by a factor $\coth(d/\lambda)$[1]. The second contribution (R_{trans}) to R_{eff} is due to power transmission into the substrate. R_{trans} decreases with growing impedance mismatch at the interface and is independent of $\tan\delta$ of the dielectric substrate, as long as the transmitted power is not reflected back to the film.

Figure 6.2 shows R_{eff} as a function of R_s calculated for different values of the film thickness d at a frequency of 13.65 GHz and $\varepsilon_r = 25$ corresponding to YSZ[2]. For the penetration depth, a 77-K value of 1000 nm was used, which roughly corresponds to the measured data shown in Fig. 5.5 of Chapter 5. According to Eq. (6.1), R_{eff} is limited by R_{trans} if R_s goes to zero.

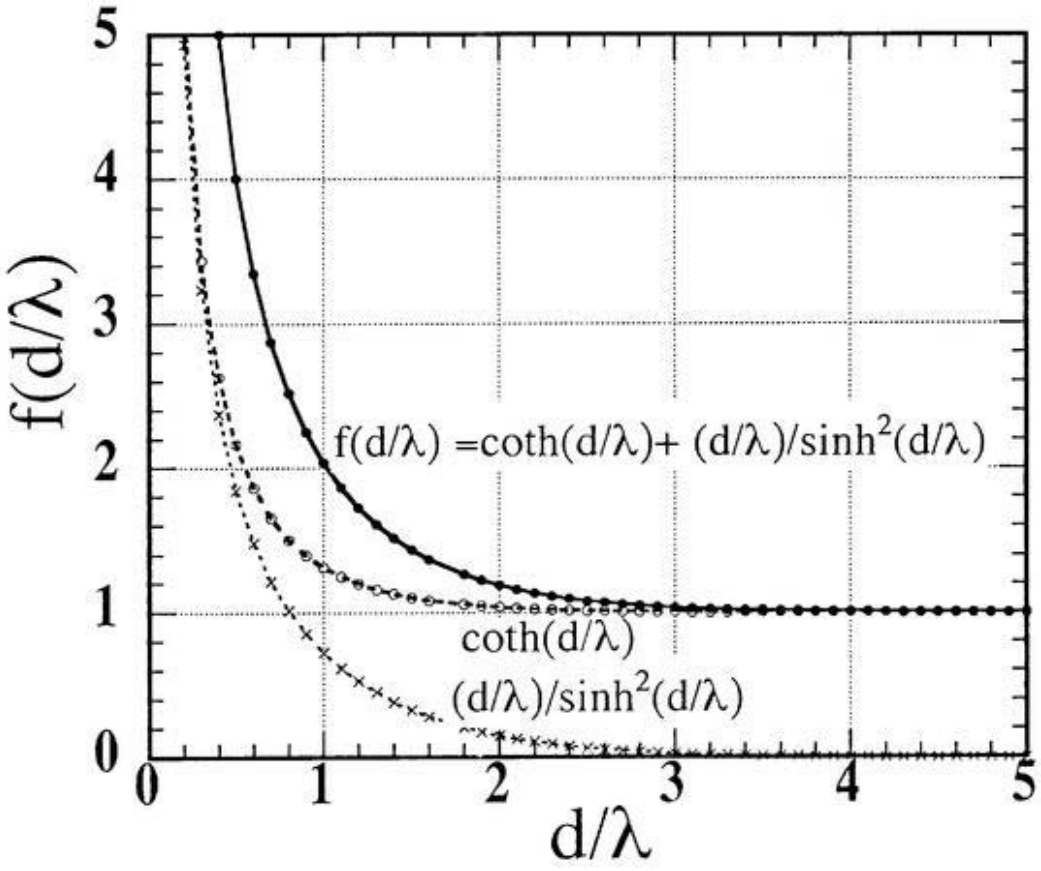

Fig.6.1. Plot of the function $f(d/\lambda) = \coth(d/\lambda) + \dfrac{d/\lambda}{\sinh^2(d/\lambda)}$.

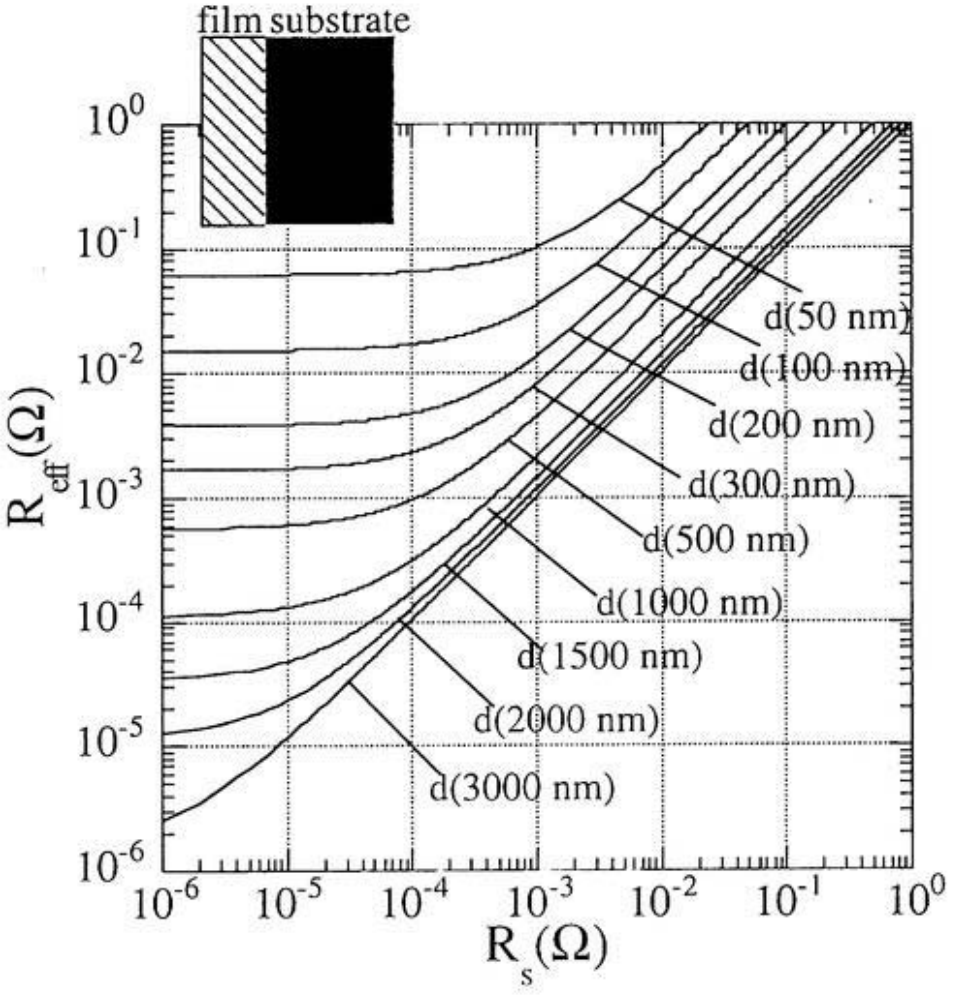

Fig.6.2. Calculated dependence of the effective surface resistance on the intrinsic surface resistance of a superconducting thin film for different values of the film thickness d.

(f = 13.65 GHZ, λ (77 K) = 1000 nm and ε_r = 25)

6.3 Films on metallic substrates with dielectric midlayer

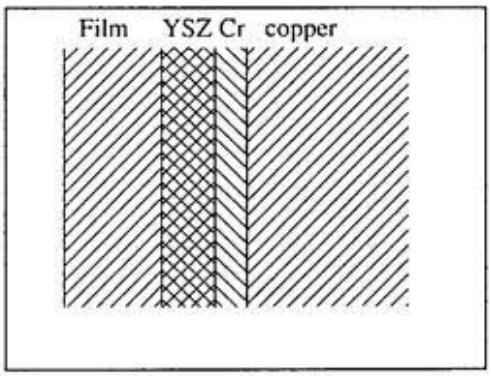

Next, we consider a sample composed of three layers as film/dielectric/metal. In our case, the YSZ buffer layer and the chromium underlayer of finite thickness are coated between the YBCO film and the copper substrate. We use the impedance transformations twice. First, the input impedance to the interface between the film and YSZ, Z, can be determined using Eq. (7) in Appendix E by

$$Z = Z_{YSZ}\frac{Z_m / Z_{YSZ} + i\tan(\beta_1 d_1)}{1 + i(Z_m / Z_{YSZ})\tan(\beta_1 d_1)}, \tag{6.5}$$

where the wave number β_1 in the YSZ material is given by $\beta_1 = \omega\mu/Z_{YSZ}$, d_1 the thickness of YSZ layer, Z_m the input impedance to the chromium layer given by Eq. (5) in Appendix E, and Z_{YSZ} the impedance of YSZ material given by $Z_{YSZ} = \frac{Z_0}{\varepsilon_r}(1 + \frac{i}{2}\tan\delta)$. By using Eq. (7) of Appendix E again, the effective impedance of the film, Z_{eff}, can be obtained.

$$Z_{eff} = Z_s\frac{Z / Z_s + i\tan(\beta d)}{1 + i(Z / Z_s)\tan(\beta d)}, \tag{6.6}$$

where Z_s is the intrinsic impedance the YBCO film, β the wave number, and d the thickness of the film.

6.4Results and discussion

In the present study, the samples (as described in Chapter 2) composed of four layers: a YBCO layer of thickness about 1.5 — 2 μm, a YSZ layer of thickness 0.8 μm, a chromium layer of thickness 0.5 μm and a copper substrate of thickness 3 mm. Since the resistivity, ρ, of chromium is 0.5×10^{-8} Ωm and that of copper is 0.2×10^{-8} Ωm at 77 K, the assumption to the chromium layer with infinite thickness is assumed for simplicity. For this three-layered structure, we calculated numerically the effective surface resistance R_{eff} as a function of the real surface resistance R_s. The calculation was based upon the impedance transformations between two different materials. The results are shown in Fig. 6.3 and Fig. 6.4, where we used $\varepsilon_r = 25$ for the YSZ dielectric constant, and $\rho_{Cr} = 0.5 \times 10^{-8}$ Ωm for the substrate resistivity. Figure 6.3 and Figure 6.4 show R_s in different scales, i.e., Fig. 6.3 for R_s from 10^{-6} Ω to 10^{-1} Ω and Fig.6.4 for R_s from 10^{-2} Ω to 1 Ω

We apply the above calculation to the measured data given in Chapter 5. From Fig. 5.1, the measured surface resistance (R_{eff}) is about 10 mΩ at 70 K. The measured penetration depth λ ($\lambda = \lambda(0)+\Delta\lambda$) at 70 K is about 0.87 μm, which was obtained from Δλ about 0.4 μm in Fig. 5.5 and λ(0) around 0.47 μm derived from Δλ curved in Fig. 5.5 using the modified two-fluid model. In Fig. 6.3, we see that the real surface resistance R_s is 10 mΩ for R_{eff} = 10 mΩ and λ = 0.87 μm. This indicates that the effect of film thickness and the substrate is negligible at 70 K. As shown in Fig. 5.1 and Fig. 5.5, both R_{eff} and λ decreases at the temperature decreases from 70 K, and at 4.2 K $R_{eff} \approx$

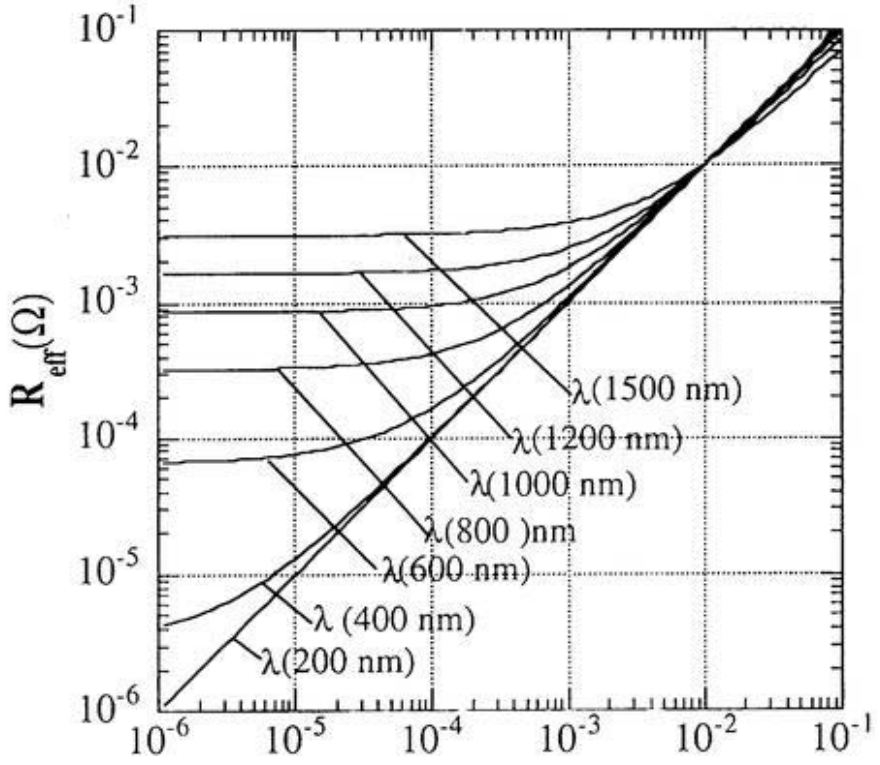

Fig.6.3 Calculated dependence of the effective surface resistance on the intrinsic surface resistance of a superconducting thin film for different values of penetration depth.

(f = 13.65 GHz, ε_r = 25 and ρ_{Cr} = 0.5E-8 at 77 K)

1 mΩ and $\lambda \approx 0.47$ μm. From these values and Fig. 6.3, it is obvious that the relationship $R_{eff} \approx R_s$ holds in the whole temperature range below 70 K. However, some amount of correction are required above 70 K, or, for R_{eff} larger than 10 mΩ.

Figure 6.4 shows that R_{eff} saturates when R_s increases up to 0.15. Before saturation, R_{eff} is slightly enhance if $\lambda \leq 1$ μm, and somewhat lowered if $\lambda \geq 1$ μm. This result makes a sharp contrast to the infinite thickness dielectric substrate case shown in Fig. 6.2, where R_{eff} is enhanced in the whole range of R_s and d values. Since, at

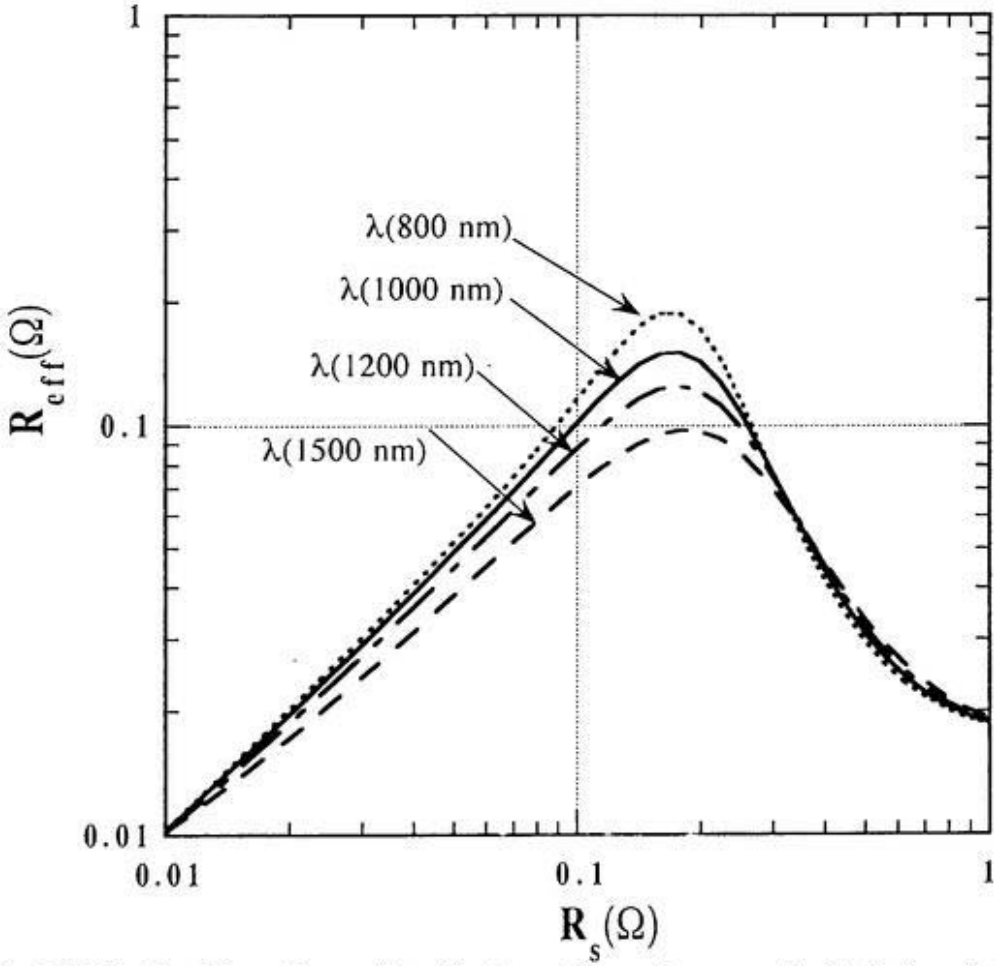

Fig.6.4. Calculated dependence of the effective surface resistance on the intrinsic surface resistance of a superconducting thin film for different values of penetration depth.

temperatures close to T_c, λ is larger than 1 μm, R_{eff} is lower than R_s to some extent depending on the value of λ. This means that R_{eff} for three layer metallic substrate case exhibits less sharp rf transition compared to the real resistance R_s or to R_{eff} for infinite thickness dielectric substrate case.

In conclusion, the measured surface resistance R_{eff} is almost equal to the real surface resistance R_s in the temperature range below 70 K. However, R_{eff} is lowered above 70 K to some extent depending on λ, and needs some corrections.

References

1. N. Klein, H. Chaloupka, G. Müller, S. Orbach, H. Piel, B. Roas, L. Schultz, U. Klein and M. Peiniger, J. Appl. Phys. **67**, 6940 (1990).

2. J. M. Phillips, Appl. Phys. Rev. 79, 1829 (1996).

7. Microwave field dependence of the surface resistance

7.1 Introduction

For the application to accelerating cavities it is important to study the R_s field dependence of high-T_c films deposited onto large-area metallic substrates. We adopted demountable cavity method[1-7] which is suitable for measuring R_s of large area samples, while most of the field-dependence measurements reported so far have been made by stripline methods[8-10] in small area films fabricated on dielectric substrates[8-13]. We used three c-axis oriented YBCO samples EC230, EC231 and EC232 for the present study[5,6], which are refered to as A, B and C, respectively.

7.2 Measurement techniques

The microwave field dependence of R_s was measured by the experimental setup as shown in Fig. 7.1. The cavity consisted of an endplate and a copper cylinder with bottom endplate. It was 33 mm in diameter, 19 mm in length, and operated at 13.6 GHz in the TE_{011} mode. The temperature of the cavity was controllable from 11 K to 300 K

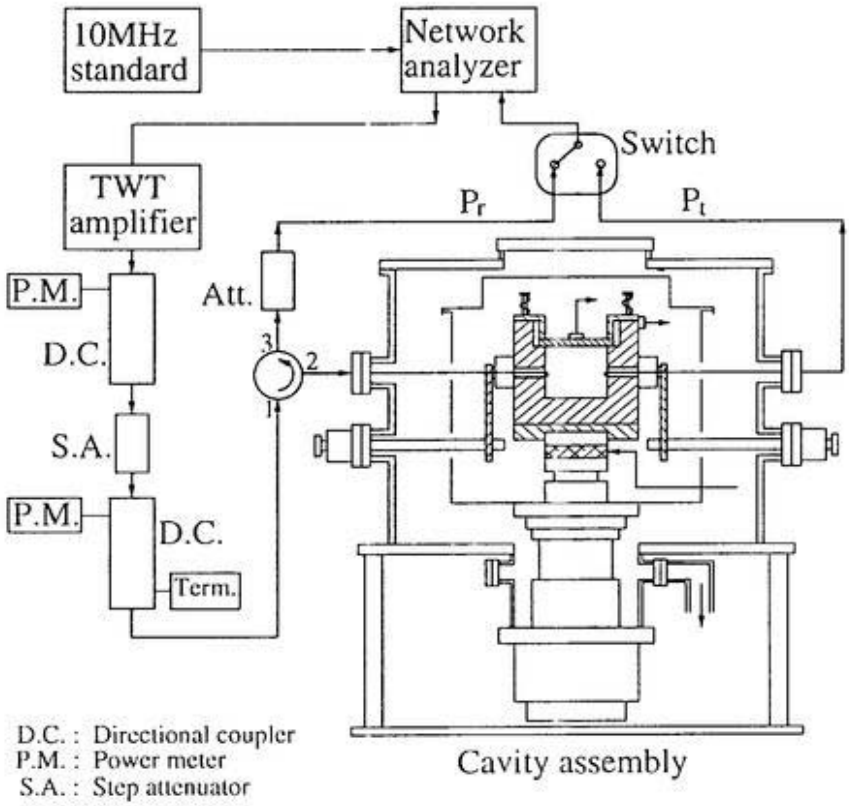

Figure 7.1: The experimental setup to measure the microwave field dependence of the surface resistance in YBCO films.

by a closed-cycle refrigerator and a 50 W heater with an autotuning temperature controller. At a fixed temperature, network analyzer found the resonant frequency f_0 and 3-dB bandwidth Δf, from which the loaded quality factor was calculated. The incident power P_{in} was varied from about 0.1 mW to about 1.5 W. The coupling coefficient β_1 and β_2 were tuned to about 0.8 and about 0.001, respectively. The surface resistance of high-T_c films can be obtained from measurements[52,54] of both high-T_c films and copper endplate. The dissipation power P_d of the cavity was found from $P_d = P_{in} - P_{ref} - P_t$, where the reflection power P_{ref} is evaluated from P_{in} and β_1, and the transmission power P_t is negligible in comparison with P_{ref}. As discussed in Sec. 3.5.3, the maximum surface magnetic field occurs on the endplate at around the middle of the radius, and is expressed for TE_{011} mode as

$$\left|H_{r,\max}\right| = 0.325\left[\frac{\varepsilon_0}{\mu_0}\right]^{\frac{1}{4}}\left[\frac{1}{a}\right]\left[\frac{\lambda_r}{l}\right]^{\frac{3}{2}}\sqrt{P_d Q_0}\ , \tag{7.1}$$

where ε_0 is the permittivity of free space, μ_0 the permeability of free space, λ_r the resonant wavelength, r the distance from the center line of cavity, $\dot{q_{01}}$ the first root of Bessel's equation $J_0'(x) = 0$, a the radius of cavity, and l the length of cavity. Inserting measured values of Q_0 and P_d into Eq. (7.1), we can obtain the maximum surface magnetic field in the cavity. In the following we use H_{rf} instead of $\left|H_{r,\max}\right|$ for simplicity.

7.3 Experimental results and discussions

Utilizing the measurement system described above, we measured R_s as a function of applied microwave surface field H_{rf} for the three samples. Figure 7.2 (a) and (b)

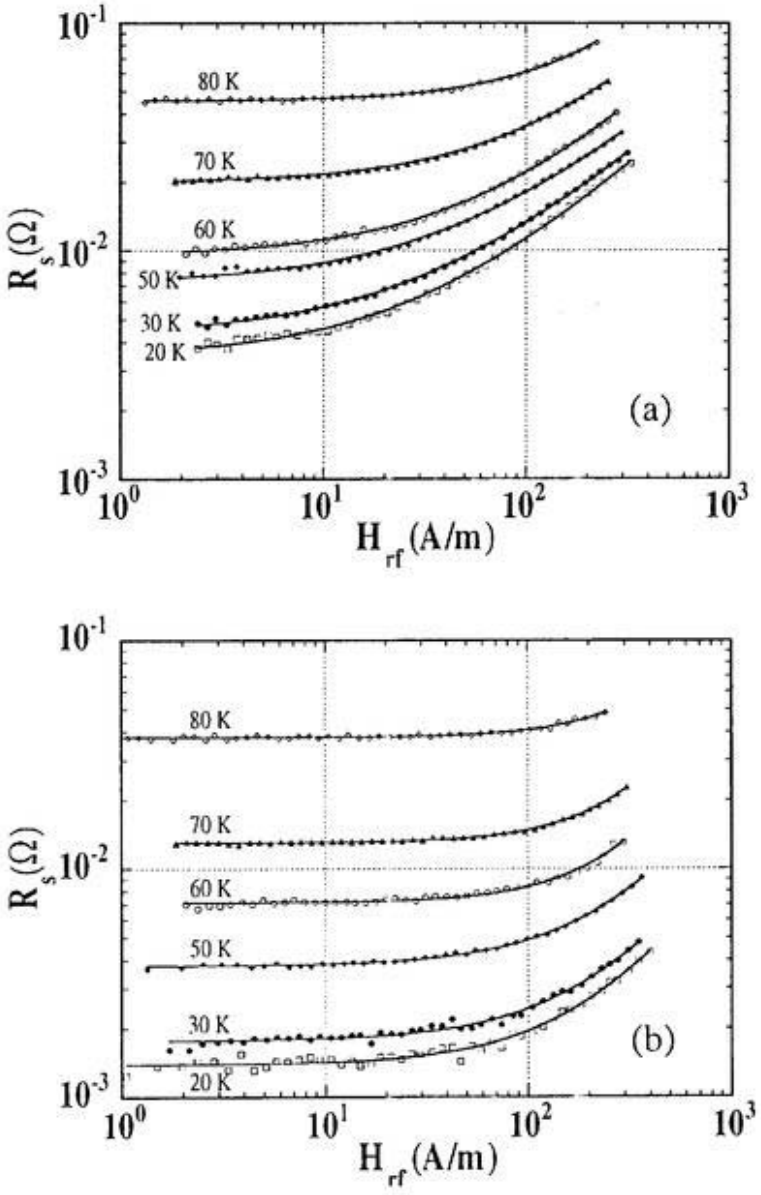

Figure 7.2. (a) and (b): The microwave magnetic field dependence of the surface resistance at six different temperatures from 20 K to 80 K (a) for sample A, (b) for sample B.

show the measured results at six different temperatures from 20 K to 80 K for sample A and B, respectively. When H_{rf} was at low field levels, the surface resistance stayed almost constant. For sample B, the surface resistance, $R_s(H_{rf},T)$, became apparently larger than those at low field levels when H_{rf} was greater than about 100 A/m. Meanwhile, for sample A, the surface resistance deviated from $R_s(H_{rf} \approx 0,T)$ when the magnetic field exceeded about 10 A/m. The data $R_s(H_{rf} \approx 0,T)$ was obtained[14] by using both copper and niobium cavities as discussed in Chapter 5. Figure 7.3 shows R_s versus T with H_{rf} as a parameter. The solid line indicates the data of $R_s(H_{rf} \approx 0,T)$.

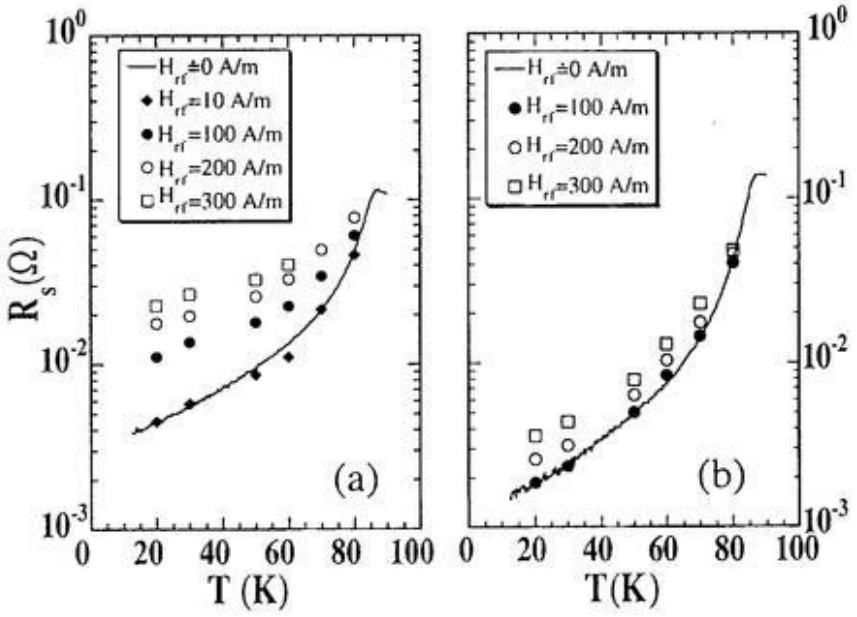

Figure 7.3: The surface resistance as a function of temperature at different microwave magnetic fields (a) for sample A and (b) for sample B. The solid line shows the data obtained previously in near zero fields.

The various models have been proposed to explain the microwave response of high-T_c materials. Coupled-grain model[15-17] treated high-T_c films as a network of superconducting grains coupled via Josephson junctions. A quadratic field dependence of R_s at field levels below 4000 A/m was reported by Nguyen *et al.*[16] with a developed coupled-grain model. On the other hand, a linear field dependence of R_s was obtained by Portis *et al.*[18] with a model based upon the critical state model of Bean[19].

We fitted the experimental data with the expression

$$R_s(H_{rf},T) = R_s(H_{rf} \approx 0,T)[1 + q(T)H_{rf}^{g(T)}], \tag{7.2}$$

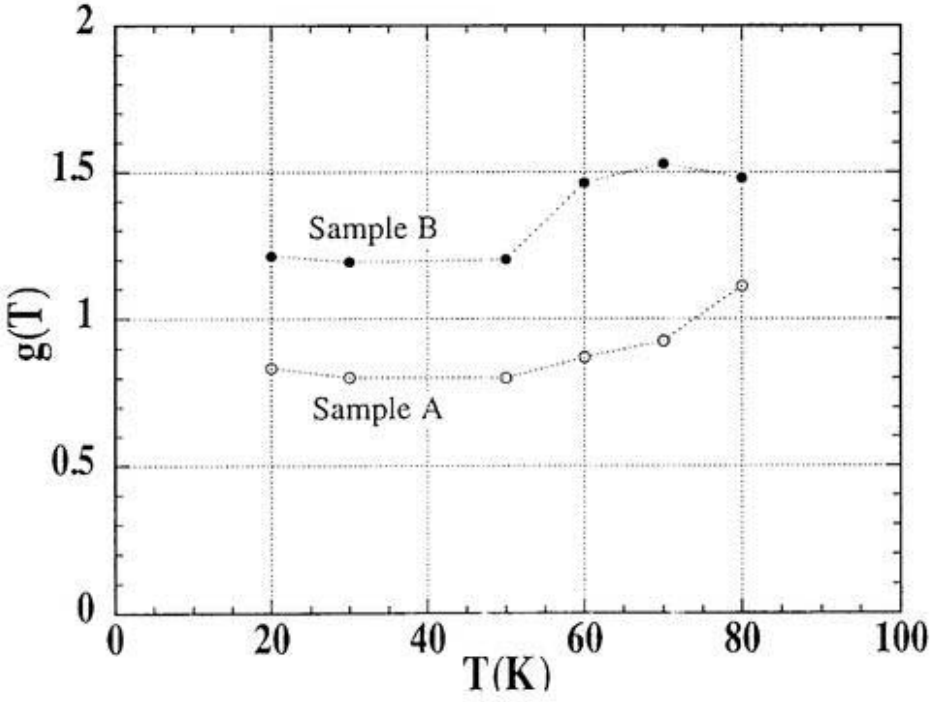

Figure 7.4: The fitting parameter g(T) by fitting data with

$R_s(H_{rf},T) = R_s(H_{rf} \approx 0,T)[1 + q(T)H_{rf}^{g(T)}]$

where $q(T)$ and $g(T)$ were the fitting parameters related to the temperature. The fitting curves are shown with solid lines in Fig. 7.2 (a) and (b). The curve of $g(T)$, as shown in Fig. 7.4, remained flat in a low temperature region, and bent around 50 K. The $g(T)$ was about 0.8 for sample A and 1.2 for sample B at temperatures below 50 K. This indicated a linear field dependence of $R_s(H_{rf},T)$ rather than a quadratic field dependence. For the temperature above 50 K, the value of $g(T)$ increased. However, it was still not large enough to indicate the quadratic field dependence.

A linear field dependence of R_s was obtained by Portis *et al.* In Portis model based upon the critical state model of Bean, the interaction between the microwave currents and free or pinned fluxons created by an external field was considered. The dissipation was calculated during the vortices movement along grain boundaries against the Lorentz force.

The surface power absorption per unit area is given by

$$\frac{dP_s}{dA} = \frac{1}{2} R_s J_s^2, \tag{7.3}$$

where $J_s(\text{A/m}) = \int J dx = H_s(\text{A/m})$ is the peak surface current density, giving for the absorption rate $\frac{dP_s}{dA} = \frac{1}{2} R_s H_s^2$.

The work performed in a microwave period per unit area is the integral over a cycle as

$$W_s = \int H d\phi_s \ (\text{Joule/m}^2 - cycle). \tag{7.4}$$

The surface flux density is given by $\phi_s = \int B dx = \frac{1}{2}\frac{\mu}{J_c} H^2$ with the critical-state field gradient related to the critical current density J_c by $\frac{dH}{dx} = \pm J_c$. The work performed per microwave period is,

$$W_s = \frac{2\mu}{3}\frac{H_s^3}{J_c} \text{ (Joule/m}^2\text{ - cycle)}, \tag{7.5}$$

where H_s is the peak microwave field. The power absorbed per unit area of surface is

$$P_s = \frac{\omega}{2\pi} W_s = \frac{1}{2} R_s J_s^2 (\text{Joule/m}^2) = \frac{1}{2} R_s H_s^2 (\text{Joule/m}^2). \tag{7.6}$$

Finally, the surface resistance is

$$R_s = (\frac{4\mu_0}{3})(\frac{\omega}{2\pi})(\frac{H_s}{J_c}) \text{ (H_s in A/m, J_c in Ã/m}^2\text{)}. \tag{7.7}$$

The surface resistance, $R_s = (\frac{4\mu_0}{3})(\frac{\omega}{2\pi})(\frac{H_s}{J_c})$, is linear in the magnitude of the microwave magnetic field H_s. The microwave power dependence $R(H)$ of the surface resistance gives the value of the critical current density as

$$J_c\left[\text{A/cm}^2\right] = \frac{0.167 \cdot f[\text{GHz}]}{R_s[\Omega] \Big/ H[\text{A/m}]}. \tag{7.8}$$

According to the Portis model, the critical current density J_c is inversely proportional to the slope of $R_s(H_{rf}, T)$ given by Eq. (7.8). From the measured $R_s(H_{rf}, T)$ at different temperatures, the critical current density $J_c(T)$ was extracted as shown in Fig. 7.5 for film A, B and C. At 20 K, the J_c for sample B and C was about

2.8×10^5 A/cm^2. On the other hand, the J_c of film A was about one order lower than that of film B and C. At 77 K, J_c of 4×10^4 A/cm^2 for film B and C, and J_c of 1.2×10^4 A/cm^2 for film A were obtained. The T-dependence of J_c using a form of $J_c(T) \propto (1-T/T_c)^m$ was fitted with m of 0.61, 1.16 and 1.36 for film A, B and C, respectively.

The J_c obtained above for film B and C at 77 K was consistent with J_c of about 3×10^4 A/cm^2 obtained previously in transport measurements[20] for these three films. The observation by an optical microscope showed that the smoothness of surface in sample B and C was better than that of sample A, which may be the reason of the difference in J_c. The current flow at microwave frequencies for both type I and II

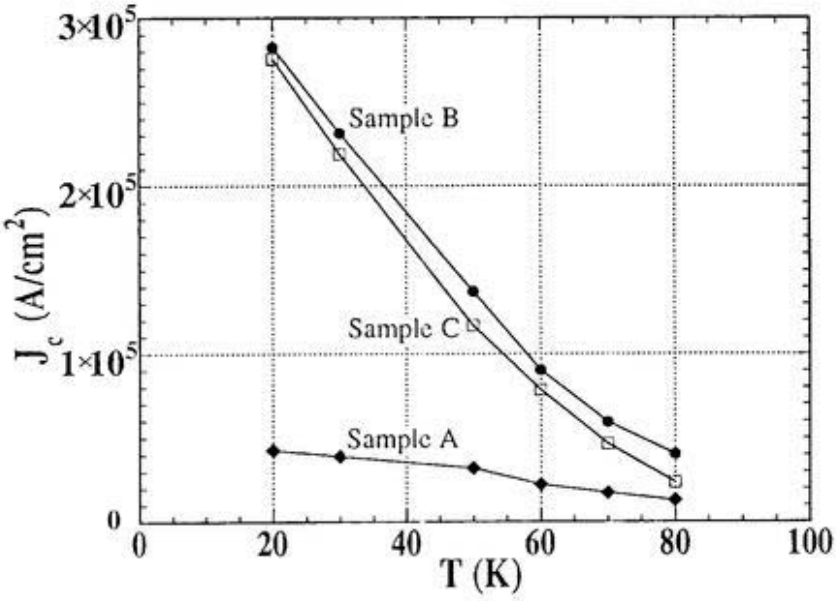

Figure 7.5: The critical current density at six different temperatures from 20 K to 80 K for sample A, B, and C.

superconductors is concentrated on the film surface, and decays exponentially from the surface with a London penetration depth. On the contrary, the J_c in dc is uniformly distributed across the cross section for type II superconductors. The effect of the roughness becomes more severe with decreasing temperature since the penetration depth decreases with decreasing temperature. Figure 8.5 shows this tendency; J_c of film B or C is almost 10 times as large as that of film A at 20 K, while only 3 times at 77 K.

7.4 Summary

We established the microwave field dependence measurement system, and measured R_s in YBCO films on copper substrate. Up to 400 A/m, a linear dependence of R_s on the microwave magnetic field was observed at temperatures below 50 K, and the dependence deviated from the linearity above 50 K. From the measured field dependence of R_s, the critical current density for three samples was obtained, and varied in the form of $(1-T/T_c)^m$ with m of 0.61, 1.16 and 1.36.

References

(References for Chapter 7, Microwave field dependence of the surface resistance)

1. D. W. Cooke, P. N. Arendt, E. R. Gray, B. L. Brown, N. E. Elliott, G. A. Reeves, A. D. Rollett, K. M. Hubbard, and A. M. Portis, Appl. Phys. Lett. **58**, 1329 (1991).
2. B. Zhang, P. Fabbricatore, G. Gemme, R. Musenich, R. Parodi, and P. Capobianco, J. Supercond. **8**, 753 (1995).
3. E. Ezura, K. Asano, H. Hayano, K. Hosoyama, S. Inagaki, S. Isagawa, M. Kabasawa, Y. Kojima, S. Kosuge, S. Mitsunobu, T. Momose, K. Nakada, H. Nakanishi, Y. Shimbo, T. Shishido, K. Tachikawa, T. Takahashi, and K. Yoshihara, Jpn. J. Appl. Phys. **32**, 3435 (1993).
4. Jian-Fei Liu, K. Asano, E. Ezura, M. Fukutomi, S. Inagaki, S. Isagawa, K. Komori, H. Nakanishi, M. Tosa, and K. Yoshihara, Proc. 1995 Particle Accelerator Conf., Dallas, 1995, p. 1652 (1995).
5. Jian-Fei Liu, K. Asano, E. Ezura, S. Inagaki, S. Isagawa, H. Nakanishi, M. Fukutomi, K. Komori, and M. Saito, Appl. Phys. Lett. 73, 3450 (1998).
6. Jian-Fei Liu, K. Asano, E. Ezura, M. Fukutomi, S. Inagaki, K. Komori, H. Nakanishi, and M. Saito, Proc. 1998 1st Asian Part. Accel. Conf., Tsukuba, Japan (1998).
7. S. Inagaki, E. Ezura, Jian-Fei Liu, and H. Nakanishi, J. Appl. Phys. **82**, 5401 (1997).
8. P. P. Nguyen, D. E. Oates, G. Dresselhaus, and M. S. Dresselhaus, Phys. Rev. B **48**, 6400 (1993).

9. Y. M. Habib, C. J. Lehner, D. E. Oates, L. R. Vale, R. H. Ono, G. Dresselhaus, and M. S. Dresselhaus, Phys. Rev. B **57**, 13833 (1998).

10. D. E. Oates, P. P. Nguyen, Y. M. Habib, G. Dresselhaus, M. S. Dresselhaus, G. Koren, and E. Polturak, Appl. Phys. Lett. **68**, 705 (1996).

11. G. Hampel, P. Kolodner, P. L. Gammel, P. A. Polakos, E. de Obaldia, P. M. Mankiewich, A. Anderson, R. Slattery, D. Zhang, G. C. Liang, and C. F. Shih, Appl. Phys. Lett. **69**, 571 (1996).

12. W. Rauch, E. Gornik, G. Sölkner, A. A. Valenzuela, F. Fox, and H. Behner, J. Appl. Phys. **73**, 1866 (1993).

13. M. A. Hein, C. Bauer, W. Diete, S. Hensen, T. Kaiser, G. Müller, and H. Piel, J. Supercond. **10**, 109 (1997).

14. Jian-Fei Liu, K. Asano, E. Ezura, S. Inagaki, S. Isagawa, H. Nakanishi, M. Fukutomi, K. Komori, and M. Saito, submitted to J. Appl. Phys.

15. T. L. Hylton, A. Kapitulnik, M. R. Beasley, J. P. Carini, L. Drabeck, and G. Grüner, Appl. Phys. Lett. **53**, 1343 (1988).

16. T. L. Hylton and M. R. Beasley, Phys. Rev. B **39**, 9042 (1989).

17. C. Attanasio, L. Mariato, and R. Vaglio, Phys. Rev. B **43**, 6128 (1991).

18. A. M. Portis, D. W. Cooke, and H. Piel, Physica C **162-164**, 1547 (1989).

19. C. P. Bean, Phys. Rev. Lett. **8**, 250 (1962).

20. M. Fukutomi, S. Aoki, K. Komori, R. Chatterjee, and H. Maeda, Physica C **219**, 333 (1994).

8. Microwave surface resistance of a-b plane well-textured and weakly-textured films

8.1 Introduction

For application of high-T_c films to accelerator cavities, low surface resistance should be realized even at high RF magnetic fields. It is well known that a c-axis texturing perpendicular to the film surface is inevitable to reduce the surface resistance and its field dependence. However, the effect of a-b plane texturing on the surface resistance is not so clear from lack of experiments, especially for films deposited on metallic substrates. We prepared four YBCO films with c-axis texturing normal to the film surface; two of them were a-b plane well textured and the other two were a-b plane weakly textured. For these two kinds of films, the surface resistance was measured as a function of temperature at low RF fields. The dependence of the surface resistance on the RF field intensity was also measured for these films.

8.2 Film structure

As described in Chapter 2, the texturing of YSZ buffer layer is crucial to obtain the a-b plane textured YBCO films. YSZ films with inplane textured over the whole surface area were obtained by a modified bias sputtering technique as shown in Fig. 2.3. The copper substrates precoated with the YSZ/Cr buffer layer were used for deposition of YBCO films using laser ablation technique. By this fabrication technique, two pairs of YBCO sample were prepared in order to know the effect of in plane texturing on surface resistance.

The list of YBCO films used for the measurement is given in Table 8.1. The x-ray diffraction patterns and pole figures showed that the structure of films EC391 and EC425 is c-axis normal to the film surface and a-b plane weakly-textured, and that of samples EC392 and EC403 is c-axis normal to the surface and a-b plane well-textured. The samples of EC391 and EC392 are named the first pair, and their x-ray diffraction patterns and pole figures are shown in Fig. 8.1 and Fig. 8.2, respectively. Correspondingly, EC425 and EC403 make the second pair.

Table 8.1. List of YBCO samples

	Weakly-textured in a-b plane (c-axis normal to the film surface)	Well-textured in a-b plane (c-axis normal to the film surface)
1st pair	EC391	EC392
2nd pair	EC425	EC403 and EC407

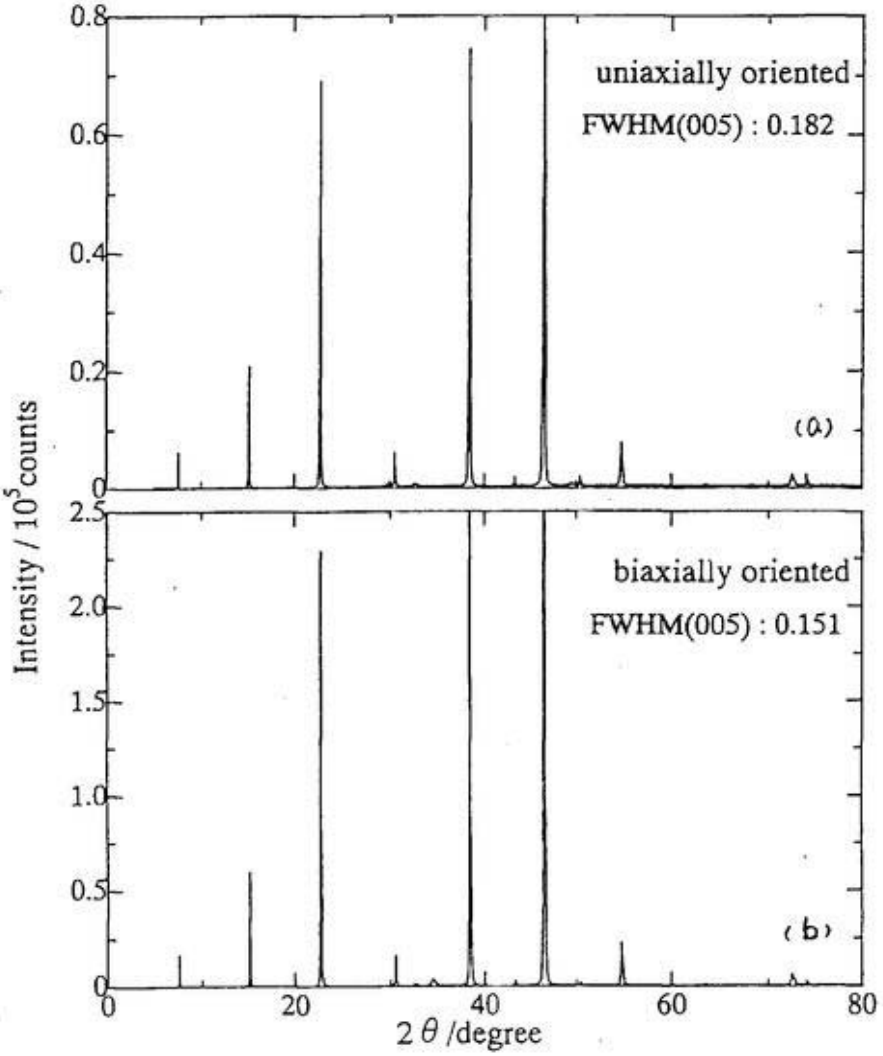

Fig. 8.1. X-ray diffraction patterns for YBCO thin films deposited on copper substrate, (a) for EC391, (b) for EC392.

Figure 8.3 shows a SEM image of a well-textured film. Rectangular or square grain shape shown in Fig. 8.3 indicates that the film is well textured. On the other hand,

the grain shape of a weakly-textured or untextured films is round, as shown in Fig. 2.9 (a), (b) and (c) in Chapter 2.

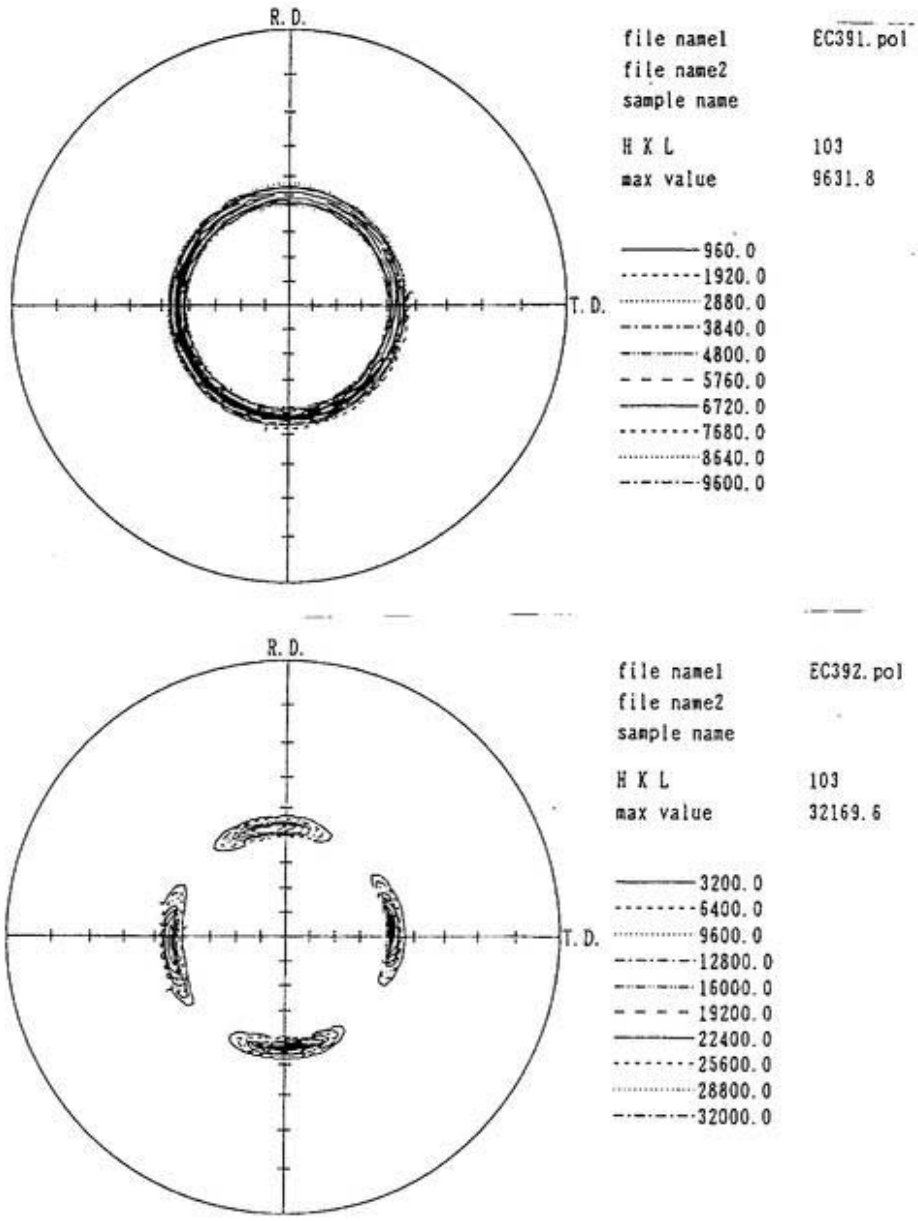

Fig. 8.2. X-ray pole figures for YBCO thin films deposited on copper substrate, (a) for EC391, (b) for EC392.

Fig. 8.3. SEM image of well-textured YBCO thin films deposited on copper substrate.

8.3 Temperature dependence

The temperature dependence of the surface resistance for both well-textured and weakly-textured YBCO films was measured by a demountable cavity method described in detail in Chapters 4 and 5. For the two pair samples, we measured the surface resistance in a wide temperature region from 15 K to 300 K. The critical temperature T_c, defined as the temperature at which dR_s/dT takes a maximum, was about 86 K for the present samples.

It is expected that the $R_s(T)$ for the well-textured films decreases more sharply than that of weakly-textured films with temperature decreasing from T_c. As shown in Fig. 8.4 and Fig.8.5, the maximum of dR_s/dT is 0.0425 $\Omega/\bar{K}$ for sample EC392, and

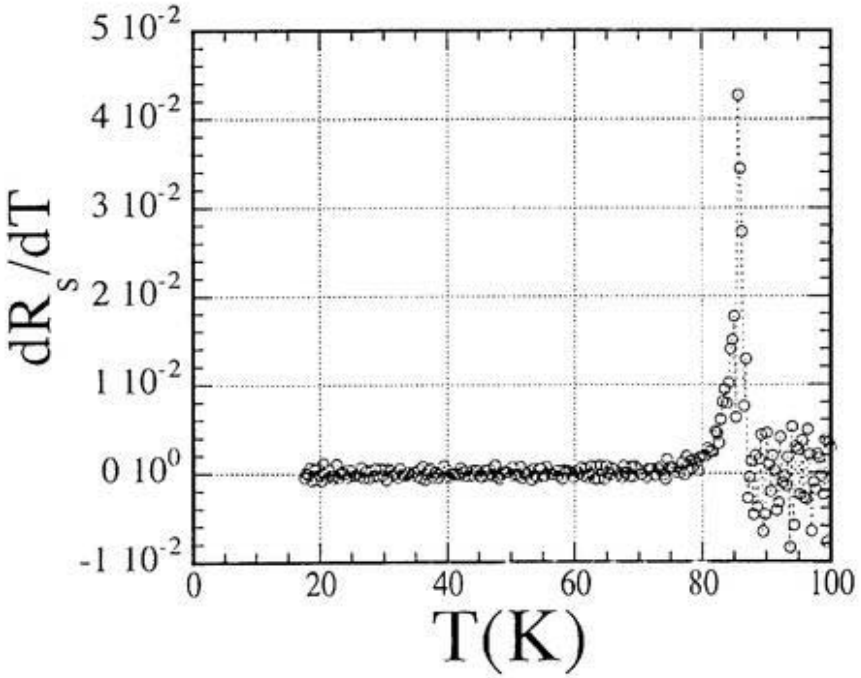

Fig.8.4. The value of dR_s/dT vs the temperature for same EC392.

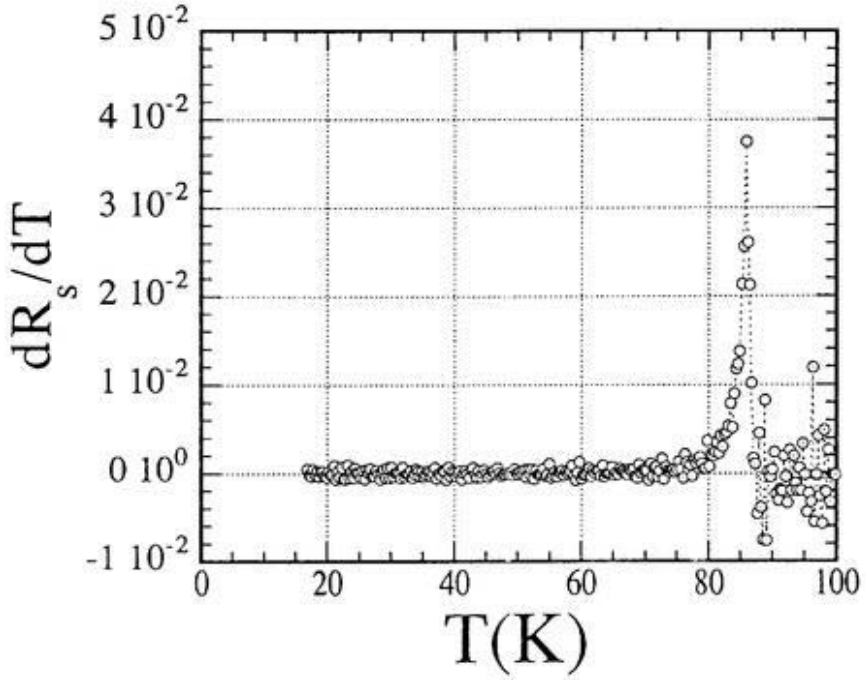

Fig.8.5. The value of dR_s/dT vs the temperature for same EC391.

0.038 Ω/K for EC391, which is consistent with the expectation. However, the peak width of dR_s/dT for EC391 is almost the same as that of EC392. Similar behavior was also observed for the second pair of films.

Figure 8.6 shows the surface resistance as a function of temperature for EC391 with open squares and EC392 with open circles. The results obtained with Nb host cavity are also shown in the figure with crosses. The data calibration, as described in Chapter 5, was applied in order to improve the data accuracy at low temperatures. The surface resistance of the weakly-textured film EC391 become lower than that of the well-textured film EC392 when the temperature decreases to below 70 K. At 20 K, the surface resistance of 0.15 mΩ was observed for EC391 and 1.3 mΩ for EC392. The surface resistance for the weakly-textured film EC391 was almost one order lower than

that of the well-textured film EC392. The results obtained from the second pair of samples also showed that the microwave surface resistance in weakly-textured films exhibits a lower value than that of well-textured films at low temperatures.

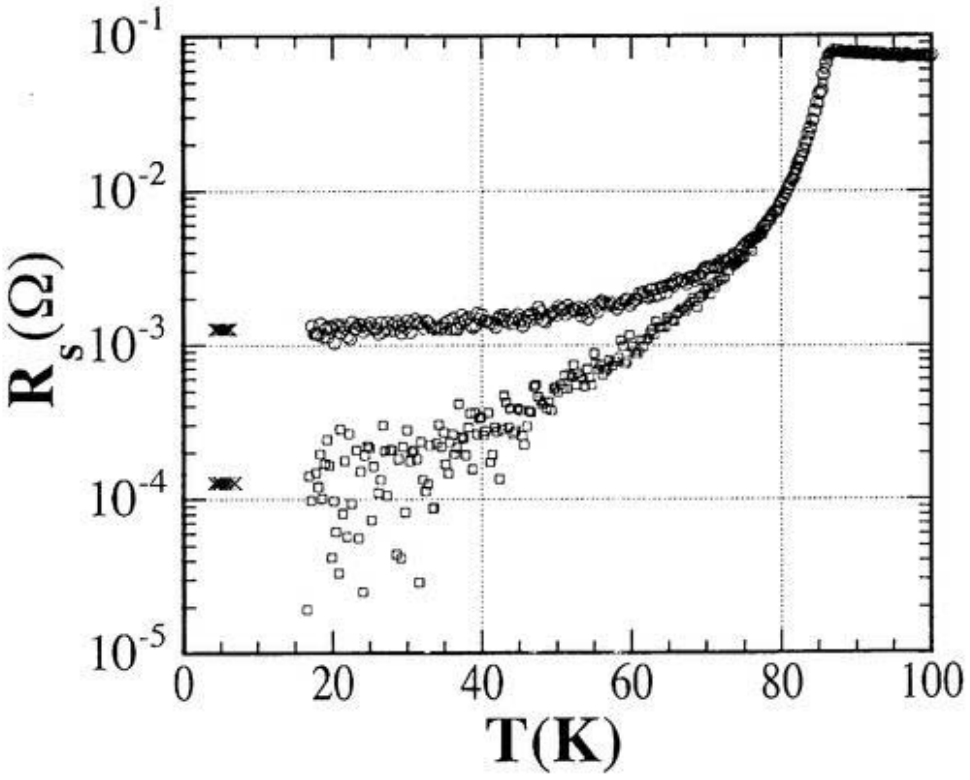

Fig.8.6. The temperature dependence of the surface resistance of samples EC391(squares) and EC392(open circles).

8.4 Field dependence

It is very important for the application to accelerator cavities to know the response of the surface resistance to application of the rf fields. The field dependence of the surface resistance both for well-textured and weakly-textured YBCO films has been studied up to a field level of 1000 A/m at the fixed temperatures from 20 K to 80 K. In chapter 4, the experimental setup was described in detail. Figures 8.7 (a), (b), (c) and (d) show the surface resistance as a function of microwave magnetic field for the sample EC391, EC392, EC425 and EC403, respectively. With increasing field levels, the

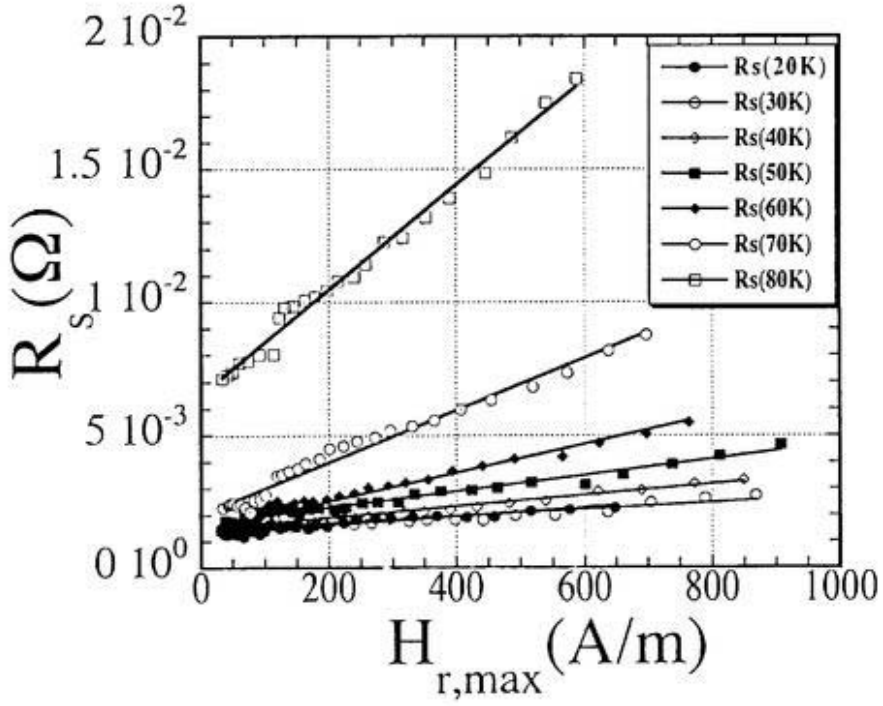

Fig.8.7 (a). The microwave magnetic field dependence of the surface resistance for sample EC391.

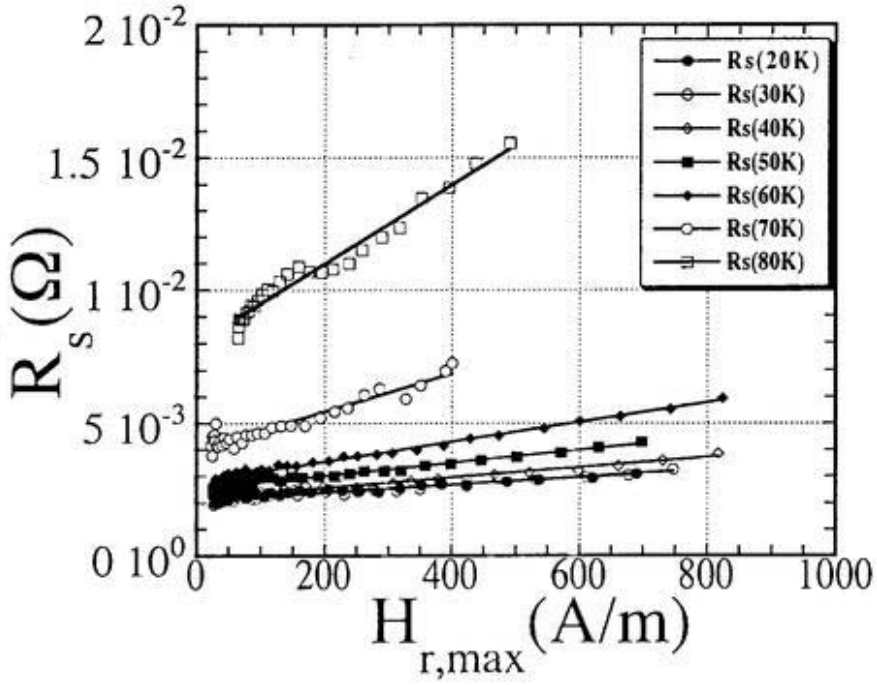

Fig.8.7 (b). The microwave magnetic field dependence of the surface resistance for sample EC392.

surface resistance in the films EC391 and EC425 increases faster than that of the films EC392 and EC403, i.e. the slope of $R_s(H)$ for films EC391 and EC425 is greater than that in the films EC392 and EC403. By the critical-state model described in Chapter 7, we calculated the critical current density for these samples as shown in Fig. 8.8. It is clearly showed that the critical current density of c-axis textured and a-b plane well-textured films is higher than that of c-axis textured and a-b plane weakly-textured films.

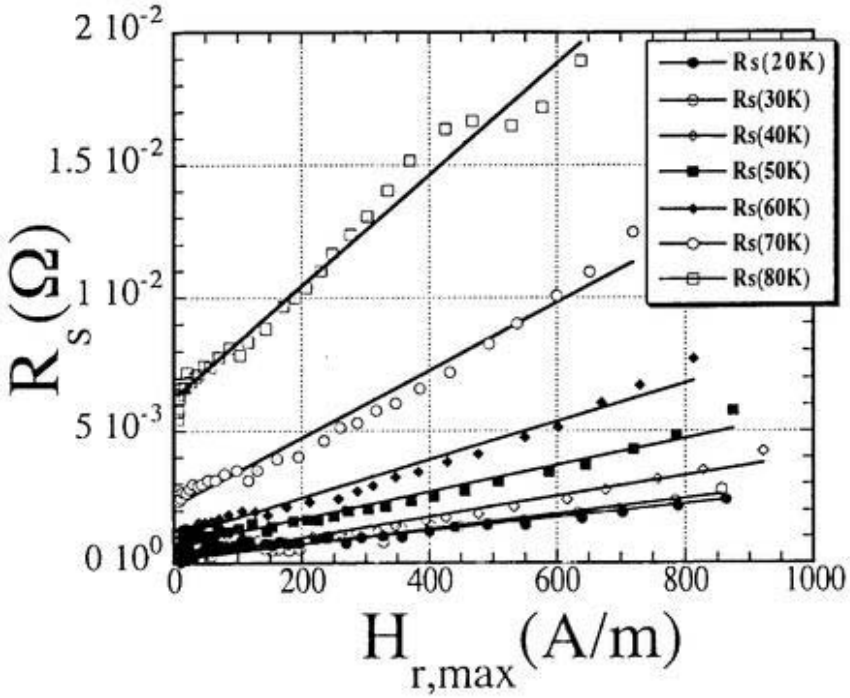

Fig.8.7 (c). The microwave magnetic field dependence of the surface resistance for sample EC425.

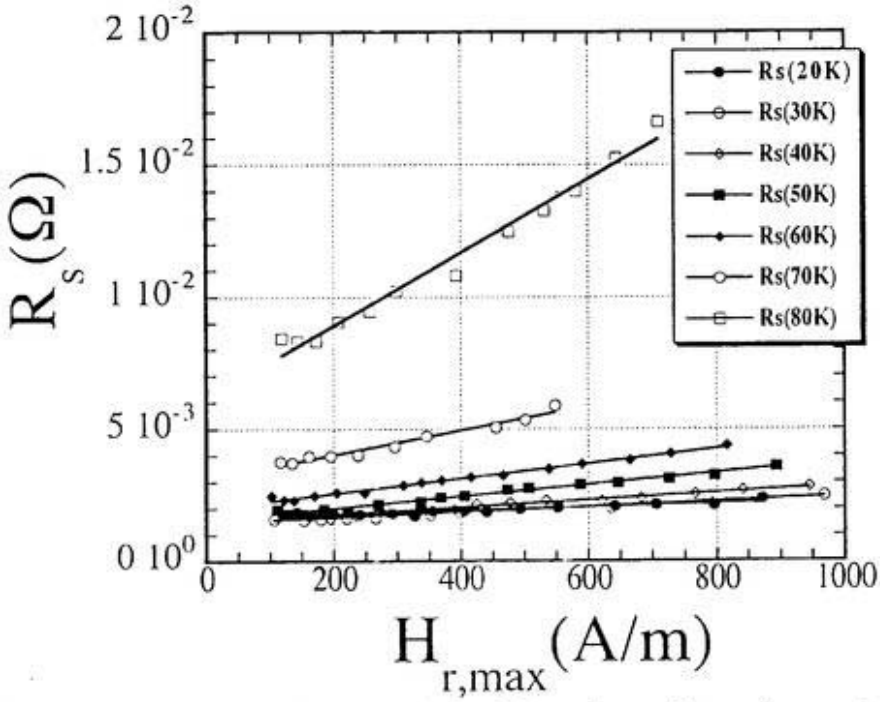

Fig.8.7 (d). The microwave magnetic field dependence of the surface resistance for sample EC403.

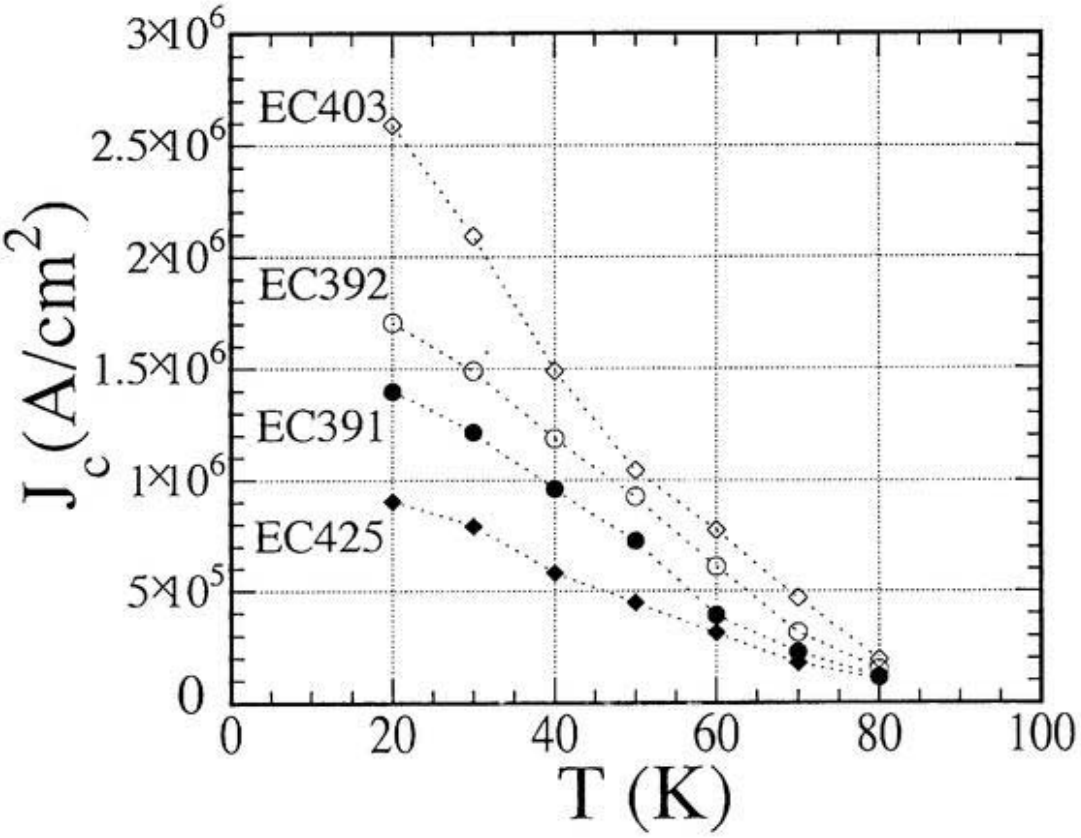

Fig.8.8. The critical current density for samples EC391, EC392, EC425 and EC403.

8.5 Discussion

So far, we obtained the results that the surface resistance R_s for in-plane well-textured films exhibits slightly steeper decrease below T_c and less rf field dependence than R_s for weakly-textured films. These are predicted results and, especially the latter property is very important for cavity application. However, as far as the rf field level is low and the temperature is below 50 K – 70 K, the weakly-textured films have lower R_s than that of well-textured films. At present we do not have any clear explanation for this unpredicted behaviour. Here we present two topics which may be related to this issue; one is an a-b plane anisotropy of conduction (i.e., surface resistance) and the other is the thermal stress remaining in YBCO films.

An anisotropy of surface resistance in a-b plane was reported by Zhang et al. [1] and Bosov et al. [2]. Zhang et, prepared two YBCO crystals (almost 1mm×1mm×0.02mm) and measured the surface resistance by placing the sample at the center of a cylindrical superconducting cavity resonanting at 34.8 GHZ in TE_{011} mode. They showed that R_{sa}, the surface resistance with current running along the a-direction is about 1.7 times as large as R_{sb} at low temperatures. In our case, the cavity is operated in TE_{011} mode and hence the rf current flows along circular paths on the endplate, as illustrated by an arrow in fig. 8.9. The grids in the figure show an array of grains in square shape for a well-textured film. We see from Fig. 8.9 that even if the film is in-plane textured, the rf current circulates experiencing every angle between its flow direction and the a and the b directions. Therefore, it is concluded that the effect of in-plane texturing on R_s can not be clearly evaluated by this measurement. The lower R_s

measured for weakly-textured films would be attributed to some other factors, which are probably related to film making process and conditions.

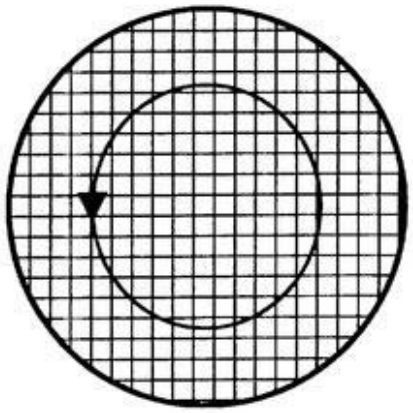

Fig. 8.9. Current path on endplate in TE_{011} mode

Our chief concern at the moment is the stress remaining in YBCO films. The stress could be created by two kinds of parameter-mismatches between film and substrate materials: a mismatch of thermal expansion coefficients and that of lattice parameters between YBCO, YSZ, Cr and Cu. The thermal expansion coefficients (TEC) of YBCO, YSZ, Cr and Cu are given in Table 8.2. The mismatch of TEC between film and substrate

Table 8.2: Thermal Expansion Coefficients (TEC) of YBCO, YSZ, chromium and copper

	Material	ppm/°C
	YBCO	11.6-12.4
	YSZ	10-11
	Chromium (Cr)	~8.4
	Copper (Cu)	~17

materials causes the contraction of the YBCO film. The c-axis of as-grown YSZ buffer layer is elongated in deposition process from that of YSZ powder. Although this strain is somewhat relaxed by heating at 750 C° in YBCO deposition process, it still gives the YBCO film considerable inner stress. It is quite probable that the process for YSZ in-plane texturing gives rise to excess strain in the YSZ layer, and in turn excess stress in the YBCO film.

In summary, for high-field cavity application, it is important for HTS films to be textured in the a-b plane in addition to along the c-axis. Since the rf current path in most of the acceleration cavities is along the cavity axis, *i.e*, the beam direction, it is desirable that the b direction of in-plane textured film is directed to this direction.

References:

1. K. Zhang, D. A. Bonn, S. Kamal, R. Liang, D. J. Baar, W. N. Hardy, D. Basov, and T Timusk, Phys. Rev. Lett. **73**, 2484 (1994).
2. D. N. Basov, R. Liang, D. A. Bonn, W. N. Hardy, B. Dabrowski, M. Quijada, D. B. Tanner, J. P. Rice, D. B. Ginsberg, and T. Timusk, Phys. Rev. Lett. **74**, 598 (1995).

9. Review and Conclusion

The purpose of this work is to study the possibility to apply high-T_c superconductors to future accelerator cavities. YBCO films with the c-axis normal to the film surface were deposited by a laser ablation technique on copper substrates of 36mm in diameter. An YSZ/Cr buffer layer was used for the deposition of YBCO film on copper substrates. The surface resistance and the penetration depth of the YBCO films were measured using a cylindrical host cavity operated at 13.6 GHz in TE_{011} mode.

The deposition on metallic substrates is an important concern from the view point of heat removal in the possible application to accelerator cavities, in which an rf excitation at a high-power level is required. Since the c-axis of the fabricated film is normal to the surface, and, therefore, the surface current flows in the ab-plane of the film, a very low surface resistance was obtained at low temperatures. In order to improve the measurement accuracy at low temperatures, a niobium host-cavity was used to calibrate the data measured by a copper host-cavity. However, since the measurable temperature region in the niobium and copper cavities were restricted and unoverlapped, some fitting procedure were required and will be described in detail. This accuracy improvement by the two-cavity method enabled us to discuss the temperature dependence of the surface resistance more reliably, and, therefore, the excitation mechanism of the normal charge carriers from the superconducting state.

Since some part of the fabricated film could be remain normal even at very low temperature , the two fluid-model was modified to include the residual charge carriers. This modified two-fluid model could well fit the measured surface resistance and penetration depth for a wide temperature range for 4-85K, if the residual charge carriers was assumed to be around 20% of the total charge carriers and the normal charge carries increased in a form $(T/T_c)^2$.

The effect of the film thickness and substrate properties on the measured surface resistance was calculated by the impedance transformation method. The results show that the measured surface resistance R_{eff} is almost equal to the real surface resistance in the temperature range below 70K. However, above 70K, R_{eff} is lowered to some extent depending on the value of penetration depth, and needs some corrections.

The field dependence of the surface resistance was measured for the c-axis textured YBCO films up to the surface magnetic field of 1000 A/m. One of important results was that the surface resistance increases linearly as the field increases, which is explained better by the critical-state model than by the coupled-grain model.

Comparison of the microwave surface resistance between a-b plane well-textured and weakly-textured samples were made. The surface resistance of the weakly-textured samples was lower than that of the well-textured samples for the circular current on the endplate in the TE_{011} excitation mode. However, the increase in the surface resistance with increasing field level was lower for the well-textured samples than for the weakly-textured samples. This suggests the necessity of a-b plane texturing as well as c-axis texturing for superconducting films to be applied to accelerator cavities.

Appendix A

Texture Determination - X-Ray Pole Figures

A pole figure is generally used for determining the texture of polycrystalline material. Recently, the texture of YBCO samples have been determined by the Schulz reflection method. The experimental pole figure setup used included a Diffractometer with Four Circle Sample Holder for raw data collection and a variety of software programs for control of the system and analysis of the data. The x-ray wavelength used usually was $\lambda(CuK\alpha) = 1.54\text{Å}$. The experiment was done by fixing the Bragg condition to a pole of interest (e.g., for the (006) pole, $2\theta = 46.64°$) and scanning ϕ over a the surface of a partial sphere around the sample surface normal. The angles 2θ and ω are the traditional Bragg-Brentano diffraction angles; these are set at specific values for peak (and off-peak, if desired) data collection, the value depending on the pole being measured. The angle χ represents the rotation of the sample holder around an axis in the plane of the sample surface. The angle χ can range from 0° to 80° with reflection methods (transmission methods are required for the final 80° to 90° and can only be done on samples <~20 μm thick). The angle ϕ represents the rotation of the sample holder about the surface normal. This angle is always scanned from 0° to 360°. Coupled with the χ movement, this creates the cone of scanned surface from which the poles of

the bicrystal were detected, and the results are then plotted on a stereographic projection.

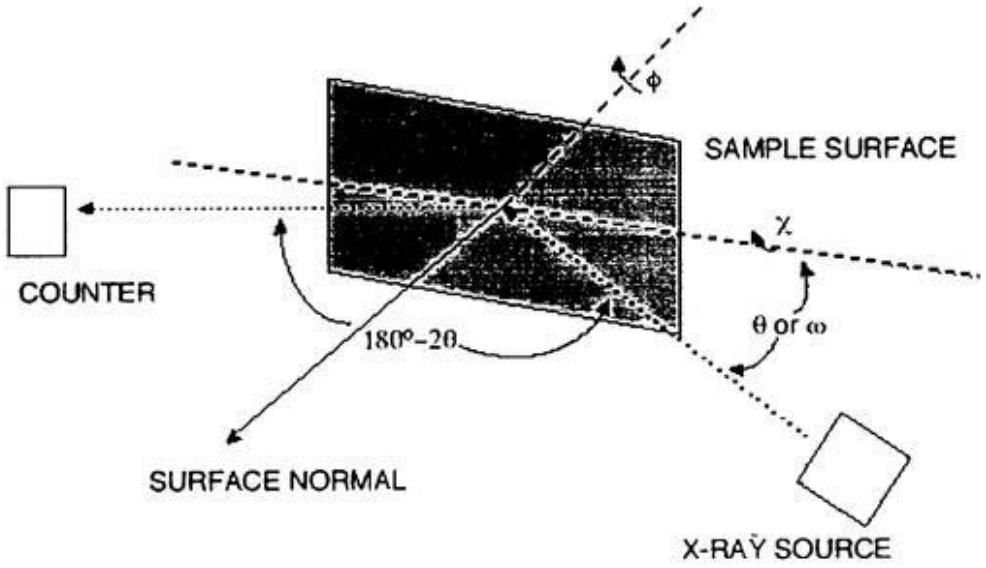

Schematic drawing of the x-ray pole figure apparatus.

Appendix B

Two-fluid model

Two-fluid model[1] is based on the concept that there are two fluids in the superconductors: a superconductive current with a carrier density n_s and a normal current with a carrier density n_n, yielding a total carrier density $n = n_s + n_n$. Free energy expressions were postulated for the superconducting and normal electrons. At temperatures below T_c, the equilibrium fractions of normal and superconducting electrons, n_n/n and n_s/n, vary with absolute temperature, T, as

$$n_n / n = (T / T_c)^4, \tag{1}$$

and

$$n_s / n = 1 - (T / T_c)^4. \tag{2}$$

At $T = 0$, all of the carriers are superconducting, and the fraction of superconducting carriers approaches zero as temperature approaches T_c.

The penetration depth λ_L is also a function of temperature. Substituting the relation n_s/n into the equation $\lambda_L = \sqrt{\Lambda / \mu} = \sqrt{m_s / \mu n_s q_s^2}$ yields

$$\lambda_L(T) = \lambda_L(0)\left[1 - (T / T_c)^4\right]^{-1/2}, \tag{3}$$

where $\lambda_L(0)$, the penetration depth at $T = 0$ K, is defined by

$$\lambda_L(0) = \sqrt{m_s / \mu n q_s^2}\,. \qquad (4)$$

The penetration depth has a minimum value of $\lambda_L(0)$ and diverges as temperature approaches T_c.

References:

1. Z.-Y. Shen, *High-Temperature superconducting microwave circuits*, p.28 (Artech House, Boston, London, 1994).

Appendix C

Surface impedance with two-fluid model

In the microwave regime, the response of a metallic surface to an electromagnetic field can be described by the surface impedance $Z_s = R_s + jX_s$, where the real part R_s (surface resistance) is a measure of microwave power dissipation and the imaginary part X_s (surface reactance) is related to microwave field penetration into the material surface. For low-resistivity normal conductors, such as silver, copper, or gold with a conductivity of σ, the surface impedance can be derived from Maxwell's equations:

$$Z_s = R_s + jX_s = \sqrt{j\mu\omega/\sigma} = (1+j)\sqrt{\mu\omega/2\sigma}\ , \qquad (1)$$

where $\omega - 2\pi f$ is the angular frequency. For normal conductors, σ is a real number, and the surface resistance, R_s, and the surface reactance, X_s, are equal:

$$R_s = X_s = \sqrt{\mu\omega/2\sigma}\ . \qquad (2)$$

Both R_s and X_s are proportional to $f^{1/2}$ for normal metals, and the result has been confirmed experimentally.

In the use of the $Z_s = R_s + jX_s = \sqrt{j\mu\omega/\sigma} = (1+j)\sqrt{\mu\omega/2\sigma}$ for the calculation of the impedance of a superconductor, a natural question arises concerning the value of the conductivity σ. According to the two-fluid model, there are two currents: a superconductive current with volume density J_s and a normal current with volume

density J_n. Correspondingly, the conductivity σ also consists of two components σ_s and σ_n, attributable to the superconducting carriers and normal carriers, respectively, and, $\sigma = \sigma_s + \sigma_n$. We can derive σ_s from the first London equation $\Lambda \frac{dJ_s}{dt} - E = 0$. For a sinusoidal current with angular frequency ω,

$$J_s = \frac{1}{j\omega\Lambda} E = \sigma_s E, \tag{3}$$

and by substituting $\lambda_L = \sqrt{\Lambda / \mu} = \sqrt{m_s / \mu n_s q_s^2}$ for the London constant Λ,

$$\sigma_s = \frac{1}{j\omega\Lambda} = \frac{1}{j\omega\mu\lambda_L^2}. \tag{4}$$

Note that σ_s is pure imaginary, and, does not contribute to the loss.

Analogous to the definition of the superconducting current J_s, the normal current density is defined by

$$J_n = n_n q_n \langle v \rangle, \tag{5}$$

where q_n is the electrical charge for the normal carriers and $\langle v \rangle$ is their average velocity. The normal carriers satisfy the following Newton's law:

$$m_n \left[\frac{d\langle v \rangle}{dt} + \frac{\langle v \rangle}{\tau} \right] = q_n E, \tag{6}$$

where τ is the relaxation time for electron scattering.

Hence,

$$J_n = \frac{n_n q_n^2}{m_n} \frac{\tau}{1 + j\omega\tau} = \sigma_n E, \tag{7}$$

$$\sigma_n = \frac{n_n q_n^2}{m_n} \frac{\tau}{1 + j\omega\tau} = \frac{n_n q_n^2 \tau}{m_n} \frac{1 - j\omega\tau}{1 + (\omega\tau)^2}. \tag{8}$$

The total conductivity for a superconductor is,

$$\begin{aligned}\sigma &= \sigma_n + \sigma_s \\ &= \frac{n_n q_n^2 \tau}{m_n}\frac{1}{1+(\omega\tau)^2} - j\frac{n_n q_n^2 \tau}{m_n}\frac{\omega\tau}{1+(\omega\tau)^2} - j\frac{1}{\omega\mu\lambda_L^2}\end{aligned} \tag{9}$$

At microwave frequency, $\omega\tau << 1$, and it can be simplified to yield,

$$\sigma = \frac{n_n q_n^2 \tau}{m_n} - j\frac{1}{\omega\mu\lambda_L^2}. \tag{10}$$

Substituting it into $Z_s = R_s + jX_s = \sqrt{j\mu\omega/\sigma}$ yields the surface impedance,

$$\begin{aligned}Z_s &= R_s + jX_s \\ &= \sqrt{\frac{j\omega\mu}{\sigma_1 - j\sigma_2}} = j\sqrt{\frac{\omega\mu}{\sigma_2}}(1 + j\frac{\sigma_1}{\sigma_2})^{-1/2}.\end{aligned} \tag{11}$$

Because $\sigma_1 << \sigma_2$, a binomial expansion can be used to simplify the above formula, yielding

$$\begin{aligned}Z_s = R_s + jX_s &= \sqrt{\frac{j\omega\mu}{\sigma_1 - j\sigma_2}} = \sqrt{\frac{\omega\mu}{\sigma_2}}(\frac{\sigma_1}{2\sigma_2} + j) \\ &= \frac{\omega^2\mu^2\lambda_L^3 n_n q_n^2 \tau}{2m_n} + j\omega\mu\lambda_L\end{aligned}, \tag{12}$$

$$R_s = \frac{1}{2}\omega^2\mu^2\lambda_L^3\sigma_N(\frac{n_n}{n}), \tag{13}$$

and,

$$X_s = \omega\mu\lambda_L, \tag{14}$$

where σ_N is the conductivity for the superconductor in its normal state,

$$\sigma_N = \frac{n q_n^2 \tau}{m_n}, \tag{15}$$

$$\sigma_n = \frac{n_n q_n^2 \tau}{m_n} = \sigma_N\frac{n_n}{n} = \sigma_N(\frac{T}{T_c})^4. \tag{16}$$

The two-fluid model leads to the prediction that the surface resistance R_s is proportional to ω^2 for a superconductor. Meanwhile, we should know that the phenomenological theory is valid only when the coherence length $\xi << \lambda_L$, and otherwise, nonlocal theory should be used. For all the known HTS material, $\xi << \lambda_L$ is satisfied, so we limit our discussions to the local limit.

Appendix D

Fields components

With Maxwell's equations and the appropriate boundary conditions, the fields E and H in a circular guide for TE_{mn} mode can be derived as (in the case of TE_{11} mode, m = 1 and n =1):

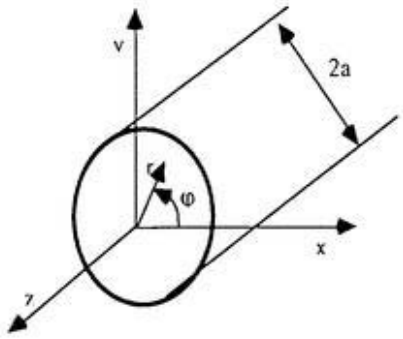

$$E_r = j\omega\mu\left(\frac{a}{q'_{mn}}\right)^2 \frac{m}{r} C J_m\left(\frac{q'_{mn}}{a} r\right) \sin(m\varphi)\left(A\cos(k_z z) + B\sin(k_z z)\right) \quad (1)$$

$$E_\varphi = j\omega\mu\left(\frac{a}{q'_{mn}}\right) C J'_m\left(\frac{q'_{mn}}{a} r\right) \cos(m\varphi)\left(A\cos(k_z z) + B\sin(k_z z)\right) \quad (2)$$

$$E_z = 0 \quad (3)$$

$$H_r = k_z\left(\frac{a}{q'_{mn}}\right) C J'_m\left(\frac{q'_{mn}}{a} r\right) \cos(m\varphi)\left(B\cos(k_z z) - A\sin(k_z z)\right) \quad (4)$$

$$H_\varphi = -k_z\left(\frac{a}{\dot{q}_{mn}}\right)^2 \frac{m}{r} C J_m\left(\frac{\dot{q}_{mn}}{a} r\right) \sin(m\varphi)\left(B\cos(k_z z) - A\sin(k_z z)\right) \tag{5}$$

$$H_z = C J_m\left(\frac{\dot{q}_{mn}}{a} r\right) \cos(m\varphi)\left(A\cos(k_z z) + B\sin(k_z z)\right) \tag{6}$$

where $J_m(x)$, $\dot{J}_m(x)$ are the mth order Bessel function and its first derivative, $\dot{q}_{mn}$ the nth root of $\dot{J}_m(x)= 0$. C, A and B are constants, m and n mode indices in the φ-direction and the r-direction in a cylindrical coordinate (r,φ, z) system, respectively. The field components in TE_{mnp} mode for a cylindrical cavity can be directly derived from TE_{mn} travelling wave fields in a circular guide with the boundary conditions. In order to obtain high Q-values, TE_{01p} mode should be selected. The field components of a cylindrical cavity operated in TE_{01p} mode can be expressed as,

$$\begin{cases} E_\varphi = j\omega_r \mu\left(\dfrac{a}{\dot{q}_{01}}\right) H_0 \dot{J}_0\left(\dfrac{\dot{q}_{01}}{a} r\right) \sin\left(\dfrac{p\pi}{l} z\right) \\ H_r = \dfrac{p\pi}{l}\left(\dfrac{a}{\dot{q}_{01}}\right) H_0 \dot{J}_0\left(\dfrac{\dot{q}_{01}}{a} r\right) \cos\left(\dfrac{p\pi}{l} z\right) \\ H_z = H_0 J_0\left(\dfrac{\dot{q}_{01}}{a} r\right) \sin\left(\dfrac{p\pi}{l} z\right) \\ E_r = E_z = H_\varphi = 0 \end{cases} \tag{7}$$

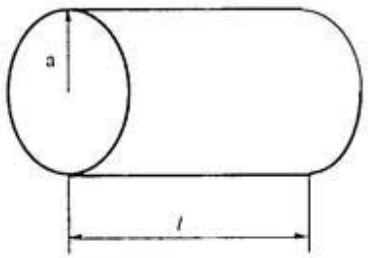

Appendix E

The effective surface impedance of thin film[1]

The response of a metallic surface to an electromagnetic field can be described by the surface impedance

$$Z_s = E_{//} / H_{//} = R_s + iX_s, \tag{1}$$

where $E_{//}$ and $H_{//}$ are the complex amplitudes of the electric and magnetic fields oriented parallel to the surface. Z_s is related to the complex wave number β of the plane wave penetrating into the metal, $\beta = \omega\mu_0 / Z_s$, where ω is the angular frequency of the microwave field and $\mu_0 = 1.256 \times 10^{-6}$ (V s/A m), the permeability in the vacuum. The real part of Z_s, i.e. the surface resistance R_s, determines the power dissipation per unit area:

$$dP / dA = \frac{1}{2} R_s H_{//}^2. \tag{2}$$

The imaginary part of Z_s, i.e. the surface reactance X_s, is related to the magnetic-field penetration depth λ:

$$X_s = \omega\mu_0\lambda, \tag{3}$$

$$\lambda = \mathrm{Re}\left(\int_0^\infty \frac{H_{//}(x)}{H_{//}(0)} dx\right). \tag{4}$$

For a normal conducting metal, Z_s depends on the dc resistivity ρ:

$$Z_s = (\frac{\omega \mu_0 \rho}{2})^{1/2}(1+i). \qquad (5)$$

Equation (5) describes the normal skin effect and holds true if the mean free path of the electrons is small in comparison to the penetration depth and to the ratio of the Fermi velocity and ω. This presumption is fulfilled for high-T_c thin films in the normal conducting state.

The impedance of a dielectric material with relative permittivity ε_r and loss tangent $\tan\delta = 1/\omega\rho\varepsilon$ (where, $\varepsilon = \varepsilon_r\varepsilon_0$) is given by

$$Z = \frac{Z_0}{\varepsilon_r^{1/2}}(1 + \frac{i}{2}\tan\delta), \qquad Z_0 = 377\ \Omega. \qquad (6)$$

In this equation it is presumed that the fields in the substrate are plane waves propagating perpendicular to the surface. This holds true if the wavelength in the substrate is small in comparison to the transverse wavelength in the relevant microwave device. This condition is fulfilled for all air-filled microwave devices like our test cavity, since the permittivity of all relevant substrates for high-T_c films is larger than 10.

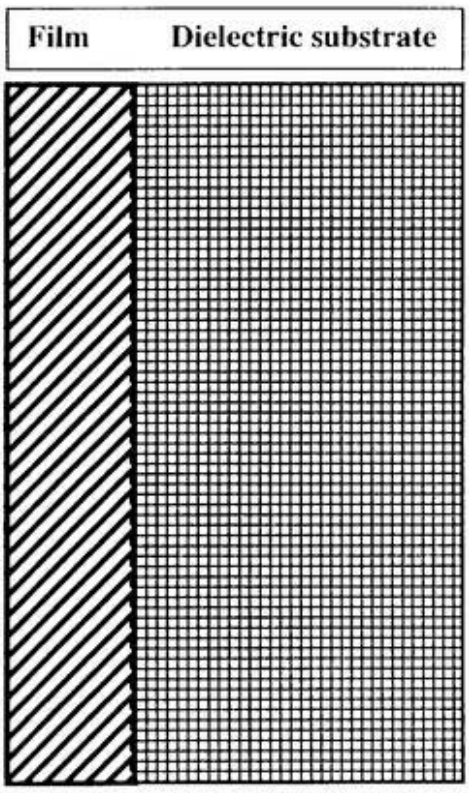

In the case of infinite dielectric substrate, the effective surface impedance, Z_{eff}, of the superconducting thin film with thickness d can be calculated by impedance transformation. The impedance is transferred from the film-substrate interface ($x = 0$) to the film surface ($x = d$) by

$$Z_{\text{eff}} = Z_s \frac{Z / Z_s + i\tan(\beta d)}{1 + i(Z / Z_s)\tan(\beta d)}, \tag{7}$$

where Z_s is the impedance of the film, β the wave number given by $\beta = \omega\mu_0 / Z_s$, and Z the impedance of the dielectric substrate given in Eq. (6). Expanding Eq. (7) in $(R_s/\omega\mu_0\lambda)^n$ and neglecting terms with $n \geq 2$, simple formulas for the real and imaginary parts of Z_{eff} result[1]:

$$R_{\text{eff}} = R_s f(d/\lambda) + R_{\text{trans}}, \tag{8}$$

$$f(d/\lambda) = \coth(d/\lambda) + \frac{d/\lambda}{\sinh^2(d/\lambda)},$$

$$R_{\text{trans}} = \varepsilon_r^{1/2} \frac{(\omega\mu_0\lambda)^2}{Z_0} \frac{1}{\sinh^2(d/\lambda)},$$

$$X_{\text{eff}} = X_s \coth(d/\lambda). \tag{9}$$

References:

1. N. Klein, H. Chaloupka, G. Müller, S. Orbach, H. Piel, B. Roas, L. Schultz, U. Klein and M. Peiniger, J. Appl. Phys. **67**, 6940 (1990).

Appendix F

Calibration of the data obtained by two cavities

By using niobium and copper as the host-cavity material, two data groups were obtained: one below a temperature $T_{Nb,max}$ with the niobium cavity and the other above a temperature $T_{Cu,min}$ with the copper cavity. Taking the measured $R_{s,hTc(Nb)}(T)$ as a reference, we calibrated the systematic error in $R_{s,hTc(Cu)}(T)$ by conforming the measured $Q_{0,Cu+hTc}(T)$. We followed as iteration procedure as follows. In order to avoid complexity, averaging procedures are not described here.

In the firs step,

(i) $R_{s,hTc(Nb)}(T)$ was calculated from the measured $Q_{0,Nb}(T)$ and $Q_{0,Nb+hTc}(T)$.

(ii) $R_{s,hTc(Cu)}(T)$ was calculated from the measured $Q_{0,Cu}(T)$ and $Q_{0,Cu+hTc}(T)$.

Generally the behavior of $R_{s,hTc(Cu)}(T)$ in low temperature region was not smoothly connected to $R_{s,hTc(Nb)}(T)$.

In the second step,

(i) From the condition $R'_{s,hTc(Cu)}(T_{Cu,min}) = R'_{s,hTc(Nb)}(T_{Nb,max})$, $Q'_{0,Cu+hTc}(T_{Cu,min})$ was found through the following equation,

$$\frac{R_{s,hTc}(T)}{R_{s,Cu}(T)} = k\left(\frac{Q_{0,Cu}(T)}{Q_{0,Cu+hTc}(T)} - 1\right) + 1 \qquad (1)$$

(ii) A constant, $c_1 = Q'_{0,Cu+hTc}(T_{Cu,min})/\ Q_{0,Cu+hTc}(T_{Cu,min})$, was multiplied to all $Q_{0,Cu+hTc}(T)$ to obtain $Q'_{0,Cu+hTc}(T)$.

(iii) $R'_{s,hTc(Cu)}(T)$ was calculated from $Q'_{0,Cu+hTc}(T)$ through Eq. (1).

(iv) Both $R_{s,hTc(Nb)}(T)$ and $R'_{s,hTc(Cu)}(T)$ were fit with an equation $R_{fit1}(T)$.

In the third step,

(i) From the condition $R''_{s,hTc(Cu)}(T_{Cu,min}) = R_{fit1}(T_{Cu,min})$, $Q''_{0,Cu+hTc}(T_{Cu,min})$ was found through Eq. (1).

(ii) A constant $c_2 = Q''_{0,Cu+hTc}(T_{Cu,min})/\ Q'_{0,Cu+hTc}(T_{Cu,min})$, was multiplied to all $Q'_{0,Cu+hTc}(T)$ to obtain $Q''_{0,Cu+hTc}(T)$.

(iii) $R''_{s,hTc(Cu)}(T)$ was calculated from $Q''_{0,Cu+hTc}(T)$ through Eq. (1).

(iv) Both $R_{s,hTc(Nb)}(T)$ and $R''_{s,hTc(Cu)}(T)$ were fit with equation $R_{fit2}(T)$.

In principle, the third procedure needs to be repeated until the sequence of the numbers $c_1, c_2, c_3, \ldots$ converges to one.

ACKNOWLEDGMENTS

I would like to thank the many people who have contributed to the work described in this dissertation. I am very grateful to my supervisor, Professor Eizi Ezura, for all of his help, guidance and constant encouragement over the years. It is because of him and the strong supporting group that I will always look back on my time at GUAS with fond memories. Many thanks to Dr. Shigemi Inagaki for teaching me basically everything I know about the experiment setup, measurement techniques, and the theory preparation. The introduction and long discussion on the details of living in Japan for me and my family were invaluable as well. I also need to acknowledge several of the scientists in KEK, including Prof. Shigeru Isagawa, Dr. Hiroshi Nakanishi, and Dr. Kiyomitsu Asano.

I would like to express my thanks to Prof. Hirotaka Sugawara for his support, and to Prof. Yoshitaka Kimura, Prof. Motohiro Kihara, and Prof. Koji Takata for their encouragement and discussion.

My thanks are also extended all the staff of the Accelerator Laboratory, Cryogenic Center of KEK for their help in experiment and their concern for my study.

Outside of KEK, I benefited from collaborations with Prof. Masao Fukutomi and Dr. Kazunori Komori at National Research Institute for Metals, and Dr. Masakazu Saito at Mitsuba electric Mfg. Co., Ltd.

I could perform this study as a scholarship student of the Japanese Government, and like to express my thanks for the financial support.

I wish to express my thanks to Prof. Shouxian Fang, Prof. Shuhong Wang, Prof. Fuquan Zhu, Prof. Mengping Gu, Prof. Dewu Wang, and Prof. Baozhong Dong in IHEP of P. R. China who recommended me to study accelerator science, and introduce KEK to me.

Finally, I thank my parents, my wife and daughter for their patience, sacrifice and love they have given me regardless of my neglecting the duties as a member of a family for my late study.